REDUCING UNCERTAINTIES IN MODEL PREDICTIONS VIA HISTORY MATCHING OF CO_2 MIGRATION AND REACTIVE TRANSPORT MODELING OF CO_2 FATE AT THE SLEIPNER PROJECT

Final Scientific Report

October 1, 2010 – March 31, 2015

Principal Investigator: Professor Chen Zhu
812-856-1884 (phone)
812-856-2223 (fax)
chenzhu@indiana.edu

June 2015

Prepared for:
United States Department of Energy
National Energy Technology Laboratory

DOE Award No.: DE-FE0004381

Federal Project Manager: Dr. Karen Kluger

Karen.Kluger@NETL.DOE.GOV

Submitted by:

Indiana University
P.O. Box 1847
Bloomington, 47402-1847

INDIANA UNIVERSITY
BLOOMINGTON

DISCLAIMER

ABSTRACT

An important question for the Carbon Capture, Storage, and Utility program is "can we adequately predict the CO_2 plume migration?" For tracking CO_2 plume development, the Sleipner project in the Norwegian North Sea provides more time-lapse seismic monitoring data than any other sites, but significant uncertainties still exist for some of the reservoir parameters. In Part I, we assessed model uncertainties by applying two multi-phase compositional simulators to the Sleipner Benchmark model for the uppermost layer (Layer 9) of the Utsira Sand and calibrated our model against the time-lapsed seismic monitoring data for the site from 1999 to 2010. Approximate match with the observed plume was achieved by introducing lateral permeability anisotropy, adding CH_4 into the CO_2 stream, and adjusting the reservoir temperatures. Model-predicted gas saturation, CO_2 accumulation thickness, and CO_2 solubility in brine—none were used as calibration metrics—were all comparable with the interpretations of the seismic data in the literature.

In Part II & III, we evaluated the uncertainties of predicted long-term CO_2 fate up to 10,000 years, due to uncertain reaction kinetics. Under four scenarios of the kinetic rate laws, the temporal and spatial evolution of CO_2 partitioning into the four trapping mechanisms (hydrodynamic/structural, solubility, residual/capillary, and mineral) was simulated with ToughReact, taking into account the CO_2-brine-rock reactions and the multi-phase reactive flow and mass transport. Modeling results show that different rate laws for mineral dissolution and precipitation reactions resulted in different predicted amounts of trapped CO_2 by carbonate minerals, with scenarios of the conventional linear rate law for feldspar dissolution having twice as much mineral trapping (21% of the injected CO_2) as scenarios with a Burch-type or Alekseyev et al.–type rate law for feldspar dissolution (11%). So far, most reactive transport modeling (RTM) studies for CCUS have used the conventional rate law and therefore simulated the upper bound of mineral trapping. However, neglecting the regional flow after injection, as most previous RTM studies have done, artificially limits the extent of geochemical reactions as if it were in a batch system. By replenishing undersaturated groundwater from upstream, the Utsira Sand is reactive over a time scale of 10,000 years.

The results from this project have been communicated via five peer-reviewed journal articles, four conference proceeding papers, and 19 invited and contributed presentations at conferences and seminars.

Table of Contents

EXECUTIVE SUMMARY

Model prediction of CO_2 plume migration and trapping mechanisms (fate) is central to all stages of CO_2 storage operations (site assessment/selection, design, installation, operations and monitoring, and closure/post-closure). Assessing the uncertainties of model predictions represents one of the most daunting challenges for Carbon Capture, Utilization, and Storage (CCUS). However accurate and reasonable estimates of modeling uncertainties are critical for regulatory approval and public acceptance. The Sleipner project in the Norwegian North Sea is the world's first commercial scale geological carbon sequestration project. To date, a total of 15 million metric tons of CO_2 has been injected over a period of 19 years. 4D seismic data have delineated the CO_2 plume migration history in the Utsira sandstone, making Sleipner one of the best places in the world to conduct a multi-phase flow and reactive mass transport modeling of CO_2 migration.

In this project, we first applied two multi-phase compositional simulators (TOUGH2 and GEM®) to the Sleipner Benchmark model for the uppermost layer (Layer 9) of the Utsira Sand and calibrated our model against the time-lapsed seismic monitoring data for the site from 1999 to 2010. An approximate match with the observed plume was achieved by introducing lateral permeability anisotropy, adding CH_4 into the CO_2 stream, and adjusting the reservoir temperatures. Model-predicted gas saturation, CO_2 accumulation thickness, and CO_2 solubility in brine—none were used as calibration metrics—were all comparable with the interpretations of the seismic data in the literature.

Second, to evaluate the uncertainties in predicted long-term fate of CO_2, we used various kinetic rate laws for mineral dissolution and precipitation in Reactive Transport Models (RTM) using the software package ToughReact. The temporal and spatial evolution of the partitioning among the four trapping mechanisms (hydrodynamic/structural, solubility, carbonate minerals, residual/capillary) was simulated up to 10,000 years. The results show that over a long period of time, the Utsira Sand is reactive and the ad hoc use of the linear rate law in the literature represent the upper bound of the predicted mineral trapping.

This project was productive. The following publications and presentations acknowledged the funding from this grant:

PEER-REFERRED PUBLICATIONS ACKNOWLDGING DOE SUPPORT (‡student authors)

1. **Zhu** C, ‡Zhang GR, ‡Lu P, ‡Meng LF, Ji X (2014) Benchmark modeling of the Sleipner CO_2 plume: Calibration to seismic data for the uppermost layer and model sensitivity analysis. ***The International Journal of Greenhouse Gas Control.*** doi10.1016/j.ijggc.2014.12.016.
2. ‡Zhang GR, ‡Peng L, ‡Zhang YL, Wei XM, †Zhu C (accepted for publication) Effects of rate law formulation on predicting CO2 sequestration in sandstone formations. ***International Journal of Energy Research***.
3. ‡Zhang GR, Lu P, **Zhu** C (2014) Model predictions via history matching of CO_2 plume migration at the Sleipner Project, Norwegian North Sea, ***Energy Procedia***, 63: 3000-3011, DOI information: 10.1016/j.egypro.2014.11.323
4. Ji X and **Zhu** C (2013) A SAFT Equation of State for the H_2S-CO_2-H_2O-NaCl system and applications for CO_2 - H_2S transportation and geological storage. ***Energy Procedia*** 37: 3780-3791. doi: 10.1016/j.egypro.2013.06.274.
5. Ji X and Zhu C (2013) Predicting possible effects of H_2S impurity on CO_2 transportation and geological storage. ***Environmental Science & Technology***. 47, 55-62, dx.doi.org/10.1021/es301292n.
6. Ji X and Zhu C (2013) A SAFT Equation of State for the Quaternary H_2S-CO_2-H_2O-NaCl system. ***Geochimica et Cosmochimica Acta*** 91, 40–59, http://dx.doi.org/10.1016/j.gca.2012.05.023.

7. **Zhu** C, Lu P (2013) Coupling of dissolution and precipitation reactions as the main contributor to the apparent discrepancy between lab and field reaction rates. ***Procedia of Earth and Planetary Sciences***. International Symposium on Water-Rock Interaction WRI-14, (7)948-952, 4 pages. DOI 10.1016/j.proeps.2013.03.051. PROEPS317
8. ‡Lu P, Fu Q, Seyfried Jr., WE, Jones K., and †**Zhu** C (2013) Coupled alkali feldspar dissolution and secondary mineral precipitation in batch systems: 2. Effects of CO_2 and implications for carbon sequestration. ***Applied Geochemistry*** 30, pp. 75-90 , Doi 10.1016/j.apgeochem.2012.04.005
9. ‡Liu Y, ‡Lu P, Griffith C, Soong Y, Hedges SW, H Hellevang H, **Zhu C** (2012), CO_2-caprock-brine interaction: Reactivity experiments on Eau Claire Shale and a review of literature. ***The International Journal of Greenhouse Gas Control*** 7, 153–167, doi.org/10.1016/j.ijggc.2012.01.012.

BOOK CHAPTER ACKNOWLDGING DOE SUPPORT

Ji X and Zhu C (accepted) “CO_2 storage in deep saline aquifers” A chapter in *Novel Materials for Carbon Dioxide Mitigation Technolo*gy to be published by Elsevier.

INVITED TALKS AND COLLOQUIUM ACKNOWLDGING DOE SUPPORT

1. University of New Hampshire, Durham, NH, October 16, 2014
2. Forum on geofluids, Jinlin University, Changchun, China, September 13, 2014
3. Invited speaker, “CO_2-Water-Rock Interactions during Geological CO_2 Storage”, First Joint Scientific Meeting of Geological Society of China and Geological Society of America, Chengdu, China, June 17-19, 2013.
4. University of Oslo, Department of Geosciences, Norway, May 3, 2012.
5. Woods Hole Oceanographic Institution, October 18, 2011.
6. University of Illinois at Chicago, Department of Earth and Environmental Sciences, April 14, 2011.
7. Ben-Gurion University of the Negev, Israel, March 16, 2011.
8. “Geochemical Modeling” short course, Israel, March 11-15, 2011.
9. Third U.S.-China CO_2 Emissions Control Science & Technology Symposium, Hangzhou, China, December 10-12, 2010.
10. National Energy Technology Laboratory, Earth Science Seminar Series, Pittsburgh, PA, November 19, 2010.
11. “Kinetics of water-rock interactions in geological carbon sequestration”, Washington University - St. Louis, weekly departmental colloquium, Department of Energy, Environmental and Chemical Engineering, November 5, 2010.

CONTRIBUTED TALKS ACKNOWLDGING DOE SUPPORT

1. Zhang G, Lu P, Zhu* C (2013) Model Predictions via History Matching of CO_2 Plume Migration at the Sleipner Project, Norwegian North Sea. American Geophysical Union Annual meeting, San Francisco, December 9 -15, 2013.
2. Zhang Z, Agarwal R, Zhu* C (2013) Optimization of CO_2 Storage in Saline Aquifers Using Water-Alternating Gas (WAG) Scheme – Case Study for Utsira Formation. American Geophysical Union Annual meeting, San Francisco, December 9 -15, 2013.
3. Lu, P., Zhu, C., and Aaggard, P. (2012) Reducing Uncertainties in Model Predictions via History Matching of CO2 Plume Migration at the Sleipner Project, Norwegian North Sea, American Institute of Chemical Engineers (AiChe) 2012 Annual Meeting, Pittsburgh, October, 2012.
4. Ji, X. and Zhu C. (2012) Thermodynamic study for CO_2 storage in deep saline aquifers. 11th International Greenhouse Gas Control Technology meeting (GHGT-11), November 18-22, 2012, Kyoto, Japan.
5. Ji X. and Zhu C. (2011) A SAFT Equation of State for the Quaternary H_2S-CO2-H2O-NaCl System. American Geophysical Union Annual meeting, San Francisco, December 5 -10, 2011.
6. Zhu C, Project review meeting, Pittsburgh, August, 2012
7. Zhu C, Project review meeting, Pittsburgh, August, 2013
8. Zhu C, Project review meeting, Pittsburgh, August, 2014

Part I. History Matching of CO_2 Plume Migration with a Reservoir Model

INTRODUCTION

The predictive modeling of CO_2 plume is indispensable for Carbon Capture, Utility, and Storage (CCUS) projects. Numerical models are used by applicants and regulators to make decisions at all phases of a project ranging from site selection, characterization, and injection to post-injection monitoring. A mathematical model is also a management tool; models are updated and refined as data from characterization, injection, and monitoring become available. However, the accuracy of modeling results and information concerning the uncertainties of a model must be taken into account. The complexity of multiphase flow and the complexity of geological systems both pose challenges to modeling adequately and predicting CO_2 plumes. The Sleipner project provides an opportunity to explore some of these issues addressed above.

The Sleipner project, situated in the Norwegian North Sea, is the world's first industrial-scale geological carbon storage project. Beginning in 1996, CO_2 separated from natural gas has been injected into the Utsira Sand at the rate of approximately one million metric tons of CO_2 per year (NRC, 2013). By the middle of 2012, a total of ~13.5 Mt of CO_2 had been injected (NRC, 2013). Seismic surveys of the site were conducted prior to injection in 1994, and then repeated in 1999, 2001, 2002, 2004, 2006, 2008, and 2010 (Chadwick et al., 2009; Chadwick et al., 2010; Boait et al., 2012; Hagen, 2012). These surveys have produced 4D seismic data that have delineated a CO_2 plume migration along a north-south trending topographic ridge in the Utsira Sand. The Utsira Sand has a storage potential of 2-15.7 billion tons of CO_2, and could become a major reservoir for neighboring countries for years to come (NRC, 2013).

Because of these circumstances, the Sleipner project provides an opportunity to answer several important questions: (1) Can we adequately predict CO_2 plume sizes and flow directions?

(2) What does it take to match observed CO_2 plume migration data? (3) Are widely available reservoir simulation tools adequate to simulate multiphase flow?

CO_2 migration in the subsurface is a complex process, and numerous "conceptual models" have been developed and published (Doughty and Pruess, 2004; Johnson et al., 2004; Kumar et al., 2004; Audigane et al., 2007; Xu et al., 2007; Cameron and Durlofsky, 2012; Cheng et al., 2012; Court et al., 2012; Nilsen et al., 2012; Zhang and Sahinidis, 2013). In these models, idealized geometry, homogeneous and isotropic permeability, and isothermal aquifers are typically assumed. While these models have helped to elucidate the many processes and the complex interplay between processes that ultimately determine CO_2 migration, these models do not provide an insight into how CO_2 migrates in real geological systems. Applying mathematical models to real geological systems helps to illustrate the complexity of the geological systems, such as reservoir geometry, spatial heterogeneities, and uncertain boundary conditions. Therefore, although various models in the literature, which explored different aspects of the complex processes, have served to identify the critical processes and parameters that determine CO_2 migration and fate, these models must be tested in geological systems with calibration data.

In this study, we first applied two advanced compositional simulators, GEM® and TOUGH2, to the Sleipner Benchmark model released by Statoil, and calibrated the model to match approximately with CO_2-brine contact development (1999-2008) by introducing permeability anisotropy and a combination of reservoir temperature and CH_4 composition adjustments. Secondly, we conducted sensitivity analysis for CO_2 plume migration and fate at Sleipner Project in order to identify the critical factors controlling CO_2 sequestration. Finally, based on the analysis results, we discussed model uncertainties in order to guide future data collection and observation.

2. GEOLOGICAL SETTINGS AND FIELD DATA

Starting in 1996, CO_2 separated from the natural gas at Sleipner Field has been injected into the Utsira Sand. The Utsira Sand extends along the Viking Graben near the UK/Norwegian median line for more than 450 km south-north between 58 ^{o}N and 61^{o}40N, and 75~130 km east-west between 1^{o}E and 3^{o}50E (**Fig 1**). The Utsira Sand has an average porosity of 36% and a permeability range from 1 to 5 Darcy. Its thickness ranges between 200 and 300 m with the top of the formation at about 800-1000 m below sea level at the injection point (Baklid et al., 1996; Zweigel et al., 2004; Singh et al., 2010). The injection point is located 1012 m below the mean sea level (Chadwick et al., 2005).

Baseline time-lapse 3D seismic data were acquired in 1994, prior to the injection. Repeat surveys were conducted from 1999 to 2010, the latter two augmented by a high resolution 2D seismic and seabed imaging survey (Chadwick et al., 2009). Nine CO_2 accumulation layers have been identified through seismic data (**Fig 2**). The topography (lateral extent, continuity, etc.) of each layer is markedly different. However, only the uppermost CO_2 plume in the “Sand Wedge” unit (Layer 9), which is separated by a 5 m shale unit as its lower boundary, is clearly resolved based on the shallowest bright reflection in the seismic data. CO_2 accumulation through time has also been quantified in this layer (Chadwick and Noy, 2010; Boait et al., 2012). On the other hand, the interpretation of lower CO_2 plume layers is affected by the overlying bright seismic reflections (Lumley, 2009). Therefore, this study focuses on only the uppermost CO_2 storage in the Layer 9 where topography is well defined. Layer 9 is in immediate contact with the overlying sealing caprock. Therefore, CO_2 behavior and fate in this layer is determinative to the long-term effectiveness and security of the containment.

Although the availability of time-lapsed seismic data makes Sleipner an ideal site for comparing simulated and observed CO_2 plume, the lack of well data near the injection site has resulted in uncertainties of reservoir temperature and pressure as well as in brine chemistry (Singh et al., 2010). Therefore, sensitivity analysis to evaluate the effects of uncertainties of these parameters on CO_2 plume migration is valuable for assessing model uncertainties.

3. MODEL CONSTRUCTION AND CALIBRATION

History-matching the development of CO_2 plume is essentially an inverse problem. Considerable progress has been made with respect to solutions to inverse problems in geophysics and hydrogeology during the last two decades (Box et al., 1994; Parker, 1994; Law and Kelton, 2000; Aster et al., 2005; Hill and Tiedeman, 2007). These procedures, nevertheless, are difficult to apply to the Sleipner field-scale reservoir model. Therefore, we relied on the conditional trial-and-error method.

Based on the principles of inverse problem solving theories, a workflow was developed (**Fig 3**). First, we translated the Sleipner Benchmark model into GEM® and TOUGH2. The Sleipner Benchmark is a modeling benchmark, released by Statoil and managed by the IEAGHG R&D program. The model comprises a numerical mesh with a cell resolution of 50×50 m^2 and related data package that is designed for comparative high resolution simulations (Singh et al., 2010). Second, we calibrated the model against the boundaries of the imaged CO_2 plume as the only history match metrics. The horizontal permeability anisotropy, reservoir temperature, and CH_4 % in CO_2 streams were adjusted as model input until reasonable matches were obtained. Third, a range of parameters, such as temperature, pressure, relative permeability curves, number and locations of feeders, and CH_4 content, still remain uncertain (Singh et al., 2010). The potential impacts from the uncertainties of these parameters were evaluated and the model uncertainty is discussed in detail below.

3.1. Model Parameterization

The grid mesh from the Benchmark model was translated into GEM® and TOUGH2. GEM® is an adaptive-implicit multiphase multi-component flow simulator with phase equilibrium and mineral dissolution/precipitation that uses the fully-coupled approach (Nghiem et al., 2004; CMG, 2009). The modeled area is approximately 3 × 6 km. The grid dimensions are x = 65, y = 119, z = 43 with a total of 332,605 blocks. Modeling parameters are shown in **Table 1.** GEM® uses a Peng-Robinson equation of state (Harvey, 1996) for calculating CO_2 density and solubility. CO_2 viscosity was calculated based on the HZYT method (Herning and Zipperer, 1936; Jossi et al., 1962; Yoon and Thodos, 1970). The viscosity of brine was calculated using the equation from Whitson and Michael (2000) and data from Kestin et al. (1981).

TOUGH2 is developed by the Lawrence Berkeley National Laboratory and is a simulator for modeling non-isothermal multiphase flow in the system H_2O-NaCl-CO_2 (Pruess, 2005). In TOUGH2, density and viscosity of CO_2-rich phase, approximated as pure CO_2, are obtained from correlation developed by Altunin (1975). Brine density for binary system water-salt is calculated first from the correlations of Haas (1976) and Andersen et al. (1992). The density of aqueous phase with dissolved CO_2 is calculated assuming additivity of the volumes of brine and dissolved CO_2 (Pruess, 2005). Brine viscosity is obtained from the correlation presented by Phillips (1981), but no allowance is made for dependence of brine viscosity on the concentration of dissolved CO_2. In this study, Cartesian grid is employed in TOUGH2 model for spatial discretization.

The reservoir was initially saturated with water (S_w = 0.9999). The method of gravity initialization for a reservoir was used in GEM. When this initialization is performed, a table is constructed, which give water pressure and several other properties as functions of depth. This table is constructed by Runge-Kutta integration of the differential equation determining the hydrostatic pressure. The initial pressure of each cell is then assigned based on the values in the table.

The boundary condition applied to our simulations for solving the mass transport equations was a Dirichlet condition boundary. This Dirichlet boundary was implemented by assigning a large (infinite) volume to the boundary grid block (Pruess et al., 2012). Consequently, any influence from the influx became negligible compared to the large volume of the formation brine. The aqueous chemical composition of the boundary element, as well as its thermodynamic conditions, such as temperature and pressure, was therefore kept essentially unchanged from the original formation brine (Pruess et al., 2012). In this study, background Darcy velocity of groundwater was considered to be zero.

In many cases, we used both GEM® and TOUGH2 for inter-simulator comparison. For simplicity, all discussions below use the results from GEM® unless otherwise indicated.

3.2 Model Calibration

The starting point of our calibration was permeability values and distribution in the original Benchmark model: *k* value near 2 Darcy, no horizontal permeability anisotropy, and vertical permeability of ~ 1/10 of the horizontal permeability. However, geological studies of the Utsira Sand at Sleipner have suggested that the system has deep channel/canyon-like feature at the northeast margin of the Utsira Sand (Gregersen, 1998; Eidvin and Rundberg, 2001). Similar incised channel-like features have also been identified at the western or eastern base of the formation that are suspected to be entry for some of the sand transport into the basin (Gregersen, 1998). The channel features suggested that the system was formed with a north-south trend, indicating preferential north-south permeability anisotropy (Gregersen, 1998; Gregersen and Johannessen, 2007). This is also consistent with the observation from the seismic data that revealed an elongated north-trending CO_2 plume after the injection.

We adopted k = 2 Darcy east-west and 10 Darcy north-south and compared with the scenario of k = 2 Darcy isotropic in all horizontal directions (**Fig 4a**). The results were comparable with the TOUGH2 simulations from Chadwick and Noy (2010). We reached similar conclusions as Chadwick and Noy (2010) that anisotropic permeability improved the match somewhat, but it is not possible to match the observed spreading of the topmost layer by adjusting permeability alone.

Next, we calibrated our model against the CWC development by adjusting temperature and CH_4 and found plume migration is highly sensitive to both parameters. However, adjusting T or CH_4 alone would not result in a match with the observed plumes unless the T or CH_4 was outside of realistic ranges. Nevertheless, a combination of temperature and CH_4 values that are within the ranges of reported values in the literature could generate approximate matches. We settled on a combination of 33.5 ^oC and 2.4% CH_4. Detailed discussion of the literature temperature and CH_4 values will be presented below.

The simulated CWC matched approximately with the observed areal extent of the CO_2 plume in 1999, 2001, 2002, 2004, 2006, and 2008 and showed improvements over previous models (**Fig 5**), in replicating the elongated, northward extension of the observed plume. In order to compare different model runs, we used image analysis software to calculate the percentages of areas within the CO_2 plume outline that the models failed to fill with CO_2 (gap areas) (**Fig 6**). It should be noted, however, that the image analysis was two-dimensional while CO_2 distribution was three-dimensional, and hence the comparison does not always paint a whole picture.

3.3 The Calibrated Model

For our calibrated model, the only calibration targets were the CO_2-water contacts (CWC) because the lateral spread of the CO_2 plume can be tracked in detail by seismic data (Chadwick and Noy, 2010). The only adjusted parameters were permeability anisotropy, reservoir temperature, and CH_4 in CO_2 streams. Other physical attributes of the model discussed below are forward predictions or inferences. These predictions are compared to the interpretations of seismic data below. We need to emphasize here that the interpretations are not observations but estimates with widely ranging uncertainties (Chadwick and Noy, 2010).

In our model, Layer 9 was divided into 34 vertical sub-layers (~ 0.35 m per sub-layer). The sizes and saturation of CO_2 distribution in each sub-layer decreased significantly from top to bottom. The area of CO_2 distribution in the topmost sub-layer delineated the maximum extent of the CO_2 plume migration.

The distribution of gas saturation simulated by our calibrated model is comparable to gas saturation maps from Chadwick and Noy (2010). As mentioned earlier, the gas saturation maps from seismic data interpretations are less accurate than the CO_2 plume outlines, and our simulated gas saturation distributions were results of "forward modeling." This means that the seismic data-based gas saturation maps were not used as calibration targets. Seismic data alone do not quantify the maximum CO_2 saturation (S_{CO2}) in the field, and the relative permeability curve that we used in our model limited S_{CO2} to 0.8. The average gas saturation maps from

Chadwick and Noy (2010) were constructed from the relationship between gas saturation and capillary pressure, which was determined by centrifuging experiments on cores from the Utsira Sand (Singh et al., 2010). Although the high gas saturation areas from the multiphase flow simulations and seismic interpretations are similar, the simulation results show that much more dispersive gas saturation along the plume fringes, particularly in the west.

The thicknesses of the CO_2 plume inferred from the model are also comparable to the estimates reported in Chadwick and Noy (2010). For 2001, the thickness is 3.0 m for the thickest area and 0.3 m for the thinnest area; for 2004, 4.5 m for the thickest area and 0.3 m for the thinnest area; and for 2006, 6 m for the thickest area and 0.35 m for the thinnest area. These values compared well with CO_2 plume thickness reported in the literature. Note that Chadwick et al. (2005) obtained the CO_2 layer thickness both from reflection amplitudes and structural analysis.

Our model calculated a CO_2 gas solubility of ~ 1.134 mol/kgw, which is similar to the CO_2 solubility calculated following Duan et al. (2006) (1.135 mol/kg at 33 ^oC, 83 bars, and 0.57 m NaCl). Considering the relatively short time (several years) after the initial injection, the injected CO_2 is mainly in a supercritical state as expected. Dissolved CO_2 is the dominant phase in the first several days as CO_2 encounters fresh brine that was undersaturated with respect to CO_2, but free phase supercritical CO_2 took over after several days because the solubility limit of CO_2 was reached and supercritical CO_2 displaced CO_2 saturated brine afterwards. With time, the fraction of dissolved CO_2 approaches 7%. The previous estimates of dissolved CO_2 based on seismic data are in the range of 5-10% total CO_2 injected (Chadwick and Noy, 2010).

4. SENSITIVITY ANALYSIS

The primary model output considered in the sensitivity analysis for this paper was the CWC in Layer 9. The justification for choosing CWC was that other plume attributes reported in the literature, such as the distribution of CO_2 saturation within the plume, plume thickness, and the amount of CO_2 trapped, are more subject to interpretations and are generally of lower accuracy (Chadwick and Noy, 2010). In addition, CWC is often related to the area of review (AoR) in regulatory decisions.

For Sleipner, Chadwick and Noy (2010) investigated the effects of temperature and topography gradient error on the CWC development. The effects of different simulators (such as black-oil simulator, invasion percolation simulator, and compositional simulator) on CO_2 sequestration modeling were investigated by Singh et al. (2010) and Cavanagh (2011). Cavanagh (2013) has employed a black-oil simulator with power-law and straight line respectively for relative permeability curves, and found that the general trend of CWC for these two scenarios is similar. However, the effect of impurities in the injected CO_2 stream on CO_2 plume, and the combined effects of temperature, pressure, and CH_4 have never been investigated. As shown below, it turned out that these combinations are important to generate an approximate match with the observations. Here, we focus on the factors of temperature, pressure, CO_2 spill rate, and impurities in injected CO_2 stream. We also found that relative permeability curves had small effects and the details are omitted from further discussion here. The issues of local topography error and geochemical process will be analyzed in our discussion on model uncertainty.

4.1 Reservoir Temperature

No direct measurement of reservoir temperature in Layer 9 is available. Chadwick and Noy (2010) used a temperature of 31.5 ^{o}C in their base case for a pure CO_2 stream, which is equivalent to density of a CO_2-methane (2% CH_4) mixture at 29 ^oC. They also tested a case with a temperature of 36 ^oC for sensitivity analysis. Bickle et al. (2007) calculated the temperature at Layer 9 to be 35 ^oC based on the following factors: the temperature of 41 ^oC at the injection depth 1012 m, the temperature of 7 ^oC at the depth 80 m, and the variable thermal conductivity that accompanies depth. We calculated the temperature at Layer 9 based on the temperature being 41 ^oC at the injection depth and a geothermal gradient of 35.6 degree/km in Sleipner Benchmark. A temperature of 33.2 ^oC was thereby calculated and used as a basis for sensitivity analysis.

In order to evaluate the effect of reservoir temperature on migration and fate of the injected CO_2, we used a range of temperatures in our model (29-37 ^oC). **Figure 7a** presents a case with an extreme value of 37 ^oC and the results are compared with that in the Base Case. Simulated CWC do not show much change in south, east, or west, but CWC extend further north with increased reservoir temperature. Supercritical CO_2 under Sleipner *P*, *T* conditions has gas-like properties, and CO_2 density and viscosity decrease drastically with temperature (**Fig 8**). Lower CO_2 density and viscosity helped CO_2 to spread along the topographic ridge from south to north (**Fig 7a**), and also helped increase the spreading speed of CO_2 (**Fig 9**). Therefore, the simulated CWC is quite sensitive to the reservoir temperature at Sleipner.

4.2. Reservoir Pressure

There are no direct measurements of reservoir pressure for Layer 9. In previous studies, the pressures in Layer 9 were calculated based on the hydrostatic gradient, assuming that pressures are hydrostatic (Bickle et al., 2007). The pressure calculated by Cavanagh based on the hydrostatic gradient (personal communication) is 8.0 MPa at the reservoir top and 8.6 MPa at the reservoir bottom. We adopted the value of 8.3 MPa at 820 m as a reference for our Base Case. To analyze the effects of pressure on the simulation results, we used a range of pressures in our model (8.0-8.6 Mpa, **Table 2**). **Fig 7b** compared the Base Case and the Test Case-Pressure by using a pressure of 8.0 MPa at 820 m.

The results show that the simulated CWC do not change much in the west, east, or south (**Fig 7b**). Within the range of pressures reported in the literature (e.g., the box in **Fig 8b**), small changes of pressure can drastically alter the density of CO_2, again, because CO_2 at the P-T condition of Sleipner has gas like properties. This is further complicated with CH_4 contents (**Fig 8b**). Combinations of P-T-CH_4, all within reported ranges, can have much lower density and CO_2 migrates further north. From that point of view, plume migration is also very sensitive to pressure although its effect is much smaller than that of temperature (within the reported range) when considered independently.

4.3. CO_2 Spill Rate and Total Mass into Layer 9

Our Base Case used the volume and rate of CO_2 spill into Layer 9 that were provided by Statoil. For sensitivity analysis, we increased the CO_2 spill rate 20% from that in the Base Case to evaluate its effect on CO_2 migration and fate. While simulation results show slightly increased areal expansion of the plume (**Fig 7c**), the plume thickness increased by 15%. Therefore the simulated plume thickness is more sensitive to a CO_2 spill rate than CWC and verifying the model only through comparing CWC on the plane view could result in large estimation errors for CO_2 accumulation at Sleipner.

4.4. Composition of Injected CO_2 Stream

The CO_2 at Sleipner contains about 1.5-2.5% methane and also unspecified amounts of butanes, toluenes, and xylenes (BTX) (Zweigel and Heill, 2003; Zweigel et al., 2004; Arts et al., 2008; Chadwick and Noy, 2010). In order to evaluate the effects of the composition of injected CO_2 on the simulation results, we used a range of CH_4 (0-4%) in our model and evaluated the modeling results. GEM® uses the Peng-Robinson equation for describing the mixing properties of CO_2 and CH_4. Significant different density values could be predicted using different models. **Figure 8b** shows predicted densities of CO_2-CH_4 mixture calculated using the SAFT2 approach.

Figure 7d,e,f show the simulation results using CH_4 of 1.8%, 2.7%, and 4% in the CO_2 stream in our model. **Figure 5b** shows the case of 2.4% CH_4. These CH_4 values are paired with respective temperatures, and with the exception of the 4% CH_4 case, the CH_4-T pairs produced similar matches with observed plumes. For the extreme case of 4% CH_4, the difference in densities between brine and gas phase increased from 384 kg/m^3 for the Base Case to 619 kg/m^3, and the viscosity of the gas phase decreased from ~5×10^{-2} to 3×10^{-2} cp (**Fig 8**). The velocity of the CO_2 flow is much higher than that in the Base Case (**Fig 9**). As a result, the test case simulated a plume that migrated beyond the north narrow ridge in all years (**Fig 7d**). The plume, however, spreads over to both the west and east flank of the main plume body. The addition of CH_4 also produced a thicker CO_2 plume on the vertical profiles (not shown). Therefore, the simulated plume is quite sensitive to the CO_2 stream compositions at Sleipner.

4.5. Sensitivity for CO_2 fate

The fate of CO_2 can be expressed as trapping mechanisms: structural (hydrodynamic), solubility, residual (capillary), and mineral trapping (IPCC, 2005). **Figure 10** shows the maximum ranges of hydrodynamic and solubility trapping in terms of total injected CO_2 when a range of modeling parameters was used. Here, we only analyzed the effects on structural trapping and solubility trapping. Residual trapping is small at Sleipner because it is still in the injection phase. Residual trapping will become more important when CO_2 injection stops and formation water flows back into the reservoir again (Liu et al., 2011). Mineral trapping is a slow process (IEA, 2008) and here at Sleipner it is negligible (see below).

Figure 10 shows that the largest uncertainties in simulated trapping mechanisms are from the CH_4 content and temperature. Adding CH_4 content to 4% can increase CO_2 solubility trapping by ~1.8%, while, with the temperature increased to 37 ^{o}C, CO_2 solubility trapping can be raised by ~1.4%.

In Test Case-CH_4 with 4% CH_4, CO_2 plume volume increased due to both increased areal extent and thickness of the CO_2 plume compared with Base Case. Water saturation did not change and CO_2 solubility was reduced slightly to 1.09 Molal from 1.13 Molal in Base Case. The cumulative effects are that solubility trapping increased ~1.8% as shown in **Fig 10**. Therefore, solubility trapping is much sensitive to CH_4 content due to the increased CO_2 plume volume.

In Test Case-Temperature with 37 ^{o}C, CO_2 plume had behavior similar to that in Test Case-CH_4. CO_2 plume volume increased due to both increased areal extent and thickness of the CO_2 plume when compared with Base Case. Water saturation changed little and CO_2 solubility was reduced slightly to 1.08 Molal. As a result, solubility trapping increased ~1.4% (**Fig 10**). Thus, temperature has an effect on solubility trapping due to the increased CO_2 plume volume, which is caused by lower CO_2 density because of higher temperature.

In summary, even with a wide range of parameter uncertainties (even with extreme values outside of known ranges), the resultant simulated trapping mechanisms only differ by

±2%. However, the above analysis can be undermined by the mass balance error in numerical models. We computed mass errors and the CO_2 mass balance accounting error is ~-0.13% for the Base Case and they vary slightly in different test cases. Therefore, the major part of the uncertainties is not related to software artifacts.

5. DISCUSSION ON MODEL UNCERTAINTY ISSUES

5.1. Number of Feeders

Most of the previous modeling work (Bickle et al., 2007; Chadwick and Noy, 2010; Singh et al., 2010; Cavanagh, 2013) pointed out the need and justifications for more feeders even though both Chadwick and Noy (2010) and Singh et al. (2010) used a single feeder in their models.

We experimented with the scenario of two feeders in this study. The main feeder is above the injection point in Layer 9. A second, smaller feeder was added at the coordinates x = 438,925 and y = 6,472,250, which is beneath one of the thickest areas of the CO_2 plume in the north ridge. This thick area appears in the 2004 and 2006 seismic survey maps, but not in the 2001 map. For the purpose of numerical experiments, we assumed that the second feeder started to contribute from January 1, 2002. 100% mass of CO_2 was distributed to the main feeder during 1999-2001; starting from 2002, 85% mass was assigned to the main feeder and 15% mass was assigned to the second feeder. The reservoir temperature used was 33.2 ^{o}C and no CH_4 was included in the model.

Figure 4b shows that using two feeders improved CO_2 migration to the north ridge. **Figure 5c, d** show simulated plume developments using GEM$^{®}$ and TOUGH2, respectively.

Although there is marked improvement for match with plume migration, there is no sufficient seismic evidence to support for a second feeder and its spill rate, with the exception of the CO_2 plume thickness information interpreted from seismic data (Chadwick and Noy, 2010). Therefore, the model with two feeders is a forced model to favor the history match and a numerical experiment used to test the idea suggested by previous modeling work.

5.2. Topography Uncertainty and its Effect on the CO_2 Plume

The simulated CO_2 for this study is always outside of the east or west boundary interpreted from seismic data (**Fig 11**). Varying temperature, pressure, CO_2 spill rate, and CH_4 content did not remediate the mismatches. Chadwick and Noy (2010), Singh et al. (2010), Cavanagh (2013), and Haukaas et al. (2013) obtained similar results although they employed different simulators and model settings in comparison with ours. Therefore, we inferred that the mismatch in east or west boundary resulted from topographic interpretation errors and they cannot be eliminated by adjusting modeling parameters.

At Sleipner, the depths of Layer 9 top were calculated using a laterally uniform "layer-cake" overburden velocity model based on average velocities from a number of wells in the vicinity, but these wells are too spatially scattered (typically more than 2 km apart) and the velocities of the wells in the vicinity are different (Chadwick and Noy, 2010). Chadwick and Noy (2010) analyzed the velocity difference between pairs of wells, which indicates significant velocity variation, with differences up to more than 50 ms^{-1}. Therefore, the topography of Layer 9, which was interpreted from average velocities of the adjacent wells, can carry significant uncertainties. These uncertainties could contribute to the apparent mismatches between simulated and seismic CWC outlines.

In order to further explore possible local topographic errors in the east and west boundary, we analyzed our simulated CO_2 plume in Layer 9 in detail. In **Fig 11** (a)-(b), two vertical profiles are described along grid cell J51 and J62, respectively. The positions of these profiles are shown in **Fig 11 (c)**. In the profiles, the red solid lines represent the simulated CO_2 plume bottoms and the black vertical dashed lines indicate the locations of seismic CWC from the areal maps.

In the profile along J51 (**Fig 11a**), the main CO_2 plume body, with a thickness of 5~6 m, filled in the structure trap that manifested by the topographic ridge of the top of Utsira surface. However, both sides of the simulated plume extend outside of the CWC of ~150 m. Nevertheless, the CO_2 layer outside the CWC is thin (Note that the vertical scale is greatly exaggerated in **Fig 11)**. Along J62, we see a similar pattern. The simulated main CO_2 plume body was within the topographic ridge. However, the simulated CO_2 plume matched with the observation on the west side, but extended too far east to the right. Again, the CO_2 layer outside the CWC is thin. One could speculate that topography errors of approximately ~±1 m would not affect the boundaries of the main CO_2 plume body. Therefore, the simulated thick CO_2 plume body matched with seismic CWC well, as we showed in this study. On the other hand, the same topography errors of approximately ~±1 m on the fridges of the CO_2 plume would have resulted in large relative errors in topography, which would in turn lead to apparent mismatches between simulated and observed CWC. However, these overspill areas are characterized by a thin layer of CO_2. As a result, the matches between simulated and observed CWC are better than it appears to be on a plane view.

From these analyses, we can conclude that (1) we need to be careful in judging what constitutes a good match between simulated and observed plumes. On a plane view, simulated

CO_2 plume spilled over outside of CWC on the west and east, which obscures the excellent match for the main CO_2 plume body. The case study at Sleipner is therefore useful in developing regulatory criteria for quality modeling work. (2) These local mismatches of plume boundaries cannot be eliminated by adjusting parameters other than local topography. Resources should not be directed to such efforts.

5.3. Geochemical Processes

Most previous modeling studies incorporating geochemistry have used idealized aquifers. Can models with realistic and complex topography have locations of enhanced geochemical reactions? Can this feedback to CO_2 plume migration? To explore these questions we constructed a test case with geochemistry. There is no formation water composition available at the Sleipner site and previous studies used Oseberg formation water as a substitute for the Sleipner site (Audigane et al., 2007; Gaus et al., 2005). Johnson et al. (2004b) slightly modified the chemical composition of Oseberg formation water in order in better accordance with the mineralogy of Utsira formation. In this study, we adopted the formation water composition from Johnson et al. (2004b) (**Table 3**). Because the simulation time from 1999-2010 is short and the reaction rate of calcite is much higher than silicate minerals, the only active mineral considered in the current study is calcite. The volume fraction of calcite (6%) is based on Chadwick et al. (2004). The kinetic parameters for calcite dissolution are rate constant of $10^{-5.81}$ mol/m^2/s at 25 ^{o}C, activation energy of 23.5 kJ/mol (Palandri and Kharaka, 2004) and reactive surface area of 88 m^2/m^3 (Nghiem et al., 2009).

Figure 12 (middle and lower panel) indicates that calcite reaction favors the topographic high in Layer 9. The percentage of calcite dissolution can be up to ~1% which is comparable with the value ~1.9% derived from Audigane et al. (2007)'s simulation for Sleipner with ToughReact. After CO_2 injection, a certain amount of CO_2(g) will dissolve into the brine, and will make the brine acidic and corrosive to all minerals in the formation resulting in the calcite dissolution. The solute (such as Ca^{+2}, HCO_3^-) in the brine is transported by advection, diffusion, and dispersion processes, which cause the calcite dissolution region to be larger than the CWC (**Fig 12 upper panel**). Calcite can achieve equilibrium quickly and the dissolved quantity is only of ~1% and porosity only increases by ~0.0004. Hence we can ignore the geochemical process in short time simulation.

5.4. Plume Migration Prediction Uncertainty

To test the forecasting ability of our calibrated model, we made model prediction to 2018. When the model was calibrated, the 2010 seismic data were not available, and hence the 2010 data were not part of the calibration and can be good criteria to assess the model. In 2010 (**Fig 13**), the simulated CWC approximately matches with the observed plume outline in south and north.

We also made predictions of CO_2 plumes to 2018 using the two-feeder test case. The predicted plumes from this test case are much smaller than those from the model with CH_4 described above. The calibrated model comparing to the two-feeder test case has a slightly higher temperature (33.5 ^oC versus 33.2 ^oC) and CH_4 (2.4 % versus 0% CH_4). With time, CO_2 plumes predicted from these two models diverge in sizes and distributions. This shows promises that non-unique models can be verified and discriminated with new observations.

6. CONCLUSIONS AND REMARKS ON MULTI-PHASE REACTIVE FLOW

In order to simulate CO_2 plume migration in the uppermost layer (Layer 9) of the Utsira Sand in the Norwegian North Sea, we applied two multi-phase compositional simulators to the Sleipner Benchmark model and calibrated the model against the time-lapsed seismic monitoring data from 1999, 2001, 2002, 2004, 2006, 2008, and 2010. Calibration against plume outlines, specifically the CO_2-water contacts, which are based on the geophysical monitoring data, was accomplished by introducing permeability anisotropy, adjusting reservoir temperature, and taking into account the CH_4 impurity in the CO_2 stream at Sleipner.

Our modeling results show:

(1) The simulated CO_2-water contacts approximately matched with the observed areal extent of the CO_2 plume in 1999, 2001, 2002, 2004, 2006, and 2008 and showed improvements over previous models. To quote Cavanagh (2013): “These (previous) models have failed to quantitatively or qualitatively reproduce the plume morphology to date.” Here, our model was generally able to match the elongated, northward extension of the observed plume.

(2) The approximate history match at Sleipner was achieved by calibrating the model against CO_2-water contacts delineated by seismic data with adjustments of permeability (k), reservoir temperature (T), and CH_4 composition in the CO_2 streams. An increase of N-S permeability is justified by the sedimentary geology of the site and the presence of an N-S trending CO_2 plume. Reservoir temperature and CH_4% used in the model are within the ranges of reported values in the literature. However, the model is not unique. Many combinations of k, T, and CH_4 would produce similar matches, and other possibilities that would have improved the development of an N-S elongated CO_2 plume, such as a slight tilting of the surface of Utsira top to the south, were not considered.

In general, because the CO_2 stream at Sleipner has gas like properties, subtle adjustments of parameters that facilitate CO_2 migration to the north would result in better history matches. However, adjusting only one parameter at a time, as those in previous modeling efforts, would not lead to an N-S elongated CO_2 plume when the adjustment is within the reported ranges. This study shows that it must be a combination of several sensitive parameters, adjusted within reported ranges, to produce an N-S elongated CO_2 plume.

(3) Although many parameters are uncertain, which leads to uncertainness of the simulated plume extent, the predicted fate of CO_2 at Sleipner nevertheless fell within a narrow band, ~93±2% structural/hydrodynamic trapping and ~7±2% solubility trapping.

(4) The model-predicted gas saturation, thickness of the CO_2 accumulations in Layer 9 through time, and the overall dissolved CO_2 in brine (solubility trapping) versus supercritical CO_2 (hydrodynamic trapping), none of them are calibration targets, all matched well with estimates from geophysical data interpretation reported in the literature (e.g., Chadwick and Noy, 2010). In particular, approximate estimates of the percentage of CO_2 which is dissolved into brine (5-10%) have been made based on seismic data interpretation (Chadwick and Noy, 2010). These solubility estimates are comparable to the about 7% in the simulation model. Caution must be exercised for these comparisons, however. These estimates in the literature (Chadwick and Noy, 2010) are not direct observations but interpretations with a widely ranging uncertainties, and the agreements could be fortuitous.

(5) Detailed analysis of the topography in the Benchmark Model and positions and extents of the simulated CO_2 plume show much better match between CWC and boundaries of the main CO_2 plume than what appears on the plane view (**Fig 5b**). The overspill outside of the CWC on the east and west fringes of the plume constitute a thin CO_2 layer, which could result

from errors of seismic interpretation of the topography. On one hand, this shows that the criterion of a good match cannot be simply a comparison between observed and simulated plume outlines. On the other hand, it would be a futile effort to attempt to achieve a perfect match. Our study shows that adjusting other parameters other than topography would not reduce the overspill areas.

(6) Model simulations show the feedback between topography and geochemical reactions. While calcite dissolution reactions concentrated in the topographic highs, only up to ~1% calcite was dissolved and porosity only increased by ~0.0004. Therefore, we can safely ignore the geochemical reactions in model structure for short time simulation.

In conclusion, it appears that we were able to use widely available reservoir simulation tools to simulate multiphase flow at Sleipner and reproduce an N-S elongated CO_2 plume. However, our model is at best a modest improvement over the previous models and a work in progress. The adjustments of parameters need to be verified with new observations. With more observations, this model will certainly be superseded.

Acknowledgement

We acknowledge the support of Computer Modeling Group for providing complementary software for education purposes. We thank Per Aagaard, Thanh Nguyen, Andrew Chadwick, and Andrew Cavanagh for discussions and Laura Brant, Sean Miranda, Michael Hamburger, and Ruth Droppo for editorial and graphic assistance.

Part I Tables

Table 1: Parameters Used in This Study

Parameters	Base Case	Range	References and comments
Reservoir geometry (depth to the reservoir top and reservoir thickness)	Statoil Benchmark model		Sleipner Benchmark
Porosity for Utsira and Shale units	~34-36%	~34-36%	Geophysical logs from 300+ wells (gamma-ray, sonic, density, resistivity and neutron logs); Sleipner Benchmark
Caprock permeability *ki*	~0.001 Millidarcy	~0.001 Millidarcy	Sleipner Benchmark
Utsira permeability *ki*	~2 Darcy	~2 Darcy	Sleipner Benchmark
Shale permeability *ki*	~0.001 Millidarcy	~0.001 Millidarcy	Sleipner Benchmark
Vertical permeability anisotropy k_k:k_i	0.1		Sleipner Benchmark
Horizontal permeability anisotropy *kj*:*ki*	5	1~10	(Chadwick and Noy, 2010)
L9 model area	18 km^2		Sleipner Benchmark
Top L9 depth	817.3	802.2-840.5	Sleipner Benchmark
L9 thickness	11.3 m	3.5-26.3	Sleipner Benchmark
Critical gas saturation	0.02		Sleipner Benchmark
Connate water saturation	0.89		Sleipner Benchmark
Residual gas saturation	0.21		Sleipner Benchmark
Reservoir temperature	33.5 °C	29 °C ~ 37 °C	(Boait et al., 2011; Cavanagh and Haszeldine, 2014)
Reservoir pressure	8.3 MPa at 820 m as reference	8.0~8.6 MPa	(Chadwick et al., 2005; Boait et al., 2011)
Hydrostatic gradient	Assumed hydrostatic equilibrium		Sleipner Benchmark
CO_2 injection rate into the Layer 9			Based on seismic data and injection rate to the whole reservoir by Statoil
Main feeder Layer 9	x = 438,516; y = 6,471,210		Sleipner Benchmark (Singh et al., 2010)
Secondary feeder	x = 438,925; y = 6,472,250		Assumed based on CO_2 thicknesses derived from reflection amplitudes Chadwick and Noy, (2010b)
Boundary conditions	Dirichlet boundary conditions (infinite large volume for the boundary grid cells)		(Pruess, 2004)
Second feeder CO_2 injection volume	15% since 2001	0-20% since 2001	This study

CO_2 density	637 kg/m^3 at reservoir temperature and pressure	Calculated with GEM®.
Pore Water Salinity	33500 ppm	Sleipner Benchmark
Water density	1021 km/m^3	Calculated based on salinity

Table 2. Layer 9 temperature and pressure ranges reported in literatures and used in our analysis

References	Temperature (°C)	Pressure (MPa)
(Aines et al., 2011)	29.4	8.5
(Bickle et al., 2007)	35	8.0
(Chadwick et al., 2005)	29	8.6
Boait et al. (2011)	29	8.0
Cavanagh and Haszeldine (2014)	31-37	8.1

Table 3: Aqueous Concentrations (in Molality) for Utsira Formation Water

Component	Adopted value[a]
Na	0.4520
K	0.0053
Ca	0.00742
Al	1.3×10^{-8}
Si	1.66×10^{-4}
Cl	0.5213
C	0.00232
pH	6.5
Temp (°C)	33[b]

[a] Johnson et al. (2004). [b] Assumed values.

Part I Figures

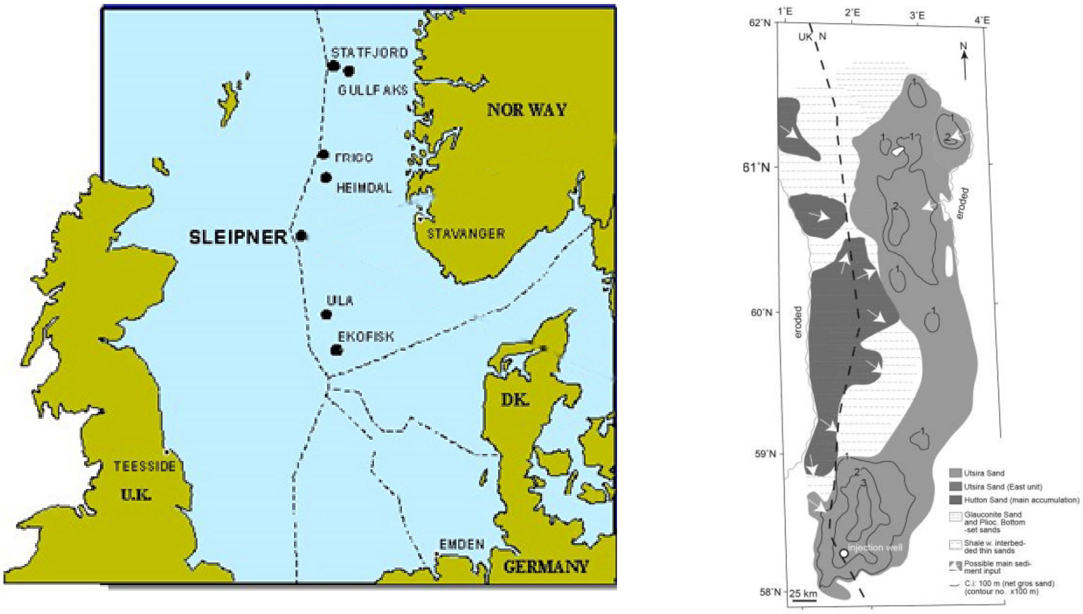

Figure 1. Left panel: Location of the Sleipner fields (after Holloway et al., 2005). Dots with names other than Sleipner refer to other oil and gas fields nearby. Right panel: Isopach map (100 m contour interval) of Neogene sandy units and sediment input directions (Gregersen and Johannessen, 2007).

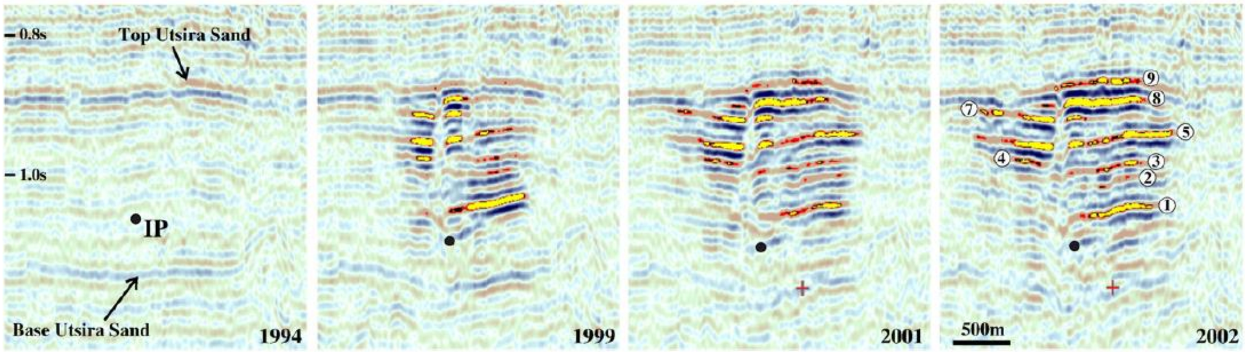

Figure 2. Time-lapse seismic images of the CO_2 plume at Sleipner. Seismic reflection profiles through time with the nine CO_2 accumulation horizons numbered in the 2002 profile. The pre-injection profile shows the base and top of the Utsira Sand but little detail within the reservoir. The subsequent post-injection profiles show bright reflections where CO_2 is ponding under thin mudstones. Note the pushdown of the basal Utsira Sand reflection resulting from low velocity of CO_2 in the reservoir and development of a low amplitude vertical ‘chimney’ just to left (south) of the injection point (IP) presumed to be the main vertical conduit of CO_2 in the plume. Vertical scale is in two-way travel time (Bickle et al., 2007).

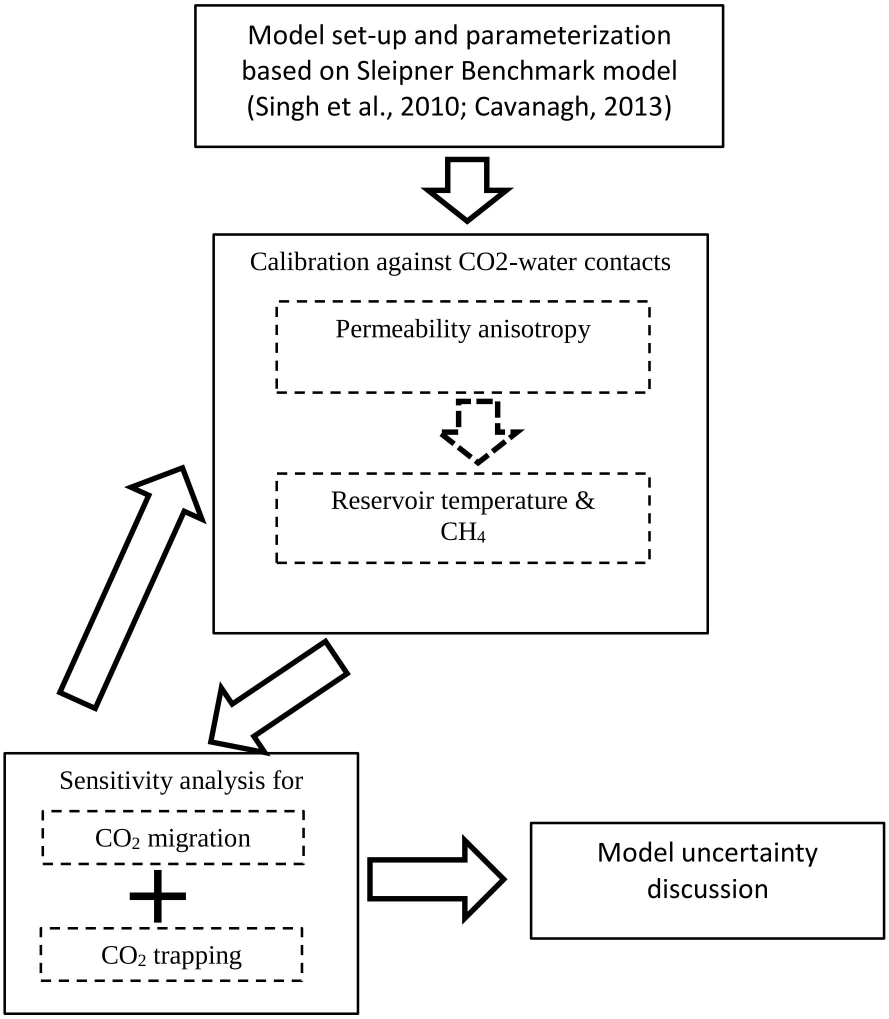

Figure 3. Workflow for CO_2 sequestration modeling and analysis of sensitivity and uncertainty at Sleipner.

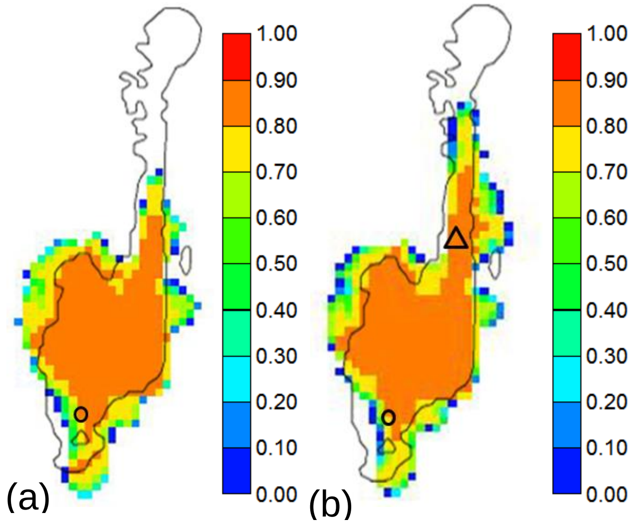

Figure 4. The extents of CO_2 plume in 2006. Black outlines represent the observations (Chadwick and Noy, 2010b). (a) results of simulation in this study with k = 2 Darcy east-west, 10 Darcy north-south, and one feeder for Layer 9; (b) simulation in this study with 100% CO_2 mass into the main feeder (circle) during 1999-2001, 85% CO_2 volume injected into the main feeder and 15% into the second feeder (the triangle) starting from 2002, k = 2 Darcy east-west and 10 Darcy north-south.

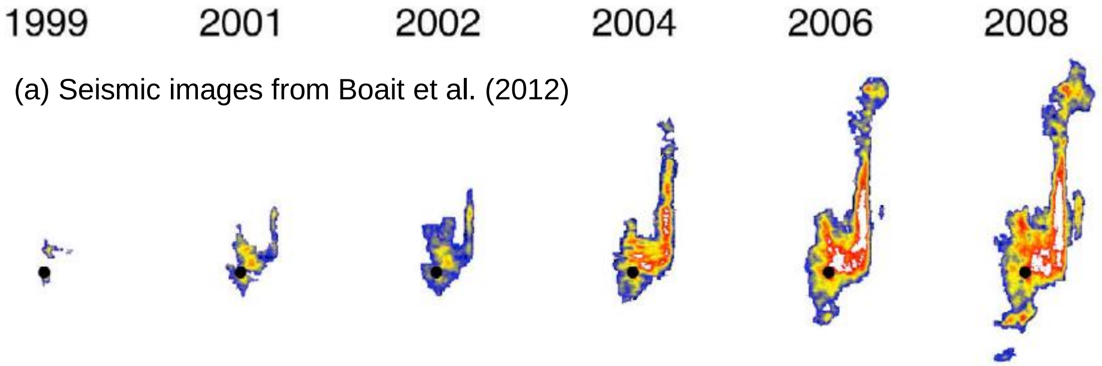

(a) Seismic images from Boait et al. (2012)

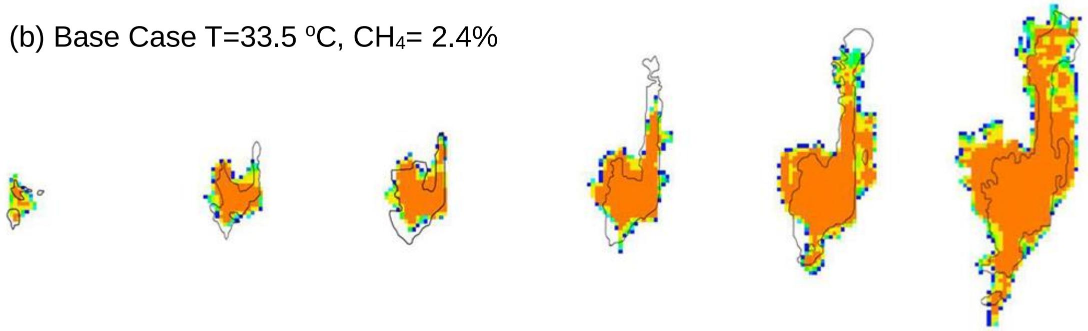

(b) Base Case T=33.5 °C, CH_4= 2.4%

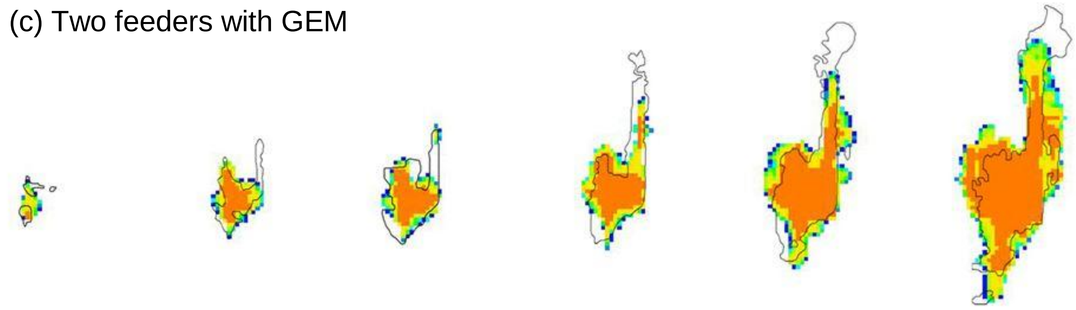

(c) Two feeders with GEM

(d) Two feeders with TOUGH2

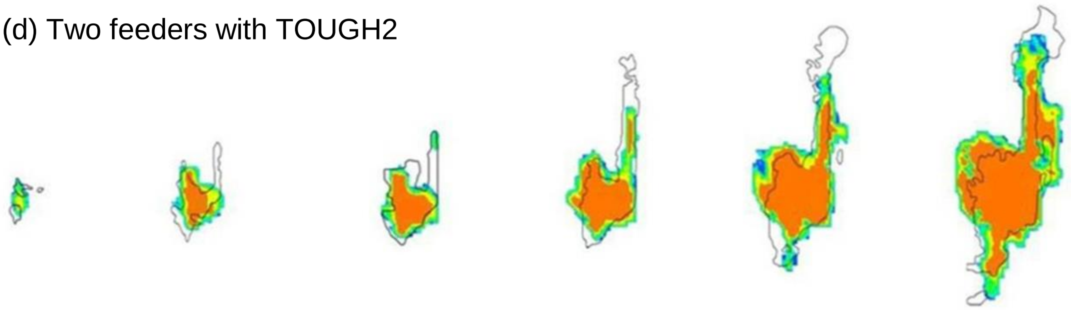

(e) Cavanagh (2013) Invasion percolation migration model

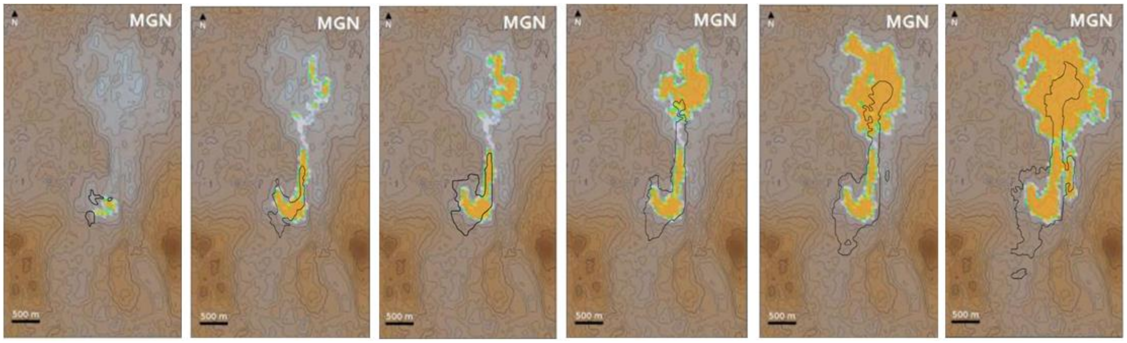

(f) Singh et al. (2010) CO_2 Black Oil Simulator using up-scaled relative permeability curves

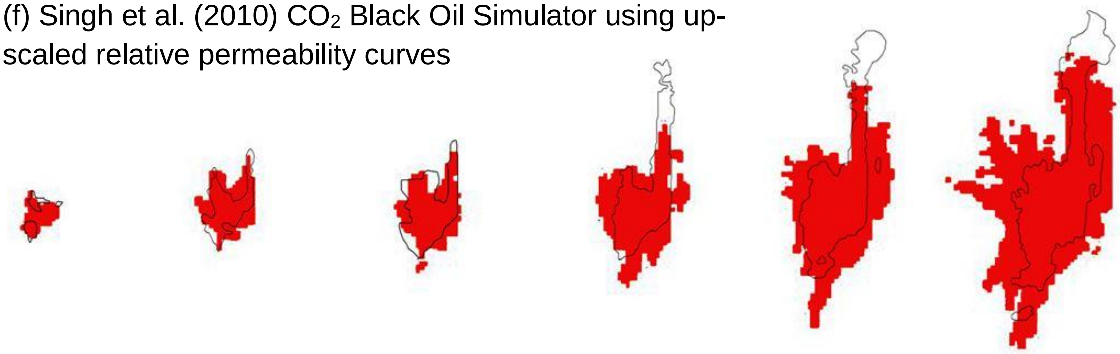

(g) Singh et al. (2010) CO_2 Black Oil Simulator using the Vertical Equilibrium option

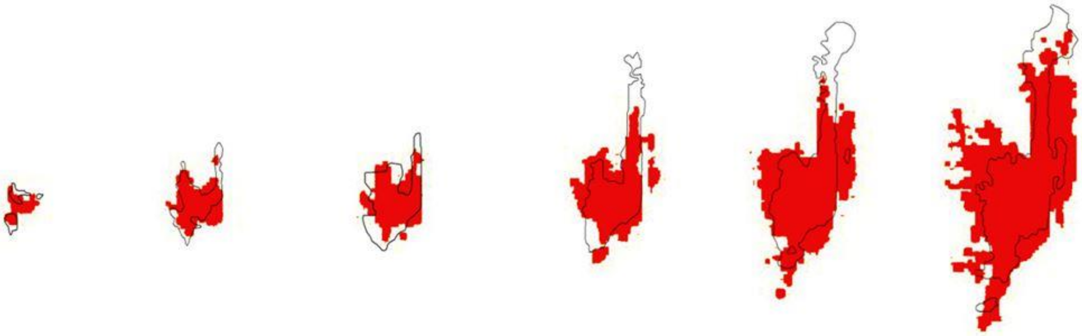

(h) Haukaas et al. (2013)

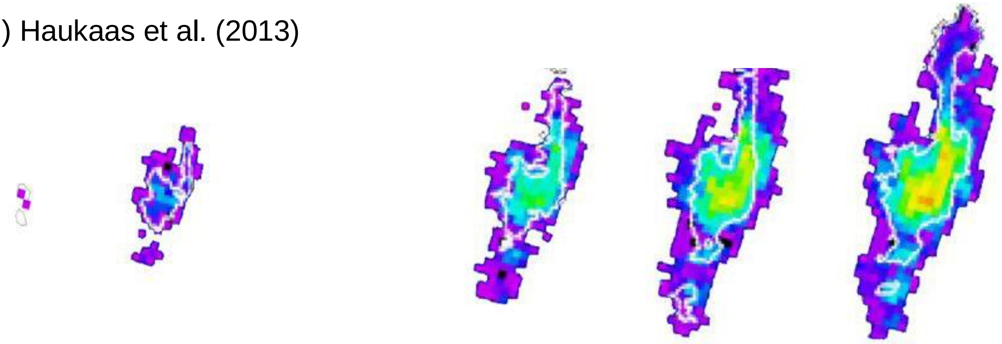

Figure 5. Comparison of simulated time-series CO_2 plume extent with observed plumes from seismic amplitude data (Boait et al., 2012).

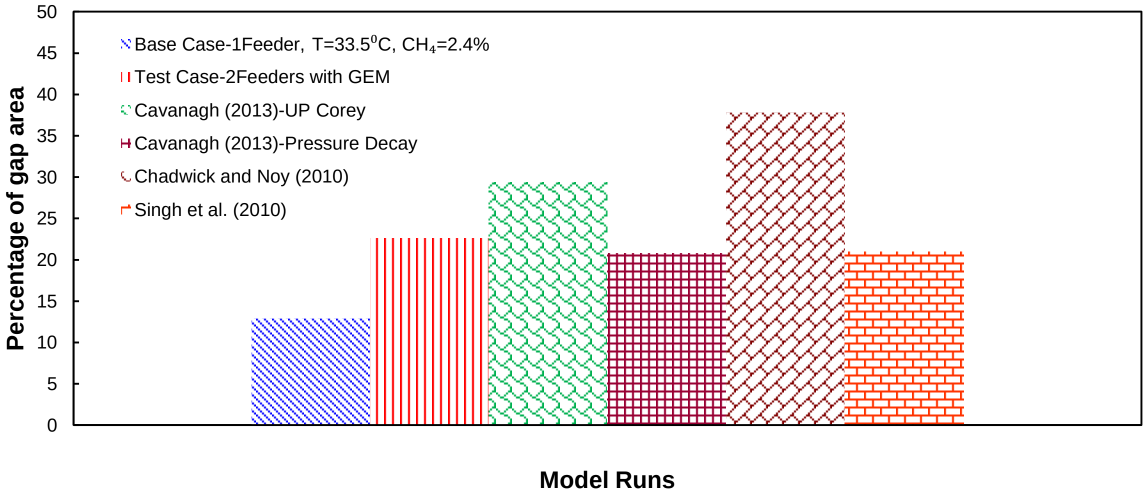

Figure 6. Percentages of areas within the CO_2 plume outline (delineated by seismic data) that were not filled by CO_2 in model runs in 2006. The bars (left to right) are from (1) Base Case in this study; (2) test case with 2 feeders in this study, simulated with GEM; (3) from Cavanagh (2013), employing a black oil simulator to the Benchmark model with upscaled Corey curves; (4) from Cavanagh (2013), with a compensation period of several decades until the overpressure has dissipated; (5) from Chadwick and Noy (2010), with TOUGH2; and (6) Singh et al. (2010), with Eclipse 300 with Corey exponents of 1.0.

(a) Test Case-Temperature

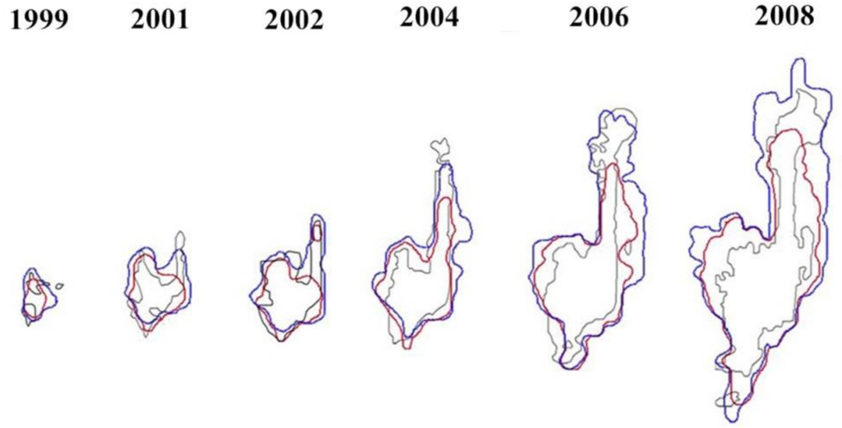

(b) Test Case-Pressure

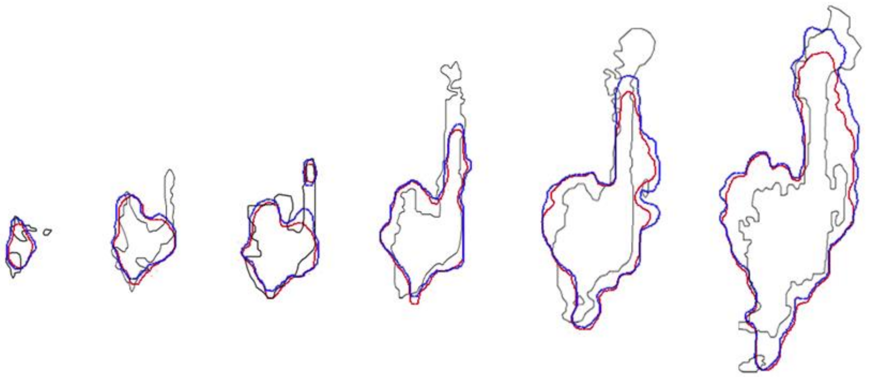

(c) Test Case-20% more CO_2 spill into Layer 9

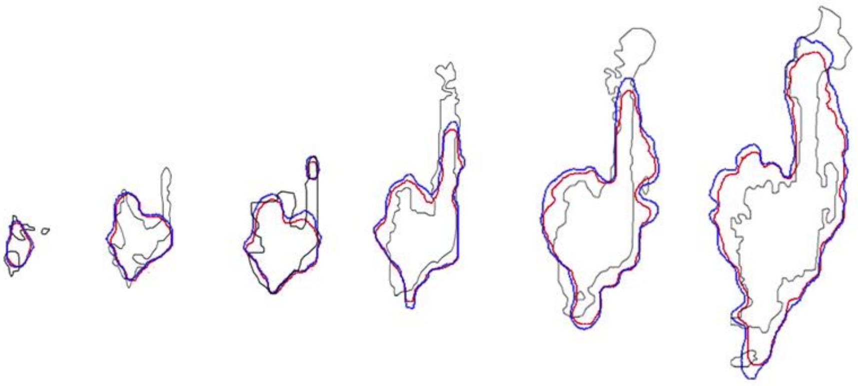

(d) Test Case-4% CH_4

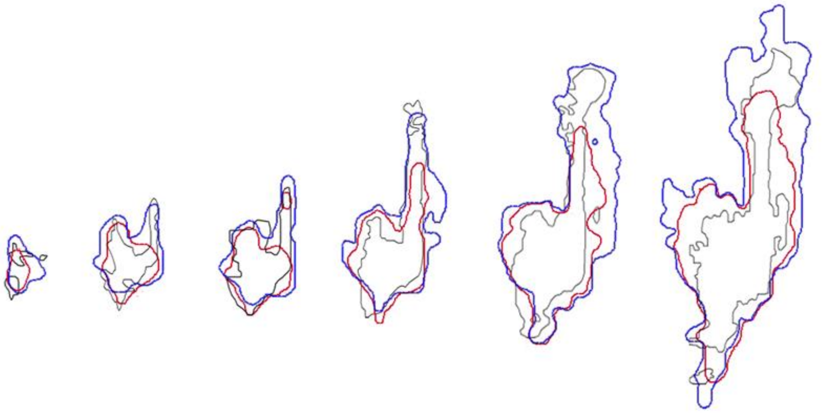

(e) Test Case-1 Feeder, T=35 °C, CH_4=1.8%

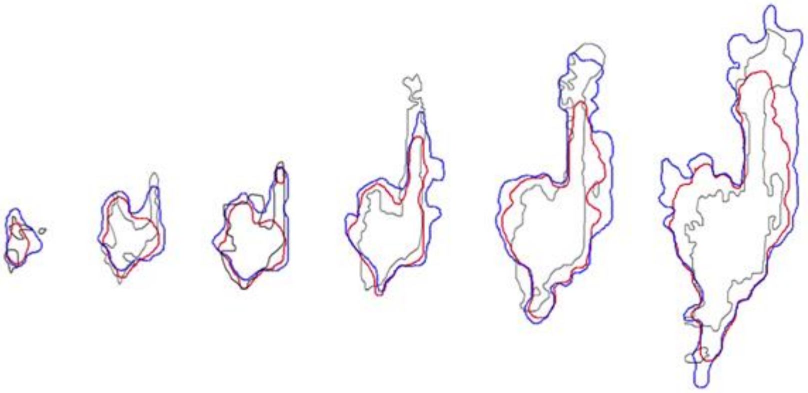

(f) Test Case-1 Feeder, T=34 °C, CH_4=2.7%

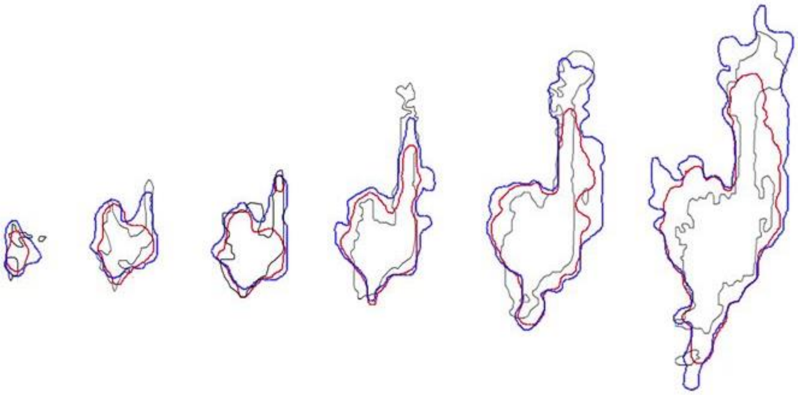

Figure 7. Results of sensitivity and uncertainty analyses. The black outlines represents CWC observed from 4D seismic (Boait et al., 2012). Red lines represent the Base Case. Blue lines in (a)-(f) represent simulated results of test cases.

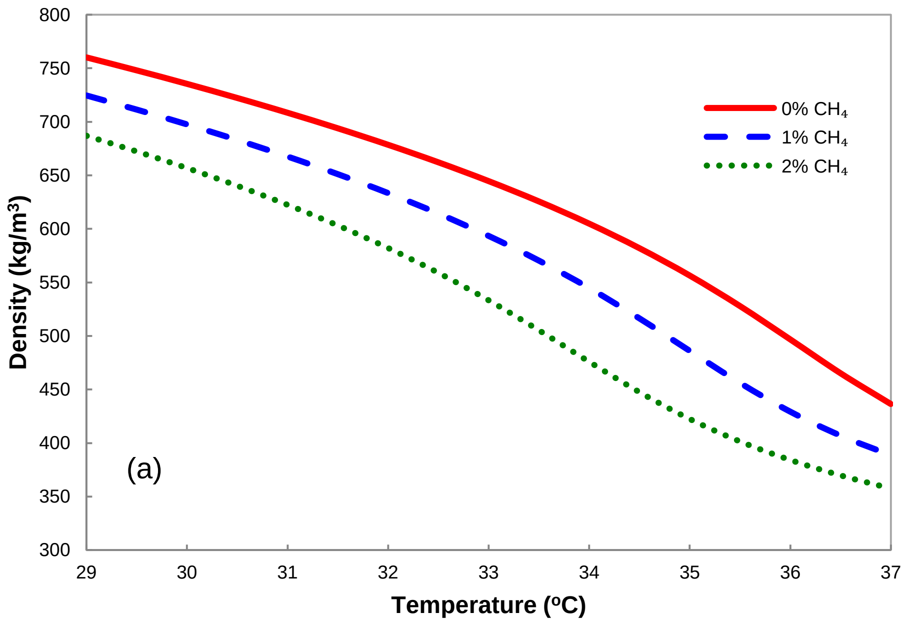
Density (kg/m^3)
800
750
700
650
600
550
500
450
400
350
300
29
30
31
32
33
34
35
36
37
Temperature (ºC)
0% CH$_4$
1% CH$_4$
2% CH$_4$
(a)

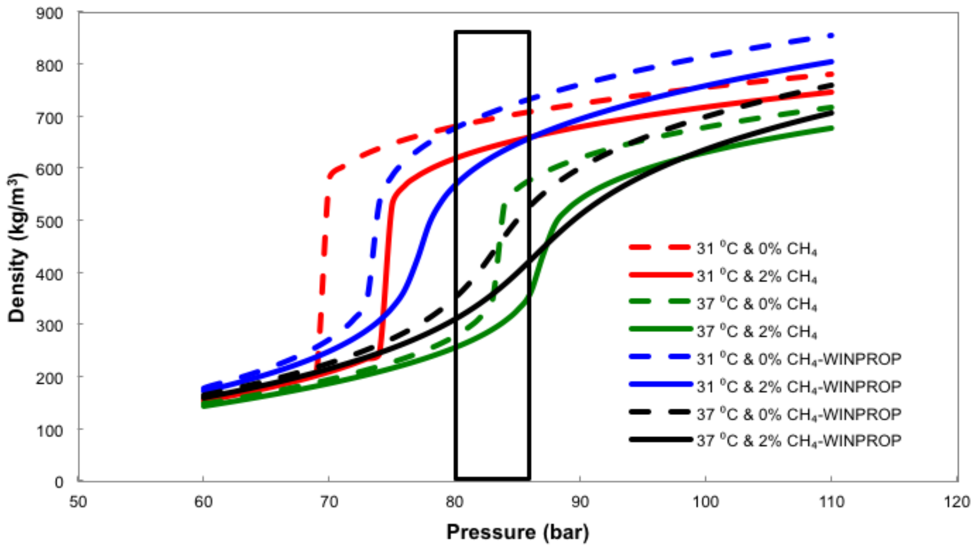
Density (kg/m^3)
900
800
700
600
500
400
300
200
100
0
50
60
70
80
90
100
110
120
Pressure (bar)
31 ^{0}C & 0% CH$_4$
31 ^{0}C & 2% CH$_4$
37 ^{0}C & 0% CH$_4$
37 ^{0}C & 2% CH$_4$
31 ^{0}C & 0% CH$_4$-WINPROP
31 ^{0}C & 2% CH$_4$-WINPROP
37 ^{0}C & 0% CH$_4$-WINPROP
37 ^{0}C & 2% CH$_4$-WINPROP

(b)

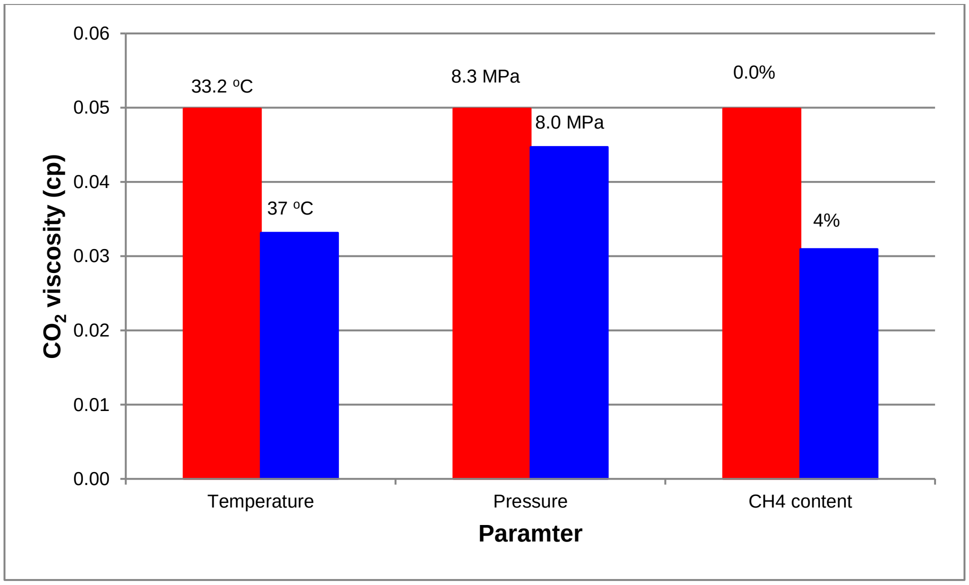

Figure 8. Variations of CO_2 density (a,b) and viscosity (c) with temperature, pressure, and CH_4 content. All density and viscosity values were computed with GEM® except the density values in (b). In (b), density values of the CO_2-CH_4 mixture (lines with notation of "WINPROP")were predicted with SAFT2, using parameters of CO_2 and CH_4 from previous work (Tan et al., 2006; Ji and Adidharma, 2010). To predict the effect of CH_4 on the density of CO_2, the mixing rules without any adjustable parameters were used in SAFT2. The box is the range of pressure in Layer 9 reported in literature.

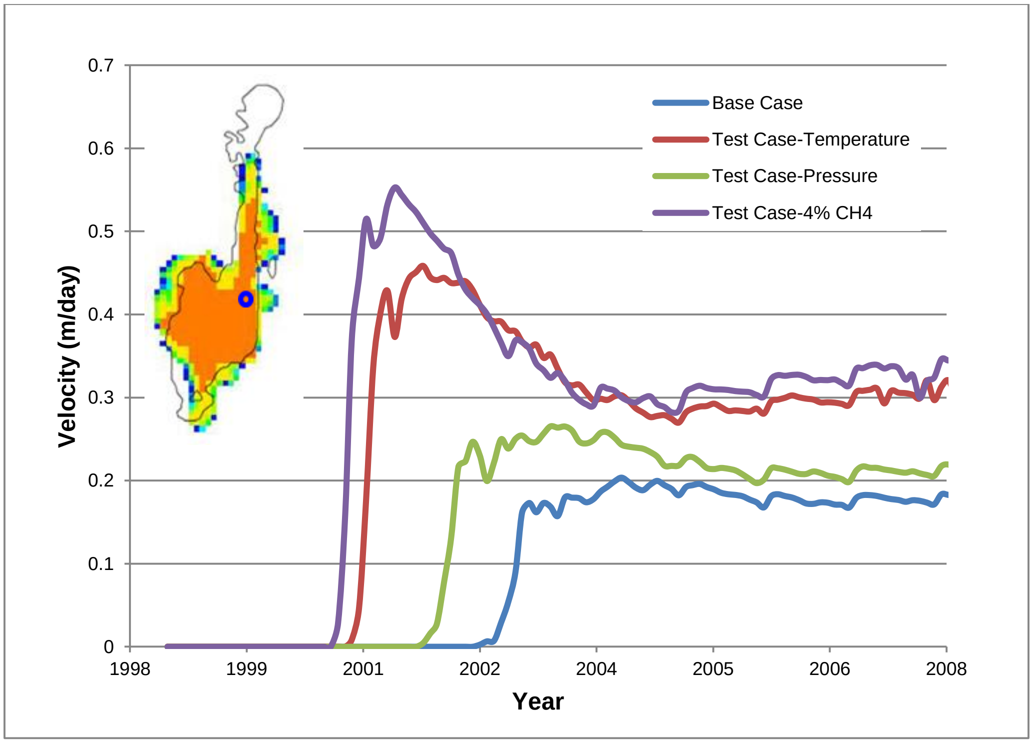

Figure 9. Comparison of CO_2 fluid velocities in various test cases. Flow velocity along the south-north direction at the position shown in plume diagram.

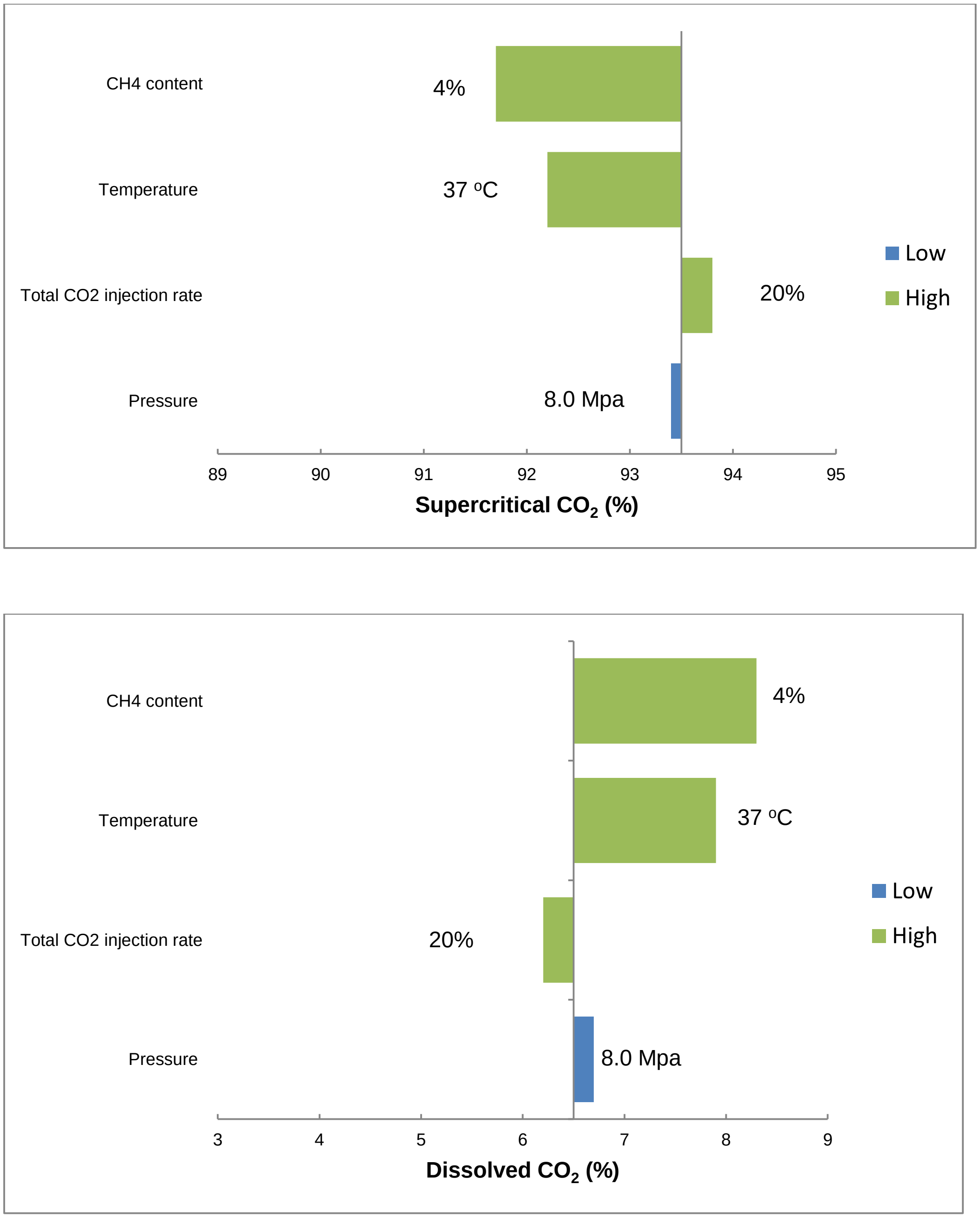

Figure 10. Sensitivity of model parameters on simulated trapping mechanisms. Upper panel: tornado diagram for supercritical CO_2 (structural or hydrodynamic trapping); lower panel: tornado diagram for dissolved CO_2 (solubility trapping). The lines represent the simulation results for the Base Case (~93.5% of total injected CO_2 for structural trapping and ~6.5% for solubility trapping); green color denotes parameter values higher than those in the Base Case and blue color lower than those for the Base Case. Parameters used in the Base Case are listed in Table 1.

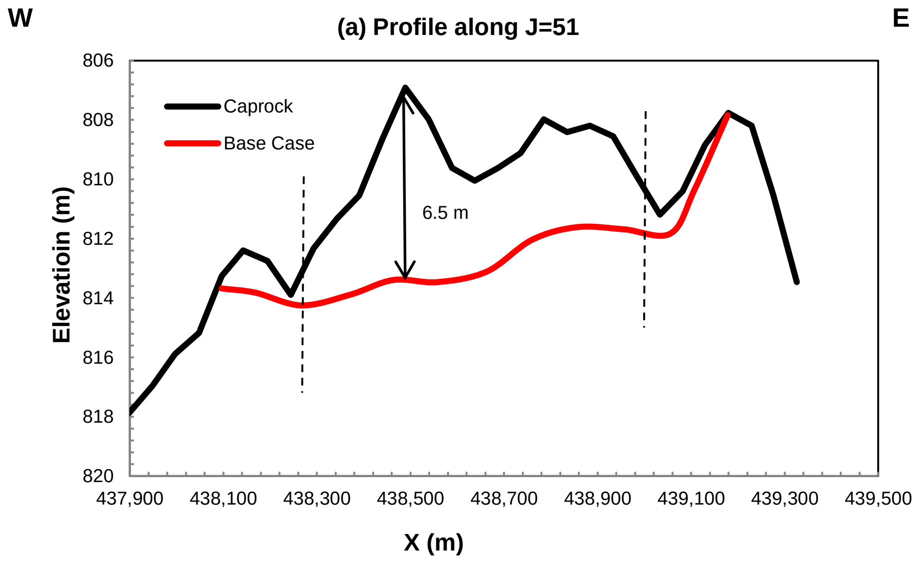
W
(a) Profile along J=51
E
Caprock
Base Case
6.5 m
Elevatioin (m)
806
808
810
812
814
816
818
820
437,900
438,100
438,300
438,500
438,700
438,900
439,100
439,300
439,500
X (m)

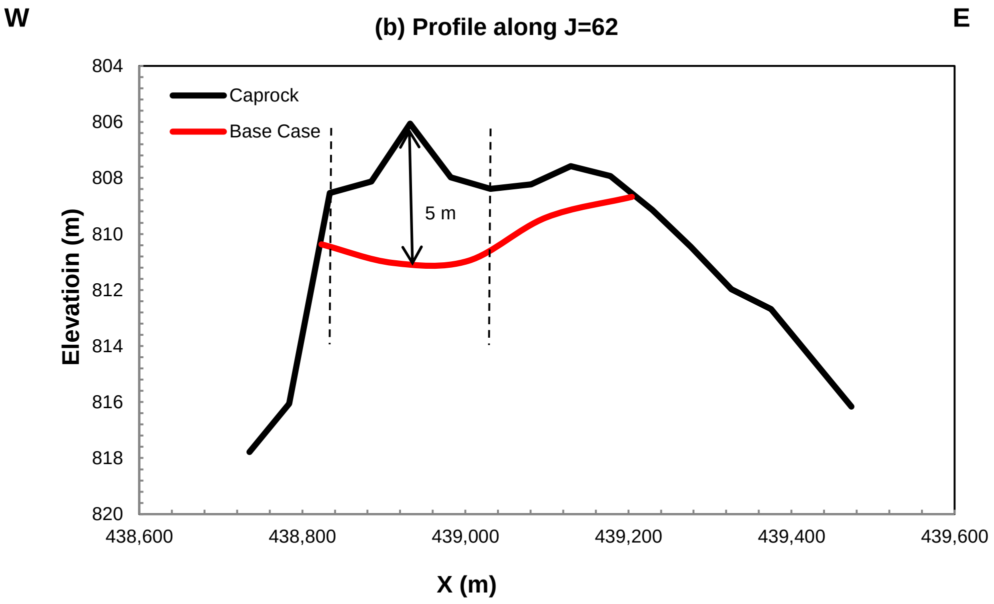
W
(b) Profile along J=62
E
Caprock
Base Case
5 m
Elevatioin (m)
804
806
808
810
812
814
816
818
820
438,600
438,800
439,000
439,200
439,400
439,600
X (m)

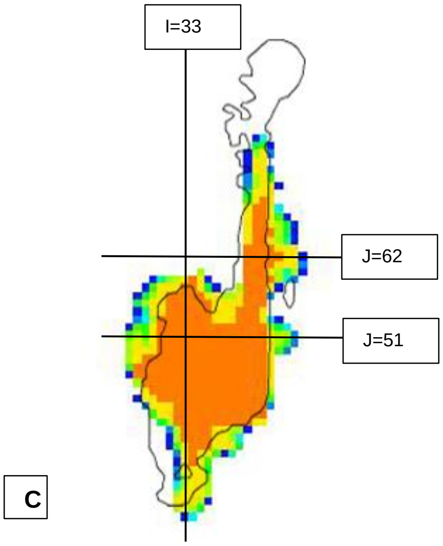

Figure 11. Vertical profiles of the CO_2 plume in Layer 9 in 2006. The red solid lines represent the simulated bottom of the CO_2 plume in the Base Case; the black solid lines are the topography of the caprock bottom in the model. The vertical black dash lines represent the boundary of CO_2 plume. (c) locations of the profiles. The black outlines denoted CWC interpreted from seismic data (Boait et al., 2012).

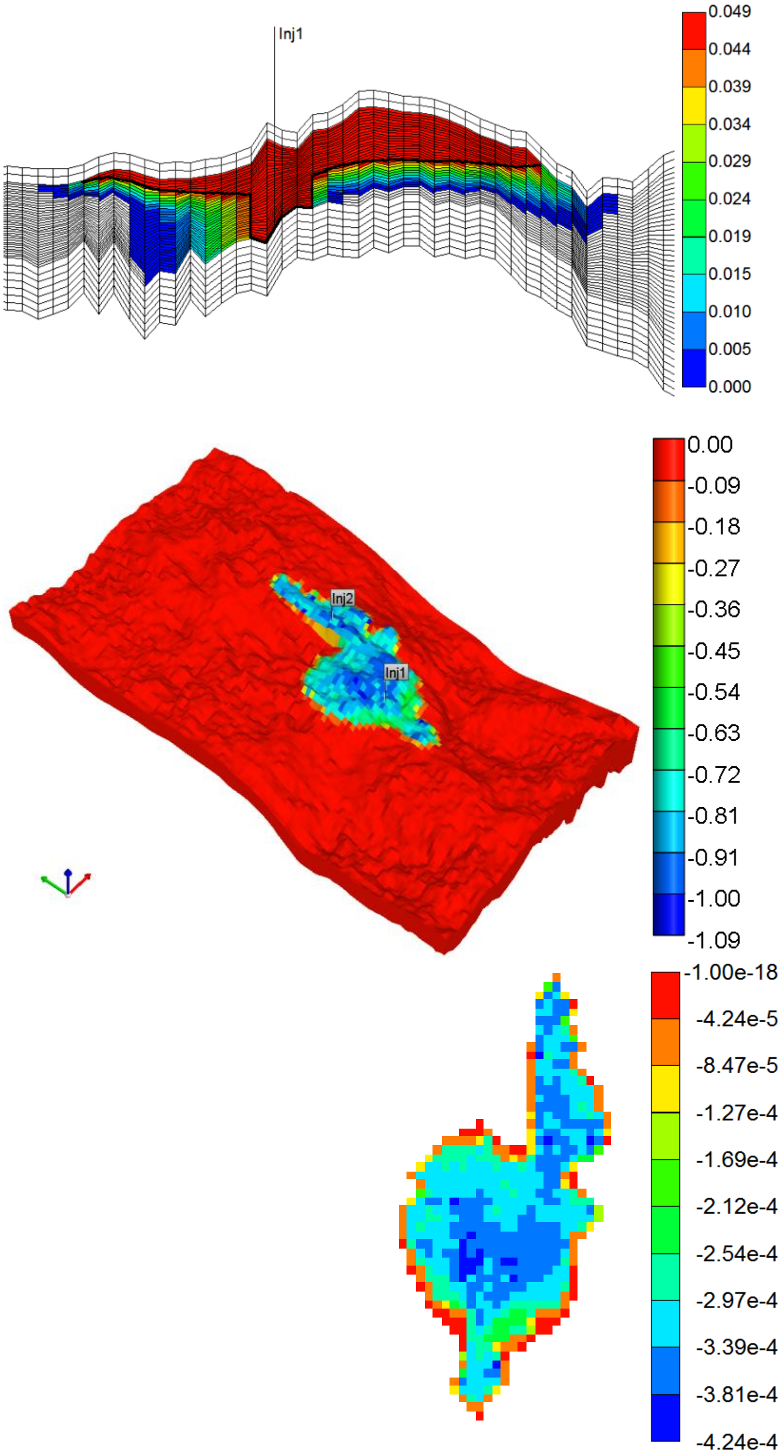

Figure 12. Upper panel: The concentration (molality) distribution of HCO_3^- at the crossing section I=33 in 2006. The blank area in the sandstone indicates the initial HCO_3^- concentration in 1999. The top 2 sub-layer and bottom 7 sub-layer of block grid are shale layers; other sub-layers are the sandstone. The bold black line represents CWC

boundary derived in the Base Case. Middle panel: The percentage of calcite dissolution at the top sub-layer of Layer 9 in 3D in 2006. Lower panel: Porosity change distribution at the top sub-layer of Layer 9 in 2006. Negative value represents the increase of porosity due to mineral dissolution.

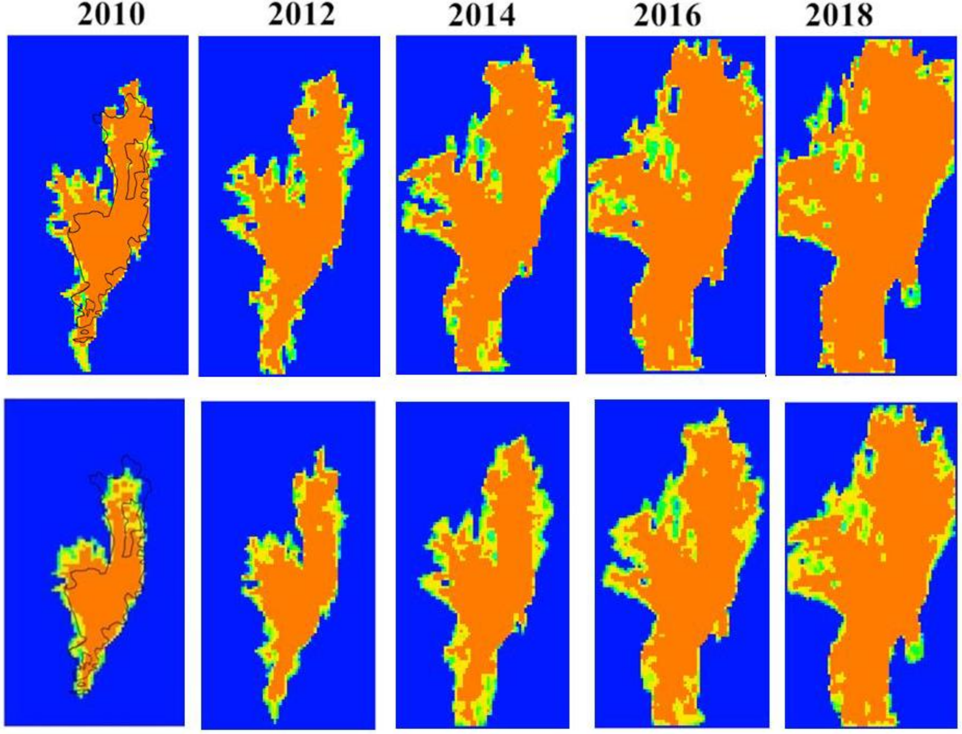

Figure 13. Simulated time-series of CO_2 plume in the top sub-layer of Layer 9 from 2010 to 2018 with Base Case- 33.5 °C, 2.4% CH_4 (upper panel) and Test Case- 2 two feeders, 33.2 °C, 0% CH_4 (lower panel). The black line in 2010 is the CWC interpreted from the seismic data of Statoil; the blue background color indicates the horizontal range of the mesh grid of the Sleipner Benchmark.

7. REFERENCES CITED

Aines, H., Eiken, O., Nooner, S., Sasagawa, G., Stenvold, T., Zumberge, M., 2011. Results from Sleipner gravity monitoring: Updated density and temperature distribution of the CO_2 plume. Energy Procedia 4, 5504-5511.

Altunin, V.V., 1975. Thermophysical properties of Carbon Dioxides. Publishing house of Standards, Moscow.

Andersen, G., Probst, A., Murray, L., Butler, S., 1992. An accurate PVT model for geothermal fluids as represented by the H_2O-CO_2-NaCl mixtures, Proceedings 17th Workshop on Geothermal Reservoir Engineering, Stanford, CA.

Arts, R., Chadwick, A., Eiken, O., Thibeau, S., Nooner, S., 2008. Ten years' experience of monitoring CO_2 injection in the Utsira Sand at Sleipner, offshore Norway. First Break 26.

Aster, R.C., Borchers, B., Thurber, C.H., 2005. Parameter estimation and inverse problems. Elsevier Academic Press, Burlington, MA, U.S.A.

Audigane, P., Gaus, I., Czernichowski-Lauriol, I., Pruess, K., Xu, T., 2007. Two-dimensional reactive transport modeling of CO_2 injection in a saline aquifer at the Sleipner site, North Sea. American Journal of Science 307, 974-1008.

Baklid, A., Korbol, R., Owren, G., 1996. Sleipner Vest CO_2 disposal, CO_2 injection into a shallpw underground aquifer, SPE Annual Technical Conference and Exhibition, Denver, Colorado, USA, pp. 1-9.

Bickle, M., Chadwick, A., Huppert, H.E., Hallworth, M., Lyle, S., 2007. Modelling carbon dioxide accumulation at Sleipner: Implications for underground carbon storage. Earth and Planetary Science Letters 255, 164-176.

Boait, F., White, N., Chadwick, A., Noy, D., Bickle, M., 2011. Layer spreading and dimming within the CO_2 plume at the sleipner field in the north sea. Energy Procedia 4, 3254-3261.

Boait, F.C., White, N.J., Bickle, M.J., Chadwick, R.A., Neufeld, J.A., Huppert, H.E., 2012. Spatial and temporal evolution of injected CO_2 at the Sleipner Field, North Sea. Journal of Geophysical Research 117, B03309.

Box, G.E.P., Jenkins, G.M., Reinsel, G., 1994. Time series analysis, forecasting and control, 3rd ed. Holden-Day, San Francisco.

Cameron, D.A., Durlofsky, L.J., 2012. Optimization of well placement, CO_2 injection rates, and brine cycling for geological carbon sequestration. International Journal of Greenhouse Gas Control 10, 100-112.

Cavanagh, A., 2011. CO_2 storage simulations: Sleipner calibration and prediction, American Geophysical Union Fall Meeting, San Francisco.

Cavanagh, A., 2013. Benchmark calibration and prediction of the Sleipner CO_2 plume from 2006 to 2012. Energy Procedia 37, 3529-3545.

Cavanagh, A.J., Haszeldine, R.S., 2014. The Sleipner storage site: Capillary flow modeling of a layered CO_2 plume requires fractured shale barriers within the Utsira Formation. International Journal of Greenhouse Gas Control 21, 101-112.

Chadwick, A., Williams, G., Delepine, N., Clochard, V., Labat, K., Sturton, S., Buddensiek, M.-L., Dillen, M., Nickel, M., Lima, A.L., Arts, R., Neele, F., Rossi, G., 2010. Quantitative analysis of time-lapse seismic monitoring data at the Sleipner CO_2 storage operation. The Leading Edge 29, 170-177.

Chadwick, R.A., Arts, R., Eiken, O., 2005. 4D seismic quantification of a growing CO_2 plume at Sleipner, North Sea, in: Dore, A.G., Vining, B.A. (Eds.), Petroleum Geology: North-West Europe and Global Perspectives - Proceedings of the 6th Petroleum Geology Conference. the Geological Society, London, pp. 1385-1399.

Chadwick, R.A., Noy, D., Arts, R., Eiken, O., 2009. Latest time-lapse seismic data from Sleipner yield new insights into CO_2 plume development. Energy Procedia 1, 2103-2110.

Chadwick, R.A., Noy, D.J., 2010. History-matching flow simulations and time-lapse seismic data from the Sleipner CO_2 plume, Petroleum Geology Conference. Geological Society, London, pp. 1171-1182.

Chadwick, R.A., Zweigel, P., Gregersen, U., Kirby, G.A., Holloway, S., Johannessen, P.N., 2004. Geological reservoir characterization of a CO2 storage site: The Utsira Sand, Sleipner, northern North Sea. Energy 29, 1371-1381.

Cheng, P., Bestehorn, M., Firoozabadi, A., 2012. Effect of permeability anisotropy on buoyancy-driven flow for CO_2 sequestration in saline aquifers. Water Resources Research 48, W09539.

CMG, 2009. User's guide GEM. . Computer Modelling Group Ltd.

Court, B., Bandilla, K.W., Celia, M.A., Janzen, A., Dobossy, M., Nordbotten, J.M., 2012. Applicability of vertical-equilibrium and sharp-interface assumptions in CO_2 sequestration modeling. International Journal of Greenhouse Gas Control 10, 134-147.

Doughty, C., Pruess, K., 2004. Modeling supercritical carbon dioxide injection in heterogeneous porous media. Vadose Zone Journal 3, 837-847.

Duan, Z., Sun, R., Zhu, C., Chou, I., 2006. An improved model for the calculation of CO_2 solubility in aqueous solutions containing Na^+, K^+, Ca^{2+}, Mg^{2+}, Cl^-, and SO_4^{2-}. Marine Chemistry 98, 131-139.

Eidvin, T., Rundberg, Y., 2001. Late Cainozic stratigraphy of the Tampen area (Snorre and Vislund fields) in the northern North Sea with emphasis on the chronology of early Neogene sands. Norsk Geologisk Tiddsskrift, 119-160.

Gregersen, U., 1998. Upper Cenozoic channels and fans on 3D seismic data in the northern Norwegian North Sea. Petroleum Geoscience 4, 67-80.

Gregersen, U., Johannessen, P.N., 2007. Distribution of the Neogene Utsira Sand and the succeeding deposits in the Viking Graben area, North Sea. Marine and Petroleum Geology 24, 591-606.

Haas, J.L., 1976. Physical properties of the coexisting phases and thermochemical properties of the H_2O component in boiling NaCl solutions. U.S. Department of the Interior, Geological Survey.

Hagen, S., 2012. Sleipner knowledge sharing in CCS projects. Statoil.

Harvey, A.H., 1996. Semiempirical correlation for Henry's constants over large temperature ranges. AIChE Journal 42, 1491-1494.

Haukaas, J., Nickel, M., Sonneland, L., 2013. Successful 4D history matching of the Sleipner CO2 plume, 75th EAGE Conference & Exhibition London, UK.

Herning, F., Zipperer, L., 1936. Beitrag zur berechnung der zahigkeit technischer gasgemische aus den zahigkeitswerten der einzelbestandteile. Das Gas und Wasserfach 5, 69-73.

Hill, M.C., Tiedeman, C.R., 2007. Effective groundwater model calibration with analysis of data, sensitivities, predictions, and uncertainty. John Wiley & Sons, Inc., Hoboken, New Jersey.

IPCC, 2005. IPCC special report on carbon dioxide capture and storage. Intergovernmental Panel on Climate Change p. 431.

Ji, X.Y., Adidharma, H., 2010. Thermodynamic modeling of CO2 solubility in ionic liquid with heterosegmented statistical associating fluid theory. . Fluid Phase Equilibria.293, 141-150.

Johnson, J.W., Nitao, J.J., Knauss, K.G., 2004. Reactive transport modelling of CO_2 storage in saline aquifers to elucidate fundamental processes, trapping mechanisms and sequestration partitioning. Geological Society, London, Special Publications 233, 107-128.

Jossi, J.A., Stiel, L.I., Thodos, G., 1962. The viscosity of pure substances in the dense gaseous and liquid phases. AIChE Journal 8, 59-63.

Kestin, J., Khalifa, H.E., Correia, R.J., 1981. Tables of the dynamic and kinematic viscosity of aqueous NaCl solutions in the temperature range 20-150°C and pressure range 0.1−35 MPa. Journal of Physical and Chemical Reference Data 10, 71-87.

Kumar, A., Noh, M., Pope, G.A., Sepehrnoori, K., Bryant, S., Lake, L.W., 2004. Reservoir simulation of CO_2 storage in deep saline aquifers 2004 SPE/DOE Symposium on Improved Oil Recovery, Tulsa, Oklahoma.

Law, A.M., Kelton, W.D., 2000. Simulation modeling and analysis, 3rd ed. McGraw-Hill, New York.

Lumley, D., 2009. 4D Seismic Monitoring of CO2: Practical Considerations, AAPG/SEG/SPE HEDBERG CONFERENCE “GEOLOGICAL CARBON SEQUESTRATION: PREDICTION AND VERIFICATION”, VANCOUVER, BC, CANADA, p. AAPG Search and Discovery Article #90103.

Nghiem, L., Sammon, P., Grabenstetter, J., Ohkuma, H., 2004. Modeling CO_2 storage in aquifers with a fully-coupled geochemical EOS compositional simulator 2004 SPE/DOE Symposium on Improved Oil Recovery, Tulsa, Oklahoma.

Nghiem, L., Yang, C., Shrivastava, V., Kohse, B., Hassam, M., Card, C., 2009. Risk mitigation through the optimization of residual gas and solubility trapping for CO2 storage in saline aquifers. Energy Procedia 1, 3015-3022.

Nilsen, H.M., Syversveen, A.R., Lie, K.-A., Tveranger, J., Nordbotten, J.M., 2012. Impact of top-surface morphology on CO_2 storage capacity. International Journal of Greenhouse Gas Control 11, 221–235.

NRC, 2013. Induced seismicity potential in energy technologies. National Academies Press.

Palandri, J.L., Kharaka, Y.K., 2004. A compilation of rate parameters of water-mineral interaction kinetics for application to geochemical modeling., U.S.Geol. Surv. Open File Report 2004-1068, p. 66.

Parker, R.L., 1994. Geophysical Inverse Theory. Princeton University Press, Princeton, New Jersey.

Phillips, S.L., 1981. A technical databook for geothermal energy utilization, Lawrence Berkeley National Laboratory Report LBL-12810, Berkeley, CA.

Pruess, K., 2004. The TOUGH Codes--A Family of Simulation Tools for Multiphase Flow and Transport Processes in Permeable Media. Vadose Zone J 3, 738-746.

Pruess, K., 2005. ECO2N: A TOUGH2 fluid property module for mixtures of water, NaCl, and CO_2. Lawrence Berkeley National Laboratory Paper: LBNL-57592.

Pruess, K., Olderburg, C., Moridis, G., 2012. TOUGH2 user's guide, version 2.0. Lawrence Berkeley National Laboratory Paper LBNL-43134.

Singh, V., Cavanagh, A., Hansen, H., Nazarian, B., Iding, M., Ringrose, P., 2010. Reservoir modeling of CO_2 plume behavior calibrated against monitoring data from Sleipner, Norway, SPE Annual Technical Conference and Exhibition, Florence, Italy.

Tan, S.P., Ji, X.Y., Adidharma, H., Radosz, M., 2006. Statistical associating fluid theory coupled with restrictive primitive model extended to bivalent ions. SAFT2: 1. Single salt plus water solutions. . Journal of Physical Chemistry B 110, 16694-16699.

Whitson, C.H., Michael, R.B., 2000. Phase behavior. Society of Petroleum Engineers.

Xu, T., Apps, J.A., Pruess, K., Yamamoto, H., 2007. Numerical modeling of injection and mineral trapping of CO_2 with H_2S and SO_2 in a sandstone formation. Chemical Geology 242, 319-346.

Yoon, P., Thodos, G., 1970. Viscosity of nonpolar gaseous mixtures at normal pressures. AIChE J. 16, 300-304.

Zhang, Y., Sahinidis, N.V., 2013. Uncertainty quantification in CO_2 sequestration using surrogate models from polynomial chaos expansion. Industrial & Engineering Chemistry Research 52, 3121-3132.

Zweigel, P., Arts, R., Lothe, A.E., Lindeberg, E.B.G., 2004. Reservoir geology of the Utsira Formation at the first industrial-scale underground CO_2 storage site (Sleipner area, North Sea). Geological Society, London, Special Publications 233, 165-180.

Zweigel, P., Heill, L.K., 2003. Studies on the likelihood for caprock fracturing in the Sleipner CO2 injection case – A contribution to the Saline Aquifer CO2 Storage (SACS) project. . SINTEF Petroleum Research.

Part II. Develop Reactive Transport Model with Rigorous Chemical Kinetics

1. Introduction

Previous reactive transport models (RTM) have provided significant insights towards understanding the process of carbon storage and predicting the fate of injected CO_2 (Balashov et al., 2013; Gaus et al., 2005; Liu et al., 2011; Mohd Amin et al., 2014). Almost all previous modelers, however, acknowledge that reaction kinetics remain the most uncertain parameters. Not surprisingly, the calculated results from various authors differ dramatically. Some authors predict a significant reduction of porosity in shale (Johnson et al., 2004) while others predict only a slight initial reduction or an increase of porosity for the Sleipner project in Norway, (Audigane et al., 2007; Gaus et al., 2005). The root of these problems is partly related to the persistent two to five orders of magnitude discrepancy between laboratory-measured and field-derived feldspar dissolution rates (Blum and Stillings, 1995; Zhu, 2009; Zhu et al., 2004).

We focus on the mineral feldspars because feldspar is the most abundant mineral in the earth's crust, making up more than 51% of the crust's volume. Typically, sandstones and shale contain a high percentage of feldspar. For example, the Utsira formation has 10 – 15 % feldspars. Mt. Simon Sandstone, a potential target for carbon sequestration in the Midwest of the United States, contains about 20% feldspar (Liu et al., 2011). Eau Claire Shale, Mt. Simon Sandstone's caprock, contains an average of ~ 20 % feldspar. Although feldspar dissolution rates are usually slow (in the order of 10^{-8} to 10^{-12} mol/m^2/s) in the temperature range of geological carbon sequestration (Blum and Stillings, 1995), the extent of water-feldspar reaction is significant because of the long time scale of CO_2 storage (10,000 years or longer) and the corrosive nature of the acid brine due to CO_2 invasion. Feldspar dissolution can also consume H^+, which promotes the precipitation of carbonate minerals and enhances the safety of CO_2 sequestration.

Advances in reaction kinetics research have narrowed this gap between field and lab rates. The coupling of dissolution of feldspar and secondary mineral precipitation results in negative feedback and slows down further dissolution of feldspar (Maher et al., 2009; Zhu and Lu, 2009; Zhu et al., 2010). How these reactions are coupled depends on rate laws and surface areas (Zhu et al., 2010). These results suggest that it is likely that most previous RTM simulations of long-term CO_2 fate have over-predicted the extent of reactions (e.g., feldspar dissolution, clay precipitation, and carbonate mineralization) and have over-estimated the acid buffering and mineral trapping capacities, as well as porosity/permeability changes.

A number of experiments near equilibrium have shown that the traditional linear rate law (TST) deviates from the actual relationship between reaction rate and Gibbs free energy of the reaction (Alekseyev et al., 1997; Burch et al., 1993; Hellmann and Tisserand, 2006). Different rate laws have been proposed to resolve this deviation, such as Burch-type and Alekseyev-type nonlinear rate law for feldspar dissolution (Alekseyev et al., 1997; Burch et al., 1993), and Burton-Cabrera-Frank (BCF) rate law for secondary mineral precipitation (Burton et al., 1951; Saldi et al., 2009).

Studies on the effects of different rate laws on the CO_2 trapping processes in the saline aquifer are scarce. We first investigated a sandstone formation resembling the Mt. Simon saline reservoir, which contains abundant feldspar in order to compare with earlier results of Liu et al. (2011). Later in Part III, we simulate similar scenarios for Utsira. Four rate law scenarios were constructed for the RTM of CO_2 sequestration in order to explore whether uncertainties of the rate laws have a large effect on CO_2 sequestration, how these effects work, and what role the coupling between feldspar dissolution and secondary mineral precipitation plays in the effect.

2. Modeling approach

2.1. Conceptual model

A CO_2 injection well is assumed to penetrate fully the homogeneous and isotropic sandstone formation of 10 m thickness and at a depth of 2 km. Supercritical CO_2 is injected into the sandstone layer at a rate of 1 kg/s along with the co-injected brine (chemical composition is the same as initial formation water) at a rate of 0.5 kg/s for 100 consecutive years. If implemented on the scale of representative thickness of 516 m, this modeled injection rate could be scaled up to millions of tons of CO_2 per year. Brine co-injection with CO_2 is suggested to promote residual trapping and enhance dissolution of the CO_2 (Kumar et al., 2004; Leonenko et al., 2006). This might induce the “salting out” effect which is considered by the simulator below (Spycher and Pruess, 2005). After the 100 years co-injection period, the brine is injected alone at a rate of 0.5 kg/s without CO_2 until the end of simulation (10,000 years) to represent approximately the return to the regional groundwater flow post CO_2 injection.

2.2. Modeling code

The simulations in the present study are conducted with the computer code ToughReact with ECO2N module. ToughReact is a numerical simulation program for chemically reactive non-isothermal, density-dependent flows of multi-phase fluids in porous and fractured media (Xu et al., 2004). The code can handle variety of equilibrium chemical reactions, such as aqueous complexation, gas dissolution/exsolution, cation exchange. Mineral dissolution/precipitation can be subject to either local equilibrium or kinetic controls. For kinetic mineral reactions, ToughReact uses a rate expression from Lasaga et al. (1994), and the rate constant is dependent on temperature and a variety of different mechanisms (such as neutral, acid, base mechanisms). A specific fluid property module ECO2N has been designed for multiphase flow dynamics to simulate geologic sequestration of CO_2 in saline aquifers (Pruess and Karsten, 2005). ECO2N can simulate the fluid property (e.g., density, viscosity, and enthalpy) in the system H_2O-NaCl-CO_2, considering two fluid phases: a water-rich aqueous phase and a CO_2 rich gas phase.

2.3. Grid design and hydrogeologic parameters

A radially symmetric grid model is set up in this study. The layer thickness is 10 m and grid block sizes increase logarithmically from the wellbore at the origin to the outer boundary of the model, which is approximately 10,000 m.

A constant pressure of 200 bars (representing a reservoir depth ~ 2000 m) is assigned to the aquifer initially to ensure the supercritical CO_2 flow along the entire formation. Reservoir pressure is allowed to build up due to CO_2 injection. The aquifer temperature is 75 °C. Minor perturbation to the temperature may occur due to the injection (André et al., 2010), but this perturbation is not considered in the simulations. Hydrological properties of the formation are listed in **Table 1**.

The boundary condition applied to our simulations for solving the reactive transport equations is a Dirichlet condition boundary. This Dirichlet boundary is implemented by assigning a large (infinite) volume to the boundary grid block (Pruess et al., 2012). Consequently, any influence from the influx becomes negligible when compared to the large volume of the formation brine. The aqueous chemical composition of the boundary element, as well as its thermodynamic conditions, such as temperature and pressure, is therefore kept essentially unchanged from the original formation brine (Pruess et al., 2012). The sandstone layer is initially saturated with water ($S_w = 1$).

2.4. Mineral and formation water composition

Initial mineral composition is listed in **Table 2**. As the formation water contains small amount of S (**Table 3**), potential secondary sulfates such as anhydrite and alunite are included. Gypsum is excluded, because anhydrite is the thermodynamic stable phase at the formation temperature of 75 ^{o}C.

The chemical composition for the formation water (**Table 3**) is taken from Eliasson et al. (1998). Prior to simulating reactive transport, a batch kinetic modeling of water-rock interaction is performed with the rate laws and kinetic data in the Base Case (see below), to equilibrate approximately the measured aqueous chemical composition and the initial minerals. A nearly steady-state aqueous solution composition is obtained that is used as the initial brine conditions in the models.

Equilibrium constants for the aqueous species and minerals are obtained from the thermodynamic database of EQ3/6 V7.2b with several revisions, following Xu et al. (2007). Local equilibrium is assumed to be attained by all reactions among the aqueous species in our simulations. Only two mineral reactions, calcite and anhydrite, are governed by the local equilibrium due to their fast reaction rates.

2.5. Kinetics of mineral reactions

2.5.1. Rate law

Traditionally, kinetically controlled mineral dissolution and precipitation are described by a general form of rate law (Lasaga, 1998; Lasaga et al., 1994),

$$\frac{r}{S} = \pm k a^{i}_{H^{+}} \, (f \Delta G_{r}) \tag{1}$$

where, r denotes the dissolution/precipitation rate in mol/s/kgw, S is the reactive surface area per kg H_2O, k is temperature dependent rate constant (mol/m^2/s), $a^{i}_{H^{+}}$ is the activity of H^+ and i is the empirical reaction order accounting for catalysis by H^+ in solution. $f(\Delta G_r)$ is the rate dependence on Gibbs free energy of the reaction ΔG_r, the chemical driving force of the reaction.

Generally, reactive transport modeling simulations used the $f(\Delta G_r)$ based on the Transition State Theory (TST) for elementary reactions (Lasaga, 1981a; Lasaga, 1981b),

$$f(\Delta G) = 1 - \exp\left(\frac{\Delta G_r}{RT}\right) \tag{2}$$

A number of experiments near equilibrium, however, have shown that the actual relationship between r_j and ΔG_r deviates from this so-called linear rate law in Eqn. (2) (Alekseyev et al., 1997; Burch et al., 1993; Hellmann and Tisserand, 2006). For feldspar dissolution, for example, different non-linear rate laws were proposed. Burch et al. (1993) discovered that feldspar dissolution reactions follow the empirical parallel rate law in the form of

$$R = k_1\left[1 - \exp(-n g^{m1})\right] + k_2\left[1 - \exp(-g)\right]^{m2} \tag{3}$$

where k_1 and k_2 denote the rate constants in units of mol/m^2/s, $g = |\Delta G_r| / RT$, and n, m_1, and m_2 are empirical parameters fitted from experimental data (Zhu, 2009).

Alekseyev et al. (1997) introduced another non-linear rate law in the form of

$$f(\Delta G_r) = \left|1 - \left(\frac{Q}{K}\right)^{p}\right|^{q} \tag{4}$$

where Q is the activity quotient, K is the equilibrium constant, p and q are fitting parameters.

Another source of kinetic uncertainties is that previous reactive transport modeling work generally used the same rate expressions for both dissolution and precipitation, which may lead to large errors. For example, using the TST based rate law along with this assumption leads to high precipitation rates even at low supersaturation (Hellevang et al., 2011). Moreover, the first order dependence on saturation state used for dissolution does not fit with the second order dependence observed for precipitation (Saldi et al., 2009).

Alternatively, the Burton-Cabrera-Frank (BCF) theory for crystal growth (Burton et al., 1951) can be used for secondary mineral precipitation,

$$f(\Delta G) = \left(\exp\left(\frac{\Delta G_r}{RT} \right) - 1 \right)^2 \tag{5}$$

Saldi et al. (2009) found that this rate law satisfactorily describes the experimental data of magnesite precipitation. BCF-type rate law has successfully simulated secondary mineralization in feldspar hydrolysis experiments (Zhu et al., 2010).

To explore whether uncertainties of the rate laws have a large effect on CO_2 sequestration, how these effects work, and what role the coupling between feldspar dissolution and secondary mineral precipitation plays in the effect, we constructed four scenarios using different rate laws for mineral reactions.

3.6.1.1. Scenario 1: Base Case

TST rate law (**Eq. 2**) is used for both the mineral dissolution and precipitation reactions.

3.6.1.2. Scenario 2: Alex Case

The latest version of ToughReact does not allow to input two $f(\Delta G_r)$ terms for mineral dissolution rate laws. Thus, we test the Alekseyev et al. (1997) type rate law (**Eq.4**; called "Alex law" hereafter) for feldspar dissolution. In order to ensure that the effects of Alex law is closer to the Burch-type law, we conduct a non-linear fitting with an excel solver to determine the parameters of p and q in **equation 4** (**Fig. 1a**). The curve of Burch-type law is used as a fitting target. The parameters of m_1, n, m_2, and k_1/k_2 values are all from Hellmann and Tisserand (2006) and (k_1+k_2) is normalized to be 1. The fitting at 75 ^{o}C (reservoir temperature of Mt. Simon) yields a p and a q of 0.184 and 4.04, respectively. Note that in the Alex Case, only feldspar dissolution rate laws (oligoclase, K-feldspar and albite) are changed to Alex law; all others remain to be the same as the Base Case (including feldspar precipitation rate law).

3.6.1.3. Scenario 3: BCF Case

In this scenario, BCF-type rate law (**Eq. 5**) is used for all secondary mineral precipitation reactions and TST rate law for all mineral dissolution reactions.

3.6.1.4. Scenario 4: Alex+BCF Case

In this case, Alex law is used for feldspar dissolution and BCF-type law for secondary mineral precipitation; all others remain to be the same as the Base Case.

2.5.2. Kinetic parameters

To calculate the kinetic rate constant k in **Eq. 1**, not only the neutral pH mechanism, but also acid and base mechanisms should be taken into account. This is because dissolution and precipitation are often catalyzed by H^+ (acid mechanism) and OH^- (base mechanism). Therefore, a general form for k, including the three mechanisms, is (Palandri and Kharaka, 2004):

$$\begin{aligned} k = {} & k_{nu}^{25} \exp\left[\frac{-E_{nu}}{R}\left(\frac{1}{T}-\frac{1}{298.15}\right)\right] + k_{H}^{25} \exp\left[\frac{-E_{H}}{R}\left(\frac{1}{T}-\frac{1}{298.15}\right)\right] a_{H}^{n_H} \\ & + k_{OH}^{25} \exp\left[\frac{-E_{OH}}{R}\left(\frac{1}{T}-\frac{1}{298.15}\right)\right] a_{OH}^{n_{OH}} \end{aligned} \tag{6}$$

where subscripts nu, H, and OH indicate neutral, acid, and base mechanisms, respectively; k^{25} is the rate constant at 25 °C; E is the apparent activation energy; R is the universal gas constant; T is the absolute temperature; a is the activity of the aqueous species; and n is a power term.

For each mineral controlled by kinetics in our simulations, the acid or base mechanism is taken into consideration for mineral dissolution reactions only. Precipitation reactions only employ a neutral pH mechanism due to the lack of precipitation rate data at different pH for most minerals. Kinetic parameters employed here are similar to those used in Xu et al. (2007), which are listed in **Table 4**.

3. Results

3.1. Alex Case

3.1.1. Feldspar dissolution

Compared to Base Case, using Alex law for feldspar dissolution does not make significant changes for rates of oligoclase dissolution patterns (diagrams not shown). The initial abundance of oligoclase is low, only 0.5 %; and it almost completely dissolves at ~ year 1,000 in the acidic zones due to the influence of CO_2 injection and ~ year 2,000 in the zones without the effects of CO_2 in both Base and Alex Cases. Oligoclase is highly undersaturated in both Base and Alex cases (SI < -15; $\Delta G_r < 100$ kJ/mol) and the rate law dependence on ΔG_r is small as a result (**Fig. 1a**).

K-feldspar dissolution rates, however, decrease significantly using Alex law compared to Base Case (**Fig. 3a, b**), especially in the acidic regions caused by CO_2 injection (**Fig. 5a, b**). The dissolution rate of K-feldspar in Base Case reaches a maximum value of ~ 2.5×10^{-11} mol/kg H_2O/s at year 100 in the acidic region, while the maximum dissolution rate in Alex Case is only 3.3×10^{-12} mol/kg H_2O/s (**Fig. 3a, b**). The calculated $f(\Delta G_r)$ of K-feldspar in Base Case is much higher than in Alex Case. For example, the maximum $f(\Delta G_r)$ of K-feldspar in Base Case is ~ 0.5 at ~ 2500 m, while it is only ~ 0.08 in Alex Case (**Fig. 1b**). Because reactive surface areas of K-feldspar in both Base Case and Alex Case vary only in a narrow range (around 3.2 ± 0.2 m^2/kg H_2O) due to its high initial abundance (24%), the rate differences of K-feldspar dissolution are mainly determined by $f(\Delta G_r)$.

The solution is unsaturated with respect to albite during the simulation and no albite precipitation is observed. Thus, we exclude the discussion of albite precipitation in all four cases.

3.1.2. Secondary mineral precipitation

Illite and quartz are the dominant secondary aluminosilicate minerals in the simulation. The maximum changes of volume fraction for illite and quartz in Base Case are ~ 2 % and ~ 1 %, respectively **(Fig. 2a)**, but are only ~ 0.5 % and ~ 0.3 %, respectively, in Alex case **(Fig. 2b)**. The maximum precipitation rate of illite drops from ~3.2×10^{-11} mol/kg H_2O/s in the acid region at year 100 in Base Case to ~ 2.5×10^{-11} mol/kg H_2O/s in Alex Case (**Fig. 4a, b**). This dropping is approximately consistent with and likely to be mainly caused by the differences in the $f(\Delta G_r)$ of illite (the maximum $f(\Delta G_r)$ value of illite in Base Case is about 1.3 times higher than that in Alex Case). Similarly, the maximum quartz precipitation rate decreases from ~ 6×10^{-11} mol/kg H_2O/s in Base Case to ~ 4.5×10^{-11} mol/kg H_2O/s in Alex Case because less $SiO_{2(aq)}$ is released from K-feldspar dissolution in the Alex case.

3.1.3. pH

A low pH zone with pH ~ 4.5 is observed in Base Case in ca. 0-200 m at year 100, 1,500-2,500 m at year 1,000, 2,500-4,000 m at year 5000, and disappears afterwards (being buffered to a higher pH: ~ 5.5 at year 10,000). In the Alex Case, however, the same low pH zone persists after year 5,000 and migrates to 4,000-6,000 m at year 10,000 (**Fig. 5a, b**).

4.1.4. Carbonate minerals and the fate of the injected CO_2

Considering the use of the same precipitation rate laws for the carbonate mineral precipitation for both Base and Alex Cases, the abundance of carbonate minerals mainly reflects the neutralization capacity of feldspars on pH. Less calcite precipitation is observed in Alex Case (maximum VF 0.68%) than in Base Case (maximum VF 0.73%), especially in the 0-4000 radial distance. Amounts of magnesite precipitation are similar in both Alex and Base Cases.

In this paper, for accounting purposes, we combined structural and residual trapping into one trapping mechanism, i.e., hydrodynamic trapping. The percentage of different tapping mechanisms as a function of time is shown in **Fig. 6**. The mineral trapping is mainly contributed by calcite and magnesite precipitation, and its percentage reduces from ~ 45% in Base Case to only ~ 22% in Alex Case at year 10,000 (**Fig. 6e**).

3.2. BCF Case

Compared to Base Case, BCF Case does not make significant changes for the patterns of feldspar dissolutions, secondary mineral precipitations, pH, and the fate of injected CO_2 (**Fig. 2a, c; Fig. 3a, c; Fig. 4a, c; Fig. 5a, c; Fig. 6a, c**). Generally, the mineral fraction changes are slightly smaller in the BCF Case than in Base Case (**Fig. 2a, c)** and the percentage of mineral trapping is slightly lower in BCF Case than in Base Case (**Fig. 6a, c**). This indicates that secondary mineral precipitation rate law is not the dominant factor in determining the system behavior.

3.3. Alex+BCF Case

Comparing Alex+BCF Case with Alex Case, the patterns of feldspar dissolutions, dominant secondary precipitations, pH, and the fate of injected CO_2 do not change significantly (**Fig. 2 b, d; Fig. 3b, d; Fig. 4b, d; Fig. 5b, d; Fig. 6b, d**). In Alex+BCF Case, the maximum dissolution rate of K-feldspar is ~3×10^{-12} mol/kg H_2O/s in the acidic region; the maximum precipitation rate of illite and quartz are ~ 2.5×10^{-11} mol/kg H_2O/s and ~ 4.3×10^{-11} mol/kg H_2O/s, respectively; mineral trapping fraction at year 10,000 is ~ 22%. These values are almost the same as those in the Alex Case.

4. Discussion

4.1. Coupling between K-feldspar dissolution and illite/quartz precipitation

Coupled feldspar dissolution –secondary mineral precipitation has been studied in a series of experiments (Lu et al., 2015; Yang et al., 2014; Zhu and Lu, 2009; Zhu and Lu, 2013). This coupling is driven by common ion effects in the solution. For example, K-feldspar dissolution releases Al and Si into the solution and the same aqueous components are consumed by kaolinite precipitation. Since the secondary kaolinite precipitation is slow, high concentrations of Al and Si are accumulated into the solution due to fast K-feldspar dissolution. This accumulation inhibits K-feldspar dissolution and promotes kaolinite precipitation by raising their saturation states. Eventually, the releasing and consuming rates of Al and Si approach the balance and rate ratios of K-feldspar dissolution versus kaolinite precipitation approaches the stoichiometric ratio of the overall reaction. The system thus reaches a steady-state and K-feldspar dissolution and kaolinite precipitation are coupled.

Because K-feldspar and illite are the most abundant primary and secondary aluminosilicate minerals, respectively, the coupling reaction between K-feldspar and illite is the dominant reaction during the simulation time (**Fig. 2a, Eq. 7**). Concurrent dissolution of K-feldspar and illitization plays the primary role in the generation of illite (Thyne et al., 2001). The intimate association of illite with K-feldspar is often observed in nature (Meunier and Velde, 2004). The overall reaction of K-feldspar dissolution and illite/quartz precipitation can be written as:

$$2.3\text{ K-feldspar} + 0.25\text{ Mg}^{+2} + 1.2\text{ H}^{+} + 0.4\text{H}_2\text{O} = \text{Illite} + 3.4\text{ Quratz} + 1.7\text{ K}^{+} \qquad (7)$$

Dissolution of K-feldspar will consume H^+ and release Al and Si, and thus alter the saturation states of illite and quartz. Proton consumption will affect the carbonate speciation and precipitation of carbonate minerals (**Eq. 8** and **9**):

$$CO_{2(g)} + H_2O = CO_{2(aq)};\ CO_{2(aq)} + H_2O = HCO_3^- + H^+ \qquad (8)$$

$$Mg^{+2} + HCO_3^- = \text{Magnesite} + H^+;\ Ca^{+2} + HCO_3^- = \text{Calcite} + H^+ \qquad (9)$$

Hence, the coupling between K-feldspar and illite dominates long-term mineral trapping. Note, the stoichiometric ratio of K-feldspar to illite is 2.3 and K-feldspar to quartz is 0.67. We will discuss below how rate laws affect the evolution of the coupling and safety of CO_2 sequestration.

4.1.1. Evolution of the coupling

Fig. 7 shows that the coupling of K-feldspar with illite/quartz can be divided into two stages: loose and tight coupling stages. In the first stage (loose coupling), the coupling of K-feldspar with illite/quartz has not been established and the reaction rate ratios K-feldspar dissolution versus illite/quartz precipitation are far from the corresponding stoichiometry in the overall reaction (**Eq. 7**). **Fig. 7** shows that the loose coupling stage exists for ~1000 years in Base Case and in BCF Case, and for ~2000 years in Alex and Alex+BCF Cases. Oligoclase dissolution is an important factor causing the rate ratios to be deviated from stoichiometry, because its dissolution supplies extra Al and Si which inhibits K-feldspar dissolution and promotes illite/quartz precipitation. Therefore, in this stage the reaction system tends to approach a steady state where illite stoichiometric precipitation rates are roughly equal to the sum of stoichiometric rates of K-feldspar and oligoclase dissolution. Note that the coupled reaction ratios of K-feldspar/illite are closer to -2.3 in low pH zones at year 1,000 (**Fig. 8**) because oligoclase dissolution is accelerated in low pH environment and oligoclase is almost exhausted at this time. The system is thus dominantly controlled by the coupling of K-feldspar with illite/quartz.

In the “tight coupling stage”, the reaction rate ratio approximately stabilizes at the corresponding stoichiometry ratio in the overall reaction (**Eq. 7**) and the system reaches a second steady state. The overall reaction rates decreases slowly within a long time due to the mitigation effects of illite/quartz precipitation. For example, rates of K-feldspar dissolution drops from ~ 2.2×10^{-13} mol/kg H_2O/s at year 2000 to ~ 5.4×10^{-14} mol/kg H_2O/s at year 10,000 in the zones free of CO_2 influences in Alex Case. Tight coupling stage sustains for a much longer time; K-feldspar, illite/quartz reactions, and mineral trapping primarily occur in this stage (**Fig. 6**). K-feldspar dissolution is faster than it should be at the stoichiometric ratio of K-feldspar/illite in normal pH zones (~ 6.5), but K-feldspar/illite ratio is closer to -2.3 in the acidic zones (**Fig. 8**). This is because Clinochlore-14A precipitation consumes Mg, Al and Si, and promotes extra K-feldspar dissolution in the normal pH zones, but in the acidic zones clinochlore-14A does not precipitate (**Fig. 9**).

4.1.2. Effect of rate law on the coupling and CO_2 sequestration safety

Because calcite is assumed to be at local equilibrium and the rate constant of magnesite is several orders of magnitude larger than K-feldspar, illite, and quartz (**Table 4**), change of rate law for secondary mineral precipitation does not make significant changes for the patterns of K-feldspar/illite rate ratios, pH and mineral trapping (**Figs. 5-8**). Therefore, we focus on comparing Alex Case with Base Case below.

The H^+ consumption is much less in Alex Case than in Base Case (**Eq. 7**) because Alex law decreases the maximum K-feldspar dissolution rate and thus the overall reaction rates of K-feldspar and illite/quartz. Solution pH, therefore, rises more quickly in Base Case than in Alex Case. Larger amount of carbon is trapped into the mineral phase in Base Case than in Alex Case (**Fig. 6**) as higher pH promotes faster precipitation of calcite and magnesite (**Eq. 9**). These indicate that using TST rate law for feldspar dissolution may overestimate mineral trapping.

4.2. Comparison with previous work

Zhu et al. (2010) simulated the feldspar hydrolysis experiments with reaction path model to explores how feldspar dissolution and secondary precipitations are coupled in batch reactor experimental systems. One set of experiment data is from Alekseyev et al. (1997), who conducted batch experiments for albite dissolution in 0.1 m $KHCO_3$ fluid at 300 °C, 88 bars, and pH ~ 9.0 (buffered by bicarbonate). The measured initial Brunauer–Emmett–Teller specific surface areas were 0.12 m^2/g for albite, and XRD and SEM results show that sanidine was the only secondary mineral. Zhu et al. (2010) found that (1) the preliminary stage (loose coupling) before tight coupling between albite and sanidine is relatively shorter (<672 h) when compared to the time needed for the complete dissolution of albite (3650 h). The tight coupling stage will be even longer if more albite is present; (2) with the sigmoidal shape rate law for primary mineral dissolution (the Burch type law), the influence of the ΔG_r term takes effect earlier and the rates drop faster than TST rate law in the course of approaching equilibrium; (3) The precipitation of the secondary minerals is the liming step which controls the dissolution rate of the primary mineral.

Although the system (minerals, aqueous solution and CO_2) is much more complex in our current simulation work than that in Zhu et al. (2010) and it is a flow instead of a static system, the conclusions drawn from Zhu et al. (2010) remain valid. We find that (1) the loose coupling stage is much shorter than the tight coupling stage; (2) the influence of the ΔG_r term for K-feldspar takes effect at a lower ΔG_r value away from the equilibrium, if using Alex law for feldspar dissolution instead of TST law; (3) illite/quartz precipitation is the rate controller for the overall reaction.

The major differences between the two studies are (1) the coupling of K-feldspar dissolution and illite/quartz is disturbed due to oligoclase dissolution and Clinochlore-14A precipitation; (2) ΔG_r for K-feldspar increases from -8.3 kJ/mol at year 2000 to -2.5 kJ/mol at year 10,000 (**Fig. 1b**), rather than locked at a fixed value, as in Zhu et al. (2010).

Pham et al. (2011) investigated how the rate model (BCF+CNT model; CNT: classical nucleation theory) that takes into account both nucleation and growth of secondary mineral phases influences CO_2 portion trapped in mineral in a batch system for Utsira-type reservoirs. Their results suggest that using TST instead of BCF+CNT law for mineral precipitation largely overestimated the growth potential of carbonates such as dawsonite, magnesite, and dolomite. In contrast, our simulation shows that using TST instead of BCF precipitation law does not make significant changes for the percentage of mineral trapping. The main reason for this discrepancy is that BCF+CNT law considers nucleation processes and secondary minerals need to overcome a certain threshold SI in order to precipitate, which significantly influences the paragenetic sequence and results in a large difference in mineral trapping.

Balashov et al. (2013) investigated the fate of injected CO_2 with a reactive diffusion model that was solved by program MK76. They observed coupling among primary and secondary minerals when analyzing the impact of kinetic rate constants on stored CO_2. For example, when the rate constant of oligoclase increases, the maximum volume fractions of both smectite and albite rise correspondently. However, they did not investigate further how the minerals interact with each other, the mathematics and chemistry behind the coupling, and how the coupling affects the fate of injected CO_2. In this paper we studied the mechanism of coupled reactions and how the coupling evolves, and discovered that the coupling of K-feldspar with illite/quartz is the dominant process controlling the long-term mineral trapping.

To date, only a few studies have focused on the effect of rate laws on CO_2 trapping in the deep saline aquifer. In this paper, we investigated a sandstone formation resembling the Mt. Simon saline aquafer in the Midwest, United States which has abundant feldspar. However, systems with different initial sandstone compositions, water chemistry and reservoir conditions may have different types of mineral coupling and the role of rate laws may also vary case by case. The rate laws considered here are only TST, Alex and BCF laws. Pham et al. (2011) suggested the nucleation process significantly influences the paragenetic sequence of secondary mineralization, resulting in a larger difference in mineral trapping. Additionally, Burch type law (Burch et al., 1993) is better to delineate the evolution of feldspar dissolution rates near equilibrium. Therefore, further work is still needed to explore how the factors listed above affect the effect of rate law on CO_2 sequestration.

5. Conclusions and Remarks

We conducted a reactive transport model for CO_2 sequestration in a sandstone formation resembling the Mt. Simon saline reservoir. Four rate law scenarios were constructed to investigate whether rate law uncertainties have large effect on CO_2 sequestration, how these effects work, and what role the coupling between feldspar dissolution and secondary mineral precipitation plays in the effect. Our conclusions are presented below:

(1) The coupled K-feldspar dissolution with illite/quartz precipitation is the dominant reaction because of the high initial K-feldspar abundance (24%) and illite/quartz to be the most abundant secondary aluminosilicate minerals. Therefore, H^+ consumption is primarily dominated by this coupling, which increases pH and HCO_3^- concentration in the solution, and promotes precipitation of carbonate minerals.

(2) Mineral trapping is more sensitive to the rate laws on feldspar dissolution than to rate laws on carbonate mineral precipitation. This is because carbonate mineral precipitation rates are fast compared to feldspar dissolution and silicate secondary mineral precipitation. In the network of reactions, the slowest reactions dominate the whole process.

(3) Negligence of the sigmoidal shape of rate – ΔG_r relationships and the mitigating effects secondary mineral precipitation can overestimate both the extent of feldspar dissolution during CO_2 injection and the extent of mineral trapping.

Our present work focuses on the Mt. Simon sandstone type reservoir and a limited number of rate laws (TST, BCF, Alex laws). Further work is still needed to explore how initial sandstone compositions, water chemistry, and reservoir conditions affect the effect of rate law on CO_2 sequestration.

Part II Tables

Table 1. Hydrogeologic parameters for the Mt. Simon sandstone formation

Parameters	Adopted values	Range	References
Permeability (m^2)	10^{-13}		Liu et al. (2011)
Porosity	0.15		Liu et al. (2011)
Thickness (m)	500		Liu et al. (2011)
Temperature (^oC)	75	20-150	Eliasson et al. (1998); Hovorka et al. (2012); Leeper (2012)
Pressure (bar)	200	70 - 420	Eliasson et al. (1998); Hovorka et al. (2012)
CO_2 injection rate (kg/s)	1 (at 0-100 years)		
Co-injected brine rate (kg/s)	0.5		
Relative permeability			
Liquid (Van Genuchten, 1980):			
$k_{rl} = \sqrt{S^*\{1-(1-[S^*]^{1/m})^m\}^2}$	$S^*=(S_l-S_{lr})/(1-S_{lr})$		
S_{lr}: irreducible water saturation	0.3	0.22-0.46	Krevor et al. (2012)
m: exponent	0.58		
Gas (Corey, 1954):			
$k_{rg} = \left(1-\hat{S}\right)^2(1-\hat{S}^2)$	$\hat{S} = \frac{(S_l - S_{lr})}{(1-S_{lr}-S_{gr})}$		
S_{gr}: irreducible gas saturation	0.1	Maximum 0.21	Krevor et al. (2012)
Capillary pressure (Van Genuchten, 1980):			
$P_{cap} = -P_o\left([S^*]^{-1/m}-1\right)^{1-m}$	$S^*=(S_l-S_{lr})/(1-S_{lr})$		
S_{lr}: irreducible water saturation	0.3	0.22-0.46	Krevor et al. (2012)
m: exponent	0.45		
P_o: strength coefficient (kPa)	6.6		Krevor et al. (2012)

Table2. Initial mineral volume fractions and possible mineral phases used in the simulations

Minerals introduced in the model	Chemical formula	Volume percent (%)[1]
Quartz	SiO_2	69.95
K-feldspar	$KAlSi_3O_8$	24
Oligoclase	$Ca_{0.2}Na_{0.8}Al_{1.2}Si_{2.8}O_8$	0.5
Dolomite	$CaMg(CO_3)_2$	0.85
Illite	$K_{0.6}Mg_{0.25}Al_{1.8}(Al_{0.5}Si_{3.5}O_{10})(OH)_2$	4.7
Calcite	$CaCO_3$	
Anhydrite	$CaSO_4$	
Chlorite	$(Mg_{2.5}Fe_{2.5}Al)(AlSi_3)O_{10}(OH)_8$	
Low-albite	$NaAlSi_3O_8$	
Magnesite	$MgCO_3$	
Kaolinite	$Al_2Si_2O_5(OH)_4$	
Siderite	$FeCO_3$	
Ankerite	$CaMg_{0.3}Fe_{0.7}(CO3)_2$	
Dawsonite	$NaAlCO_3(OH)_2$	
Opal-A	SiO_2	
Alunite	$KAl_3(SO_4)_2(OH)_6$	
Na-smectite	$Na_{0.29}Mg_{0.26}Al_{1.77}Si_{3.97}O_{10}(OH)_2$	
Ca-smectite	$Ca_{0.145}Mg_{0.26}Al_{1.77}Si_{3.97}O_{10}(OH)_2$	
Clinochlore-14A	$Mg_5Al_2Si_3O_{10}(OH)_8$	

[1] Eliasson et al. (1998) and Leeper (2012)

Table 3. Solution chemistry of the Mt. Simon formation brine after Eliasson et al. (1998)

Component	Concentration
	(mol/kg H_2O)
Ca	3.547×10^{-1}
Mg	1.033×10^{-1}
Na	1.596
K	3.108×10^{-2}
Fe	3.161×10^{-5}
C	1.724×10^{-3}
S	1.408×10^{-2}
Cl	2.545
pH	6.9
Temperature	75 °C

Table 4. Adopted kinetic data for minerals*

Mineral	k_H (E_a) ($mol/m^2/s^1$) (kJ/mol)	k_{H2O} (E_a) ($mol/m^2/s^1$) (kJ/mol)	n	Specific surface area (cm^2/g)	Rate Law (Base Case)	Rate Law (Alex Case)	Rate Law (BCF Case)	Rate Law (Alex+BCF Case)
Quartz		1.023 x 10^{-14} (87.7)		9.8	TST	TST	Dissolution: TST; Precipitation BCF	Dissolution: TST; Precipitation BCF
K-feldspar	8.710 x 10^{-11} (51.7)	3.890 x 10^{-13} (38)	0.5	9.8	TST	Dissolution: Alex; Precipitation: TST	Dissolution: TST; Precipitation BCF	Dissolution: Alex; Precipitation BCF
Oligoclase	2.138 x 10^{-10} (65)	1.445 x 10^{-12} (69.8)	0.457	9.8	TST	Dissolution: Alex; Precipitation: TST	Dissolution: TST; Precipitation BCF	Dissolution: Alex; Precipitation BCF
Dolomite	6.457 x 10^{-4} (36.1)	2.951 x 10^{-8} (52.2)	0.5	9.8	TST	TST	Dissolution: TST; Precipitation BCF	Dissolution: TST; Precipitation BCF
Illite	1.047 x 10^{-11} (23.6)	1.660 x 10^{-13} (35)	0.34	151.63	TST	TST	Dissolution: TST; Precipitation BCF	Dissolution: TST; Precipitation BCF
Anhydrite					Equilibrium	Equilibrium	Equilibrium	Equilibrium
Calcite					Equilibrium	Equilibrium	Equilibrium	Equilibrium
Opal-a		Dissolution: 4.9 x 10^{-13} (76) Precipitation: 3.8 x 10^{-10} (49.8)		9.8	TST	TST	Dissolution: TST; Precipitation BCF	Dissolution: TST; Precipitation BCF
Chlorite		2.512 x 10^{-12} (62.76)		9.8	TST	TST	Dissolution: TST; Precipitation BCF	Dissolution: TST; Precipitation BCF
Low-albite	6.918 x 10^{-11} (65)	2.754 x 10^{-13} (69.8)	0.457	9.8	TST	Dissolution: Alex; Precipitation: TST	Dissolution: TST; Precipitation BCF	Dissolution: Alex; Precipitation BCF
Magnesite	4.619 x 10^{-7} (14.4)	4.517 x 10^{-10} (23.5)	1	9.8	TST	TST	Dissolution: TST; Precipitation BCF	Dissolution: TST; Precipitation BCF
Ankerite	6.457 x 10^{-4} (36.1)	1.260 x 10^{-9} (62.76)	0.5	9.8	TST	TST	Dissolution: TST; Precipitation BCF	Dissolution: TST; Precipitation BCF
Dawsonite	6.457 x 10^{-4} (36.1)	1.260 x 10^{-9} (62.76)	0.5	9.8	TST	TST	Dissolution: TST; Precipitation BCF	Dissolution: TST; Precipitation BCF
Siderite	6.457 x 10^{-4} (36.1)	1.260 x 10^{-9} (62.76)	0.5	9.8	TST	TST	Dissolution: TST; Precipitation BCF	Dissolution: TST; Precipitation BCF
Kaolinite	4.898 x 10^{-12} (65.9)	6.918 x 10^{-14} (22.2)	0.777	151.63	TST	TST	Dissolution: TST; Precipitation BCF	Dissolution: TST; Precipitation BCF
Alunite		1.000 x 10^{-12} (57.78)		9.8	TST	TST	Dissolution: TST; Precipitation BCF	Dissolution: TST; Precipitation BCF
Na-Smectite	1.047 x 10^{-11} (23.6)	1.660 x 10^{-13} (35)	0.34	151.63	TST	TST	Dissolution: TST; Precipitation BCF	Dissolution: TST; Precipitation BCF
Ca-Smectite	1.047 x 10^{-11} (23.6)	1.660 x 10^{-13} (35)	0.34	151.63	TST	TST	Dissolution: TST; Precipitation BCF	Dissolution: TST; Precipitation BCF
Clinochlore-14A	7.762 x 10^{-12} (88)	3.02 x 10^{-13} (88)	0.5	9.8	TST	TST	Dissolution: TST; Precipitation BCF	Dissolution: TST; Precipitation BCF

* Rate constants are at 25 °C.

Part II Figures

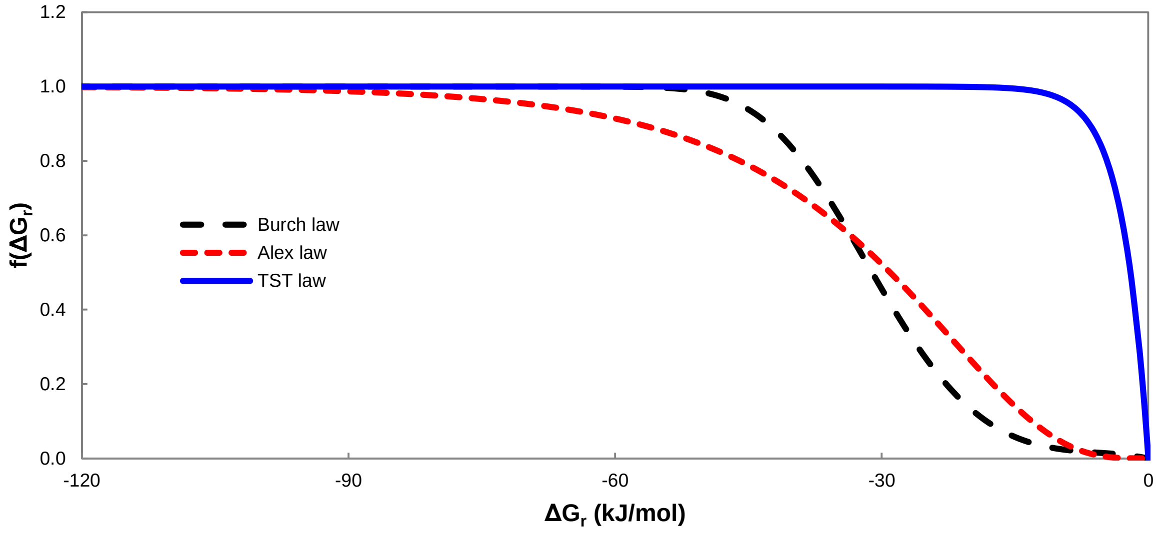

(a)

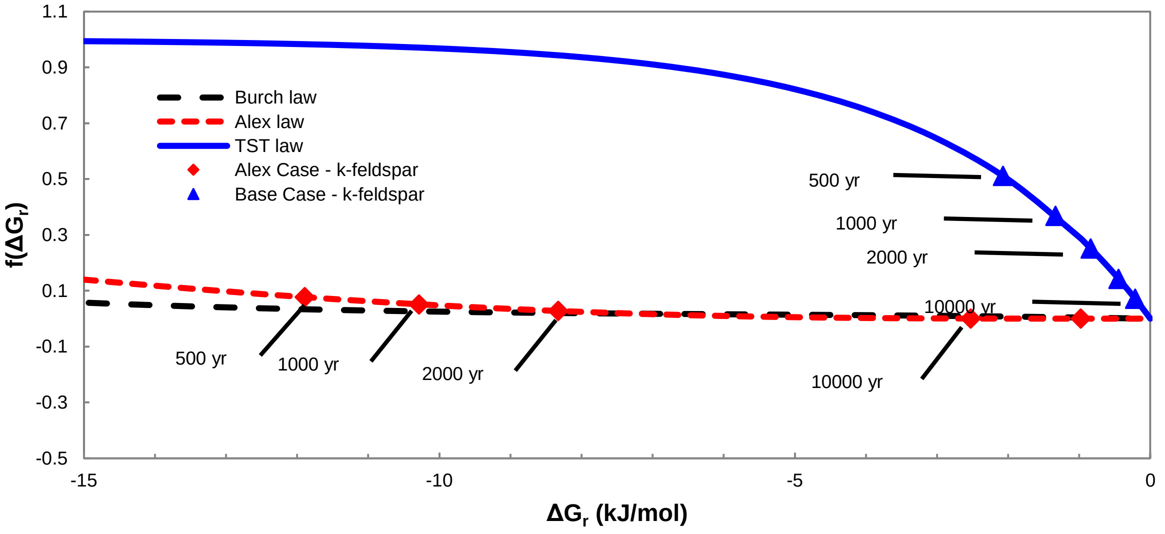

(b)

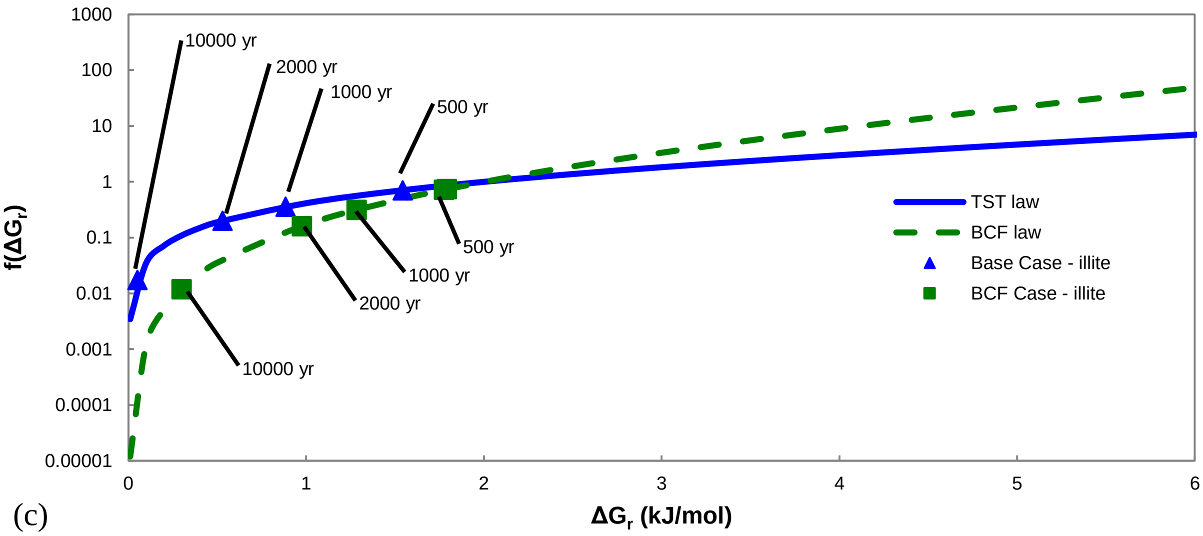

Fig. 1. Relationship between f(ΔG_r) and ΔG_r for different rate laws. Scatter points are the related data of K-feldspar or illite extracted from the corresponding cases at ~2500 m from year 500 to 10,000. (a) Comparison of feldspar dissolution rate laws. The curve of TST rate law differs significantly from Burch and Alex laws in the transition and near equilibrium regions. Alex law is used to represent Burch law, as a compromise of the code capability. (b) Zoom in of (a) in the near equilibrium region with data points extracted from the simulations. (c) Comparison of illite precipitation rate laws with data points extracted from the simulations.

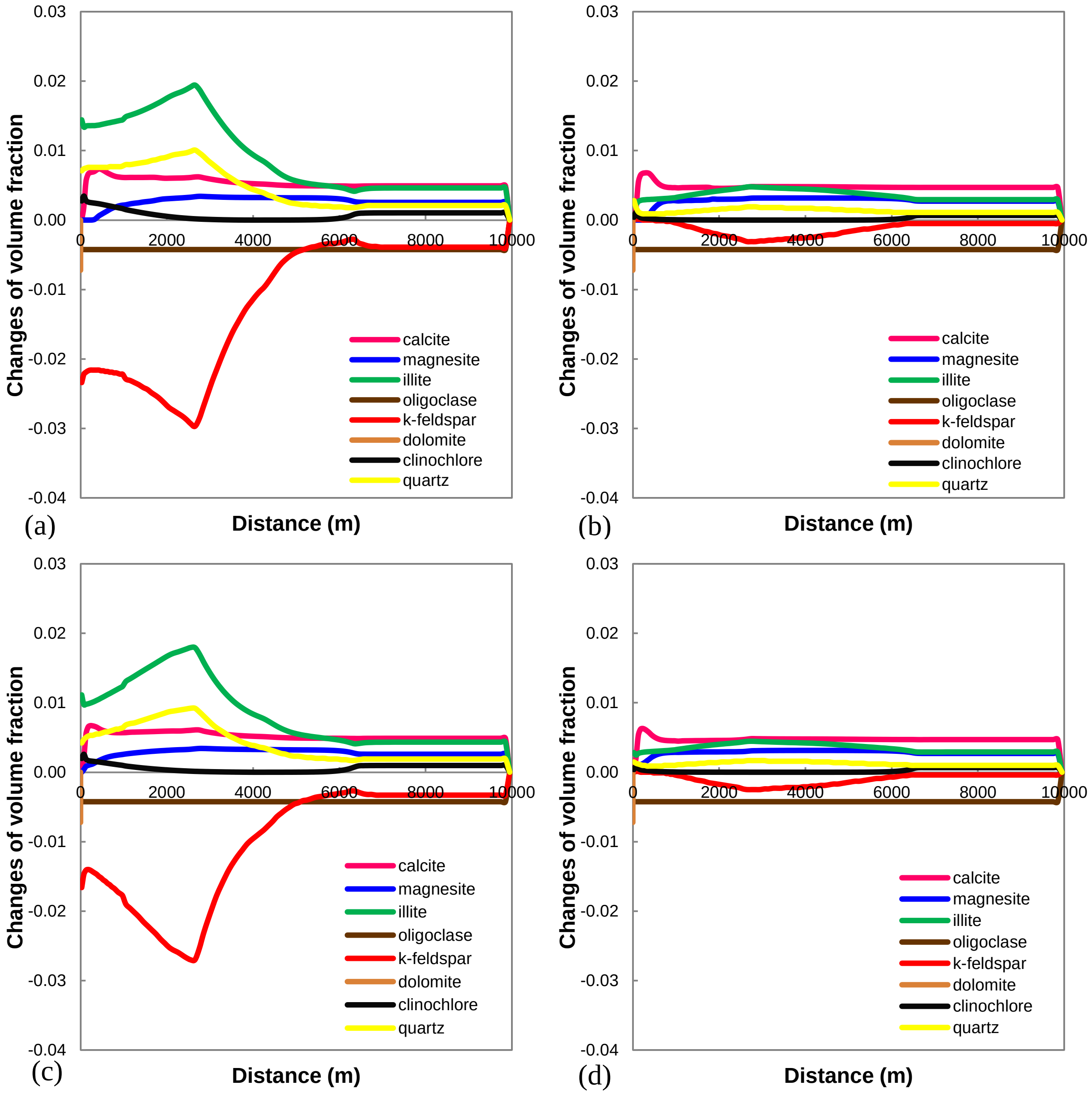

Fig. 2. Comparison of simulated results of mineral volume fraction changes, as function of radial distance at year 10,000. (a) Base Case with TST law for both feldspar dissolution and mineral precipitation; (b) Alex Case with Alex law for feldspar dissolution and TST law for mineral precipitation; (c) BCF Case with TST law for feldspar dissolution and BCF law for mineral precipitation; (d) Alex+BCF Case with Alex law for feldspar dissolution and BCF law for mineral precipitation.

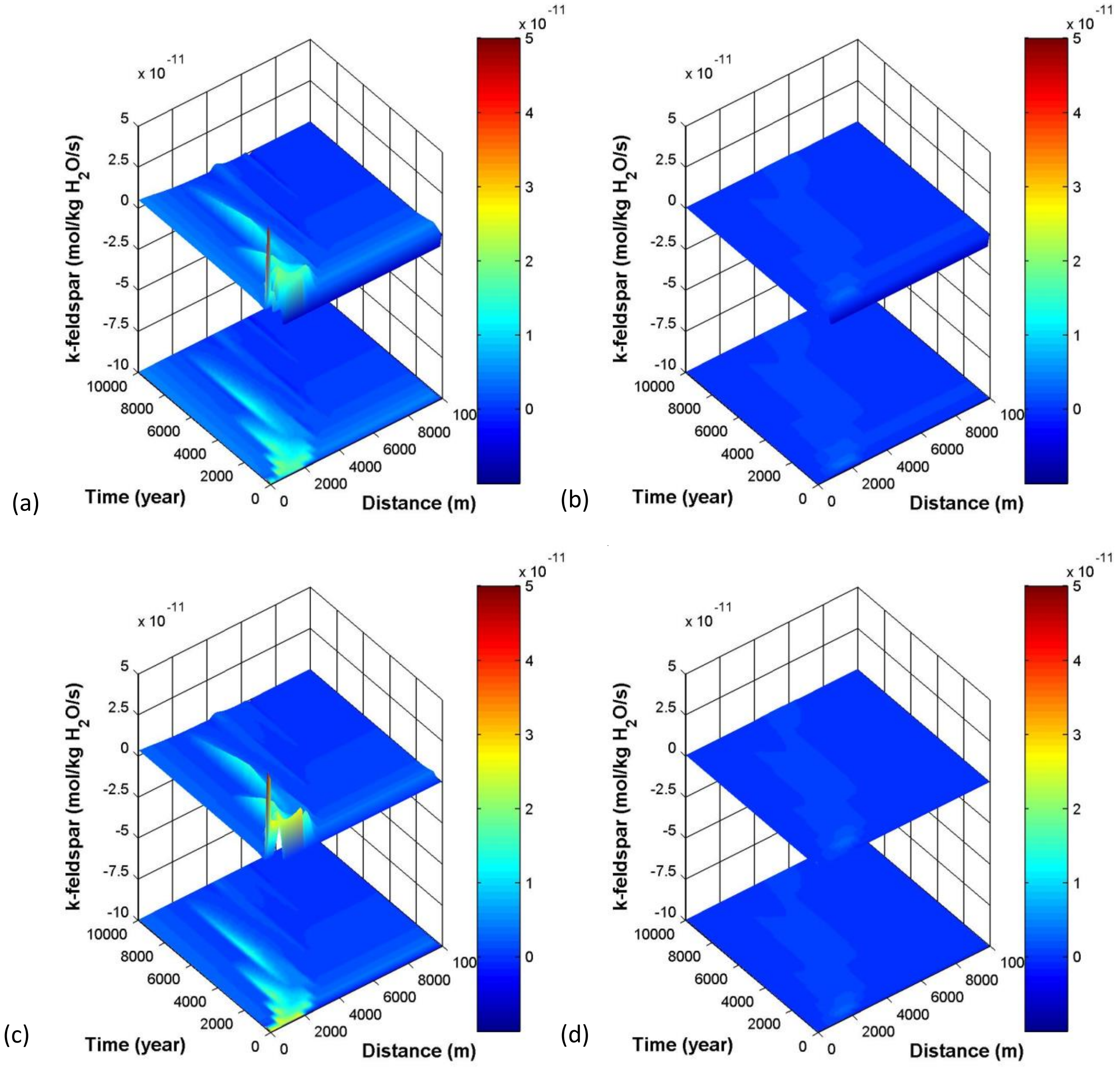

Fig. 3. Reaction rates of K-feldspar (mol/kg H_2O/s) as function of radial distance and time. (a) Base Case with TST law for both feldspar dissolution and mineral precipitation; (b) Alex Case with Alex law for feldspar dissolution and TST law for mineral precipitation; (c) BCF Case with TST law for feldspar dissolution and BCF law for mineral precipitation; (d) Alex+BCF Case with Alex law for feldspar dissolution and BCF law for mineral precipitation.

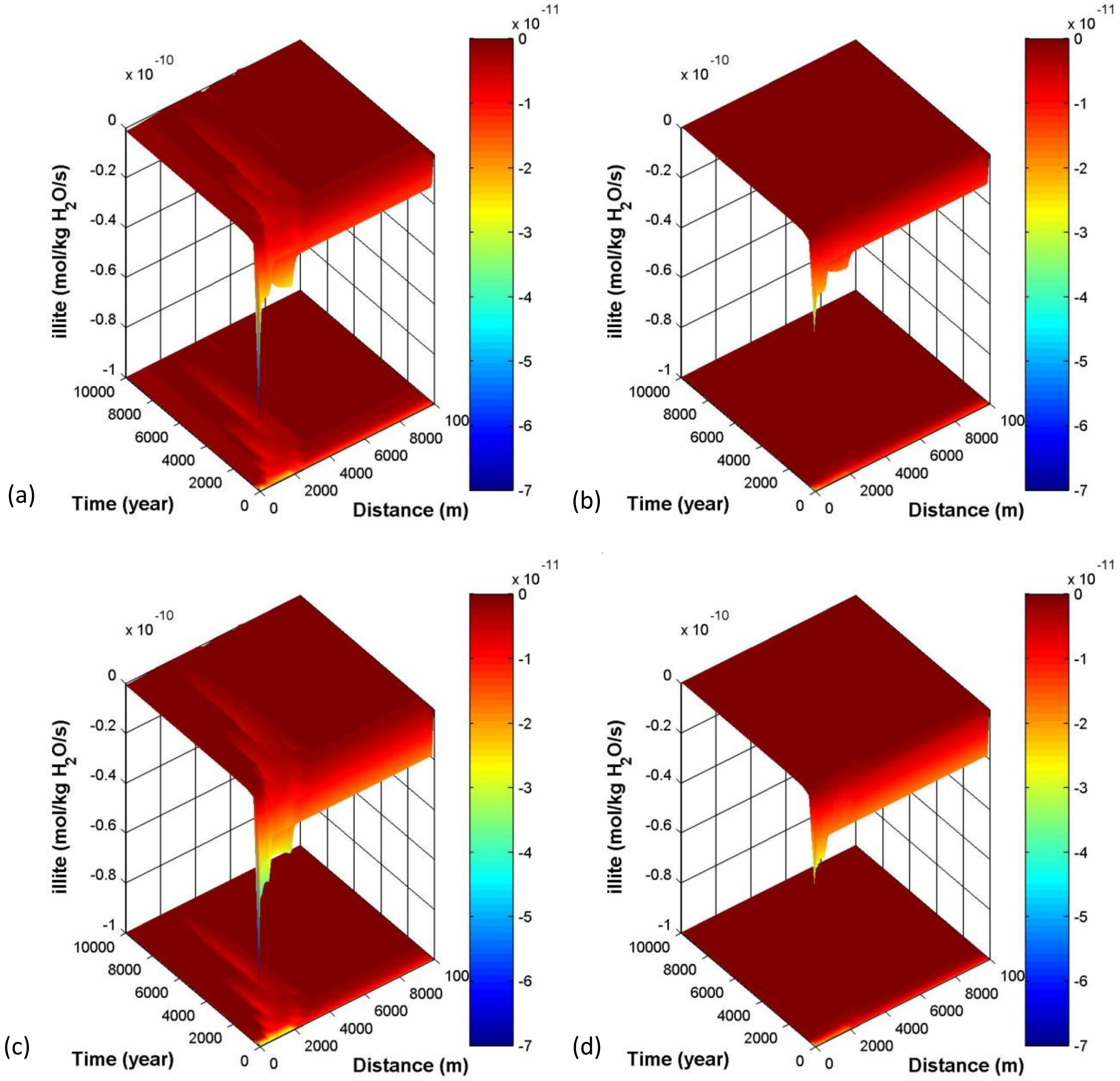

Fig. 4. Reaction rate of illite (mol/kg H_2O/s), as function of radial distance and time. (a) Base Case with TST law for both feldspar dissolution and mineral precipitation; (b) Alex Case with Alex law for feldspar dissolution and TST law for mineral precipitation; (c) BCF Case with TST law for feldspar dissolution and BCF law for mineral precipitation; (d) Alex+BCF Case with Alex law for feldspar dissolution and BCF law for mineral precipitation.

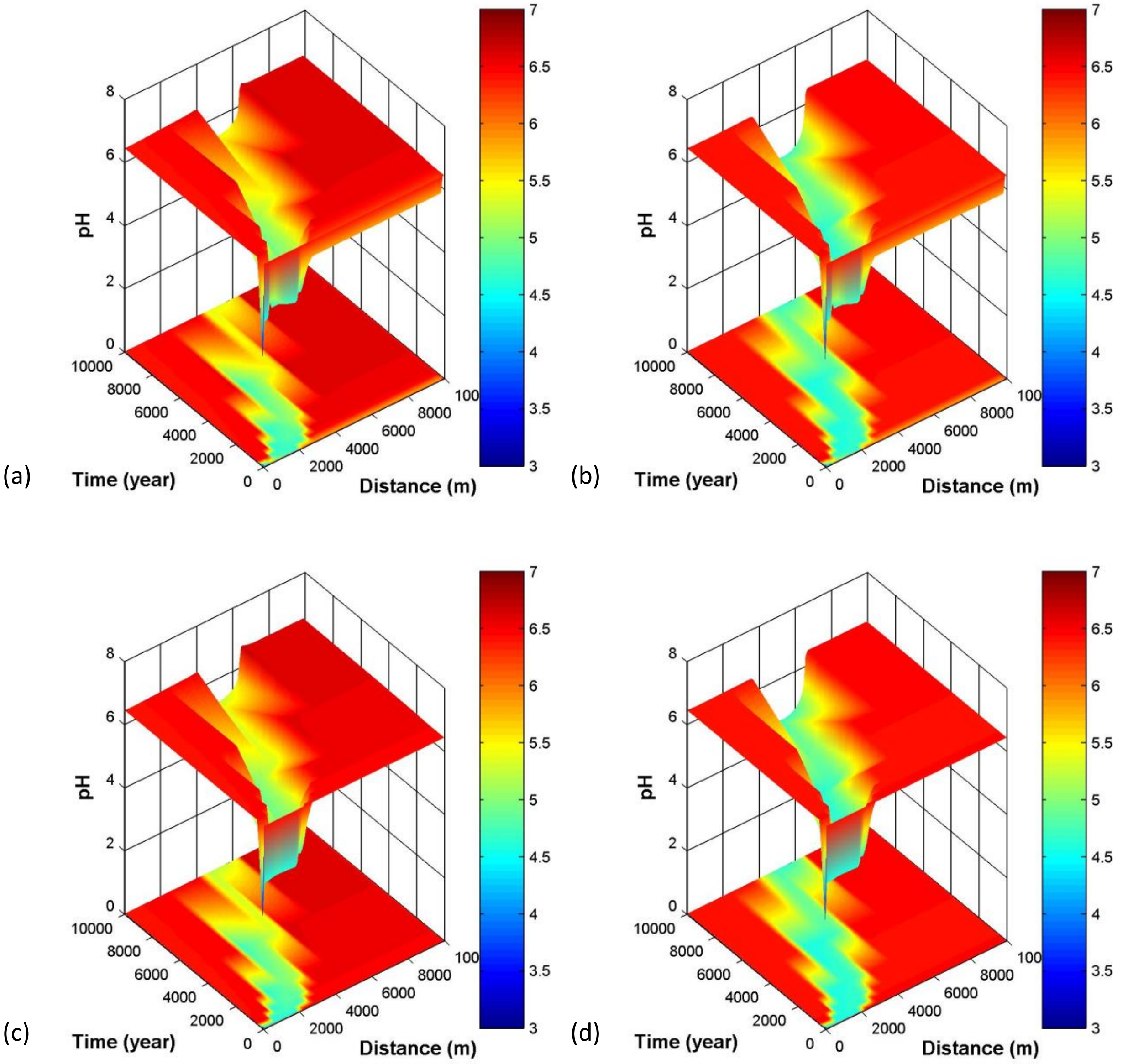

Fig. 5. pH as function of radial distance and time. (a) Base Case with TST law for both feldspar dissolution and mineral precipitation; (b) Alex Case with Alex law for feldspar dissolution and TST law for mineral precipitation; (c) BCF Case with TST law for feldspar dissolution and BCF law for mineral precipitation; (d) Alex+BCF Case with Alex law for feldspar dissolution and BCF law for mineral precipitation.

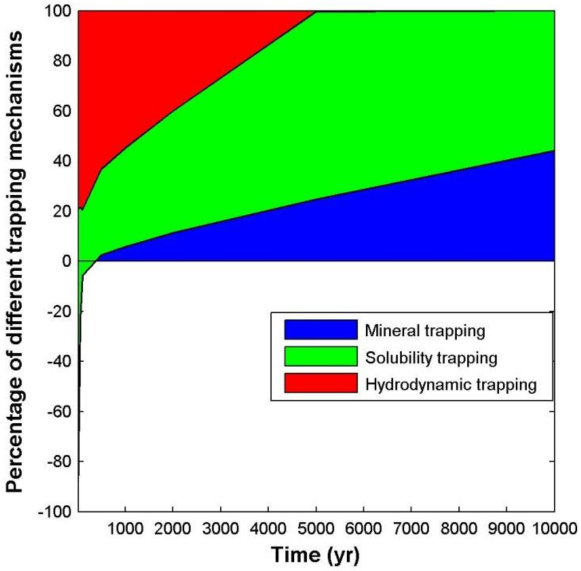
Percentage of different trapping mechanisms
100
80
60
40
20
0
-20
-40
-60
-80
-100
1000 2000 3000 4000 5000 6000 7000 8000 9000 10000
Time (yr)
Mineral trapping
Solubility trapping
Hydrodynamic trapping

(a)

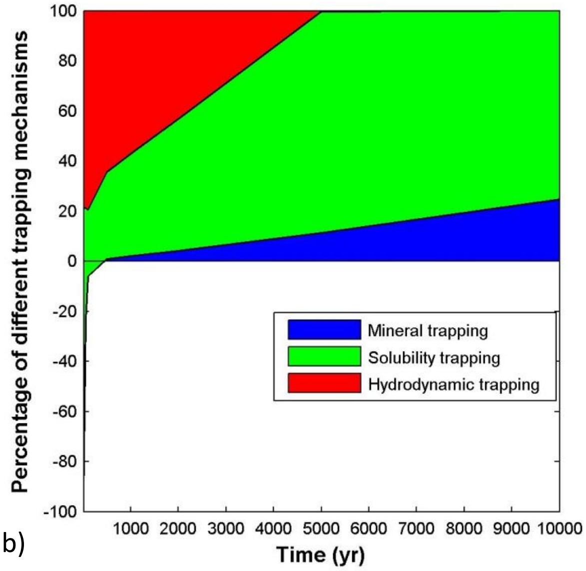
Percentage of different trapping mechanisms
100
80
60
40
20
0
-20
-40
-60
-80
-100
1000 2000 3000 4000 5000 6000 7000 8000 9000 10000
Time (yr)
Mineral trapping
Solubility trapping
Hydrodynamic trapping

(b)

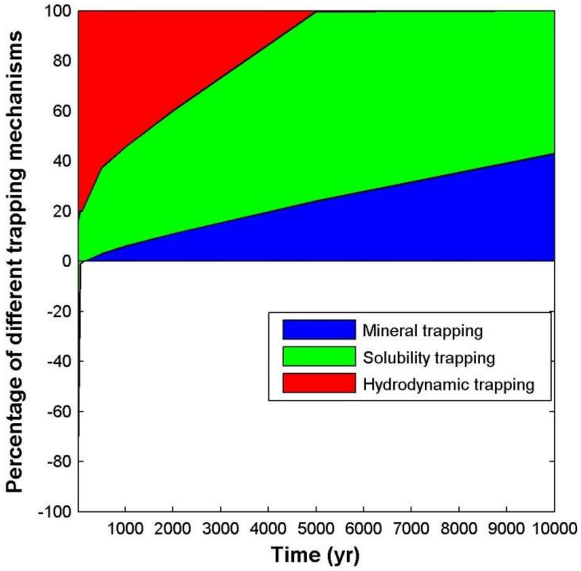
Percentage of different trapping mechanisms
100
80
60
40
20
0
-20
-40
-60
-80
-100
1000 2000 3000 4000 5000 6000 7000 8000 9000 10000
Time (yr)
Mineral trapping
Solubility trapping
Hydrodynamic trapping

(c)

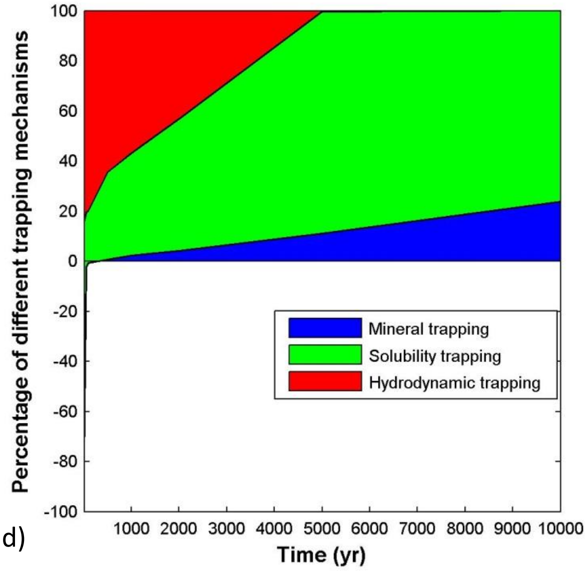
Percentage of different trapping mechanisms
100
80
60
40
20
0
-20
-40
-60
-80
-100
1000 2000 3000 4000 5000 6000 7000 8000 9000 10000
Time (yr)
Mineral trapping
Solubility trapping
Hydrodynamic trapping

(d)

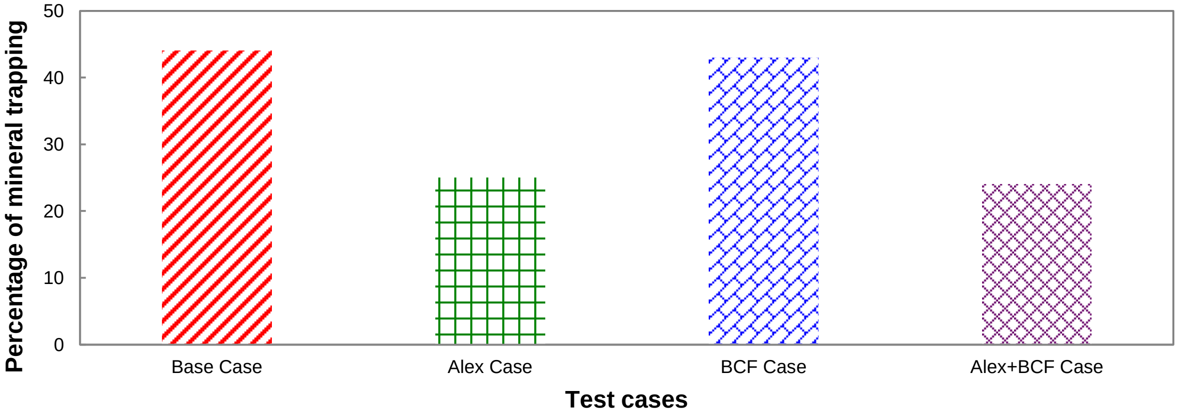
Percentage of mineral trapping
50
40
30
20
10
0
Base Case
Alex Case
BCF Case
Alex+BCF Case
Test cases

(e)

Fig. 6. Percentage of different trapping mechanisms for the whole domain as function of time. (a) Base Case with TST law for both feldspar dissolution and mineral precipitation; (b) Alex Case with Alex law for feldspar dissolution and TST law for mineral precipitation; (c) BCF Case with TST law for feldspar dissolution and BCF law for mineral precipitation; (d) Alex+BCF Case with Alex law for feldspar dissolution and BCF law for mineral precipitation. (e) Percentage of total injected CO_2 as mineral trapping after 10,000 years for the whole domain.

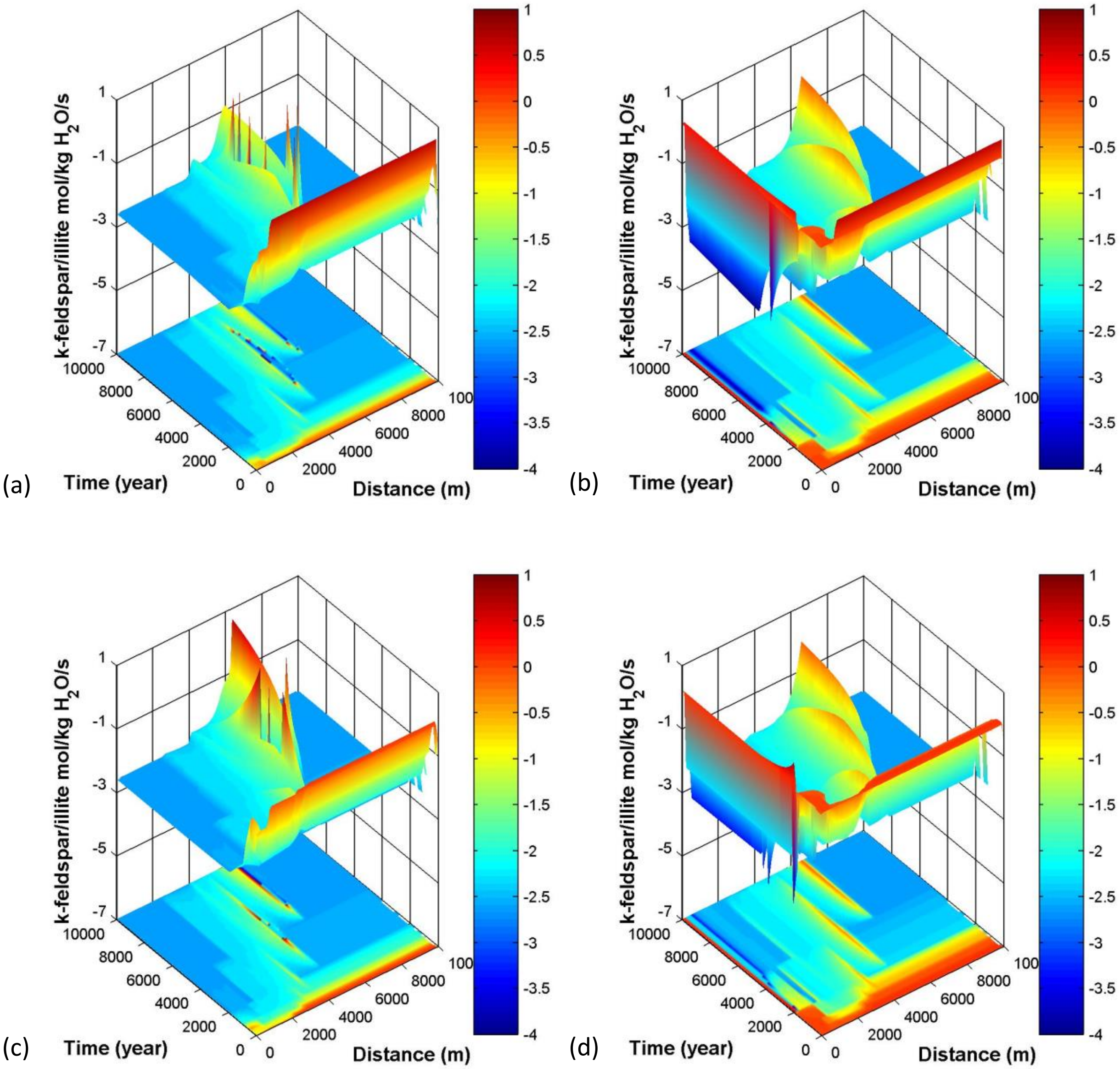

Fig. 7. Reaction rate ratios between K-feldspar and illite as function of radial distance and time. (a) Base Case with TST law for both feldspar dissolution and mineral precipitation; (b) Alex Case with Alex law for feldspar dissolution and TST law for mineral precipitation; (c) BCF Case with TST law for feldspar dissolution and BCF law for mineral precipitation; (d) Alex+BCF Case with Alex law for feldspar dissolution and BCF law for mineral precipitation.

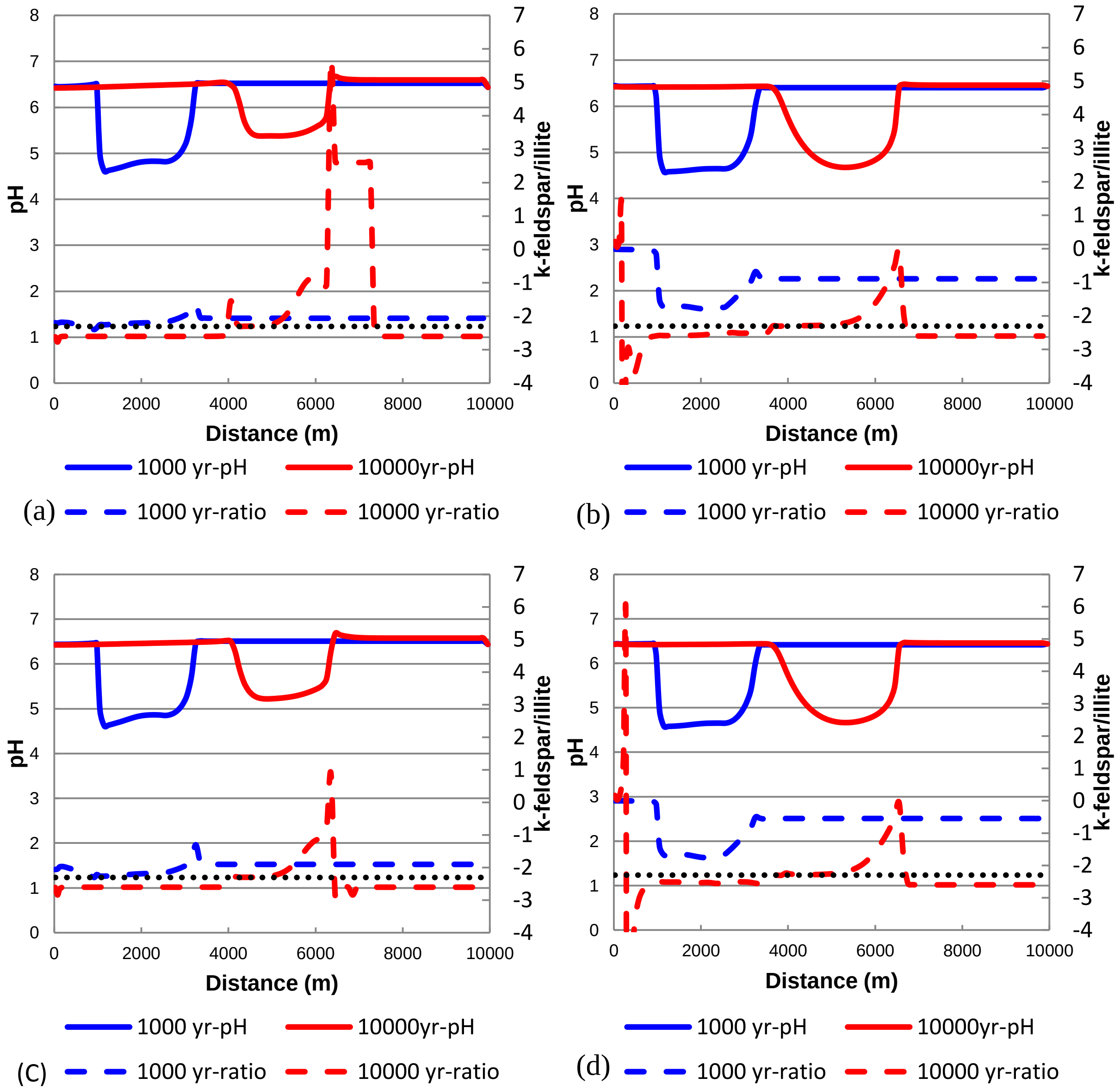

Fig. 8. Comparison of pH and the reaction rate ratios of K-feldspar versus illite, as function of radial distance at year 1000 and 10,000. (a) Base Case with TST law for both feldspar dissolution and mineral precipitation; (b) Alex Case with Alex law for feldspar dissolution and TST law for mineral precipitation; (c) BCF Case with TST law for feldspar dissolution and BCF law for mineral precipitation; (d) Alex+BCF Case with Alex law for feldspar dissolution and BCF law for mineral precipitation. The black dotted lines represent the stoichiometric ratio of K-feldspar/illite in the overall reaction (2.3).

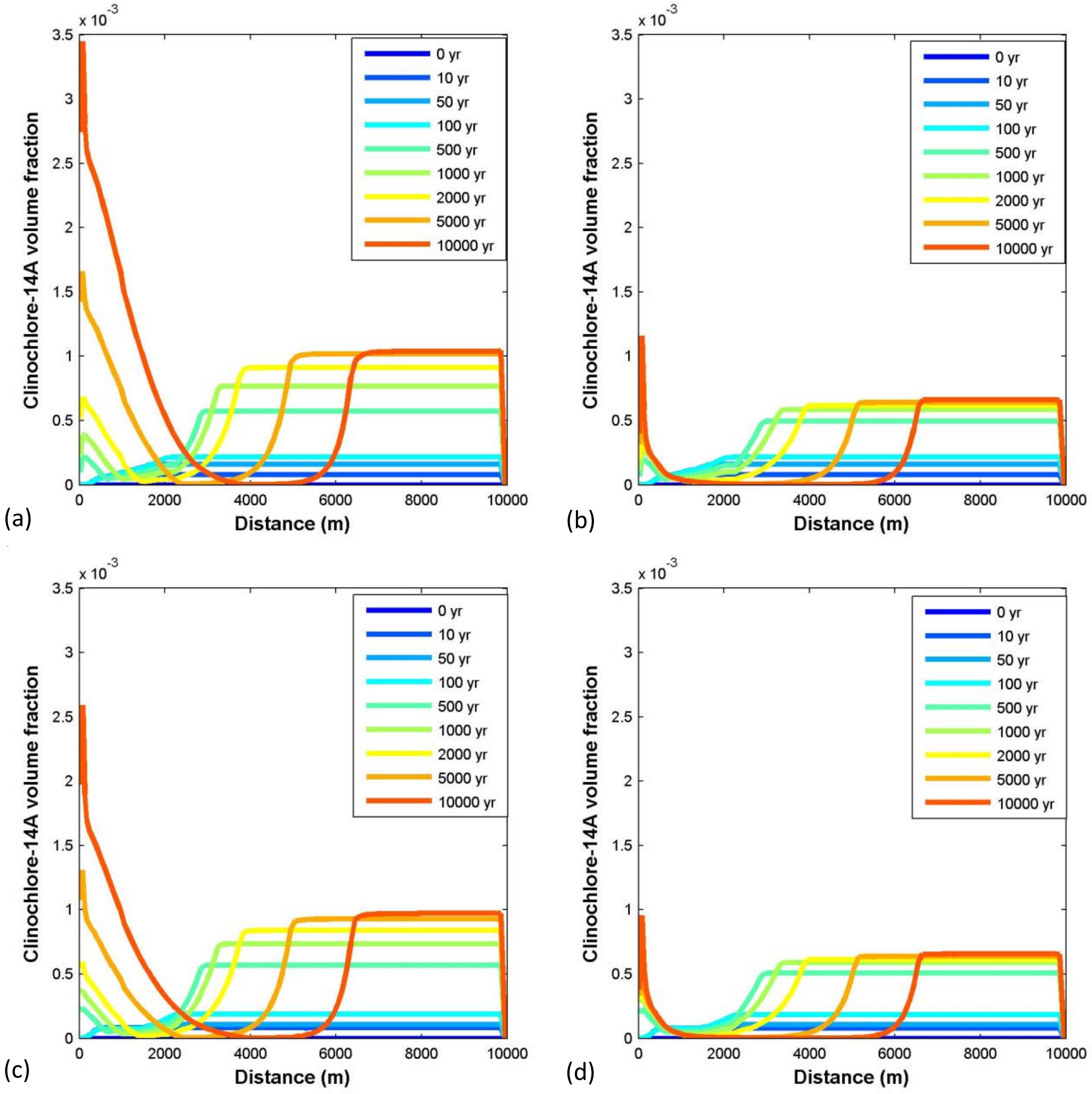

Fig. 9. Clinochlore-14A volume fraction as function of radial distance and time. (a) Base Case with TST law for both feldspar dissolution and mineral precipitation; (b) Alex Case with Alex law for feldspar dissolution and TST law for mineral precipitation; (c) BCF Case with TST law for feldspar dissolution and BCF law for mineral precipitation; (d) Alex+BCF Case with Alex law for feldspar dissolution and BCF law for mineral precipitation.

References

Alekseyev, V.A., Medvedeva, L.S., Prisyagina, N.I., Meshalkin, S.S., Balabin, A.I., 1997. Change in the dissolution rates of alkali feldspars as a result of secondary mineral precipitation and approach to equilibrium. Geochimica et Cosmochimica Acta 61, 1125-1142.

André, L., Azaroual, M., Menjoz, A., 2010. Numerical simulations of the thermal impact of supercritical CO_2 injection on chemical reactivity in a carbonate saline reservoir. Transport in Porous Media 82, 247-274.

Audigane, P., Gaus, I., Czernichowski-Lauriol, I., Pruess, K., Xu, T., 2007. Two-dimensional reactive transport modeling of CO_2 injection in a saline aquifer at the Sleipner site, North Sea. Am J Sci 307, 974-1008.

Bachu, S., Bonijoly, D., Bradshaw, J., Burruss, R., Holloway, S., Christensen, N.P., Mathiassen, O.M., 2007. CO_2 storage capacity estimation: Methodology and gaps. International Journal of Greenhouse Gas Control 1, 430-443.

Balashov, V.N., Guthrie, G.D., Hakala, J.A., Lopano, C.L., Rimstidt, J.D., Brantley, S.L., 2013. Predictive modeling of CO_2 sequestration in deep saline sandstone reservoirs: Impacts of geochemical kinetics. Applied Geochemistry 30, 41-56.

Becker, L.E., Hreha, A.J., Dawson, T.A., 1978. Pre-Knox (Cambrian) stratigraphy in Indiana. State of Indiana, Department of Natural Resources, Geological Survey.

Blum, A., Stillings, L., 1995. Feldspar dissolution kinetics, in: Brantley, S.L., White, A.R. (Eds.), Chemical Weathering Rates of Silicate Minerals. Mineralogical Society of America, Washington DC, pp. 291-346.

Bowersox, J.R., Williams, D.A., Greb, S., Nuttall, B.C., Parris, T.M., Anderson, W.A., 2008. Solving the carbon storage puzzle in Kentucky, North-Central Section-42nd Annual Meeting, Evansville, Indiana.

Burch, T.E., Nagy, K.L., Lasaga, A.C., 1993. Free energy dependence of albite dissolution kinetics at 80° C and pH 8.8. Chemical Geology 105, 137-162.

Burton, W.K., Cabrera, N., Frank, F.C., 1951. The growth of crystals and the equilibrium structure of their surfaces. Royal Soc. London Philos. Trans. 243, 299-358.

Cohee, G.V., 1948. Cambrian and Ordovician rocks in Michigan Basin and adjoining areas. AAPG Bull 32, 1417-1448.

Corey, A.T., 1954. The interrelation between gas and oil relative permeabilities. Prod. Mon., 38-41.

Desideri, U., Arcioni, L., Tozzi, M., 2008. Feasibility study for a carbon capture and storage project in northern Italy. International Journal of Energy Research 32, 1175-1183.

Eliasson, B., Riemer, P., Wokaun, A., 1998. Greenhouse gas control technologies: Proceedings of the 4th international conference on greenhouse gas control technologies. Elsevier.

Gaus, I., Azaroual, M., Czernichowski-Lauriol, I., 2005. Reactive transport modelling of the impact of CO_2 injection on the clayey cap rock at Sleipner (North Sea). Chemical Geology 217, 319-337.

Gunter, W.D., Bachu, S., Benson, S., 2004. The role of hydrogeological and geochemical trapping in sedimentary basins for secure geological storage of carbon dioxide. Geological Society, London, Special Publications 233, 129-145.

Hellevang, H., Declercq, J., Aagaard, P., 2011. Why is dawsonite absent in CO_2 charged reservoirs? Oil & Gas Science and Technology - Revue de l'IFP 66, 119-135.

Hellmann, R., Tisserand, D., 2006. Dissolution kinetics as a function of the Gibbs free energy of reaction: An experimental study based on albite feldspar. Geochim. Cosmochim. Acta 70, 364-383

Holloway, S., 2004. Underground sequestration of carbon dioxide--a viable greenhouse gas mitigation option. Energy 30, 2318-2333.

Hovorka, S.D., Romero, M.L., Warne, A.G., Ambrose, W.A., Tremblay, T.A., Treviño, R.H., Sasson, D., 2012. Sequestration of greenhouse gases in brine formations, Bureau of Economic Geology, The University of Texas at Austin.

IPCC, 2005. Special report on carbon dioxide capture and storage. Intergovernmental Panel on Climate Change

Johnson, J.W., Nitao, J.J., Knauss, K.G., 2004. Reactive transport modelling of CO_2 storage in saline aquifers to elucidate fundamental processes, trapping mechanisms and sequestration partitioning. Geological Society, London, Special Publications 233, 107-128.

Krevor, S.C.M., Pini, R., Zuo, L., Benson, S.M., 2012. Relative permeability and trapping of CO_2 and water in sandstone rocks at reservoir conditions. Water Resources Research 48, W02532.

Kumar, A., Noh, M., Pope, G.A., Sepehrnoori, K., Bryant, S., Lake, L.W., 2004. Reservoir simulation of CO_2 storage in deep saline aquifers, 2004 SPE/DOE Symposium on Improved Oil Recovery, Tulsa, Oklahoma.

Lasaga, A.C., 1981a. Rate laws of chemical reactions., in: Lasaga, A.C., Kirkpatrick, R.J. (Ed.), Kinetics of Geochemical Processes. Mineralogical Society of America, Washington DC, pp. 1-68.

Lasaga, A.C., 1981b. Transition state theory, in: Lasaga, A.C., Kirkpatrick, R.J. (Eds.), Kinetics of Geochemical Processes. Mineralogical Society of America, Washington DC, pp. 135-169.

Lasaga, A.C., 1998. Kinetic theory in the Earth sciences. Princeton University Press, New York.

Lasaga, A.C., Soler, J.M., Ganor, J., Burch, T.E., Nagy, K.L., 1994. Chemical weathering rate laws and global geochemical cycles. Geochimica et Cosmochimica Acta 58, 2361-2386.

Leeper, N., 2012. Characterization of the Mt. Simon sandstone in southwest Ohio for CO_2 sequestration. The Ohio State University.

Leetaru, H., Morse, D.G., Frailey, S.M., Finley, R., 2005. Mt. Simon sandstone as a carbon sequestration sink in the Illinois Basin, AAPG Annual Convention, Calgary, Alberta.

Leonenko, Y., Keith, D., Pooladi-Darvish, M., Hassanzadeh, Y., 2006. Accelerating the dissolution of CO_2 in aquifers, Eighth International Conference on Greenhouse Gas Control Technologies, Trondheim, Norway.

Liu, F., Lu, P., Zhu, C., Xiao, Y., 2011. Coupled reactive flow and transport modeling of CO_2 sequestration in the Mt. Simon sandstone formation, Midwest U.S.A. International Journal of Greenhouse Gas Control 5, 294-307.

Lu, P., Konishi, H., Oelkers, E., Zhu, C., 2015. Coupled alkali feldspar dissolution and secondary mineral precipitation in batch systems: 5. Results of K-feldspar hydrolysis experiments. Chinese Journal of Geochemistry 34, 1-12.

Maher, K., Steefel, C.I., White, A.F., Stonestrom, D.A., 2009. The role of reaction affinity and seocndary mienrals in regulating chemical weathering rates at the Santa Cruz Soil Chronosequence, California. Geochim. Cosmochim. Acta.

Meunier, A., Velde, B.D., 2004. Illite: origins, evolution, and metamorphism. Springer.

MGSC, 2011. http://sequestration.org/mgscprojects/deepsalinestorage.html.

Mohd Amin, S., Weiss, D.J., Blunt, M.J., 2014. Reactive transport modelling of geologic CO_2 sequestration in saline aquifers: The influence of pure CO_2 and of mixtures of CO_2 with CH_4 on the sealing capacity of cap rock at 37degrees C and 100 bar. Chemical Geology 367, 39-50.

Palandri, J.L., Kharaka, Y.K., 2004. A compilation of rate parameters of water-mineral interaction kinetics for application to geochemical modeling. U.S.Geol. Surv., p. 66.

Pham, V.T.H., Lu, P., Aagaard, P., Zhu, C., Hellevang, H., 2011. On the potential of CO_2–water–rock interactions for CO_2 storage using a modified kinetic model. International Journal of Greenhouse Gas Control 5, 1002-1015.

Pruess, K., Karsten, 2005. ECO2N: A TOUGH2 fluid property module for mixtures of water, NaCl,and CO2. Earth Sciences Division, Lawrence Berkeley National Laboratory.

Pruess, K., Olderburg, C., Moridis, G., 2012. TOUGH2 user's guide, version 2.0. Lawrence Berkeley National Laboratory Paper LBNL-43134.

Saldi, G.D., Jordan, G., Schott, J., Oelkers, E.H., 2009. Magnesite growth rates as a function of temperature and saturation state. Geochimica et Cosmochimica Acta 73, 5646-5657.

Soong, Y., Hedges, S.W., Howard, B.H., Dilmore, R.M., Allen, D.E., 2014. Effect of contaminants from flue gas on CO_2 sequestration in saline formation. International Journal of Energy Research 38, 1224-1232.

Spycher, N., Pruess, K., 2005. CO_2-H_2O mixtures in the geological sequestration of CO_2 center dot. II. Partitioning in chloride brines at 12-100 degrees C and up to 600 bar. Geochimica Et Cosmochimica Acta 69, 3309-3320.

Thyne, G., Boudreau, B.P., Ramm, M., Midtbø, R.E., 2001. Simulation of potassium feldspar dissolution and illitization in the Statfjord Formation, North Sea. AAPG Bulletin 85, 621-635.

Van Genuchten, M.T., 1980. A closed-form equation for predicting the hydraulic conductivity of unsaturated soils. Soil Sci Soc Am J 44, 892-898.

Walcott, C.D., 1914. Cambrian geology and paleotology. Smithsonian Misc. Coll. 57, 345-412.

Xu, T., Apps, J.A., Pruess, K., Yamamoto, H., 2007. Numerical modeling of injection and mineral trapping of CO_2 with H_2S and SO_2 in a sandstone formation. Chemical Geology 242, 319-346.

Xu, T., Sonnenthal, E., Spycher, N., Pruess, K., 2004. TOUGHREACT user's guide: A simulation program for non-isothermal multiphase reactive geochemical transport in variably saturated geologic media (V1.2), V1.2 ed. Lawrence Berkeley National Laboratory.

Yang, C., Trevino, R.H., Zhang, T., Romanak, K.D., Wallace, K., Lu, J., Mickler, P.J., Hovorka, S.D., 2014. Regional assessment of CO_2-solubility trapping potential: a case study of the coastal and offshore Texas Miocene interval. Environment Science & Technology 48, 8275-8282.

Yawar, Z., Schieber, J., 2008. Facies and depositional setting of Eau Claire Formation (Cambrian) mudstones in northwestern Indiana, Geological Society of America Abstracts with Programs, p. 435.

ZERO, 2013. http://www.zeroco2.no/projects/mt.-simon-sandstone.

Zhu, C., 2009. Geochemical modeling of reaction paths and geochemical reaction networks, in: Oelkers, E.H., Schott, J. (Eds.), Thermodynamics and Kinetics of Water-Rock Interaction. Mineralogical Society of America, pp. 533-569.

Zhu, C., Blum, A.E., Veblen, D.R.D., 2004. A new hypothesis for the slow feldspar dissolution in groundwater aquifers. Geochimica et Cosmochimica Acta 68, A148.

Zhu, C., Lu, P., 2009. Coupled alkali feldspar dissolution and secondary mineral precipitation in batch systems: 3. Saturation indices of product minerals and reaction paths. Geochimica et Cosmochimica Acta 73, 3171-3200.

Zhu, C., Lu, P., 2013. The Coupling of dissolution and precipitation reactions as the main contributor to the apparent field-lab rate discrepancy. Procedia Earth and Planetary Science 7, 948-952.

Zhu, C., Lu, P., Zheng, Z., Ganor, J., 2010. Coupled alkali feldspar dissolution and secondary mineral precipitation in batch systems: 4. Numerical modeling of reaction path and reactive transport. Geochimica et Cosmochimica Acta.

Part III. Assessing Uncertainties of Predicted Long-Term CO_2 Fate at Sleipner due to Uncertain Mineral Dissolution and Precipitation Kinetics

1. Modeling approach

Here we used a similar modeling approach as we did in Part II and built upon its the success to simulate the long-term fate of the CO_2 in the Utsira Sand at the Sleipner project. The effects of different rate laws on mineral trapping were evaluated. The rate law formulations were the same, unless stated otherwise. Specific site parameters, e.g., temperature, pressure, mineralogy, and brine composition, were modified according to the Sleipner site conditions (**Table 1**).

A CO_2 injection well was assumed to fully penetrate the 10 m thick homogeneous sandstone formation at a depth of ~820 m. Supercritical CO_2 is spilled or injected into the sandstone layer at a rate of 3.5 kg/s for 100 consecutive years and the simulation continues until 10,000 years. The thickness here is only represented symbolically and does not represent the actual aquifer thickness. Here, the evolution of CO_2 sequestration is simplified as the radial processes of multiphase flow and reactive geochemical transport, due to the smaller thickness relative to the potential lateral distance reached by CO_2 plume. After 100 years of injection, a brine is injected at a rate of 1.0 kg/s without CO_2 until the end of simulation (10,000 years) to represent, approximately, the return to regional groundwater flow post-CO_2 injection/spill.

2. Mineral and formation water composition

The mineralogical compositions for Utsira Sand (Sleipner site) used in the modeling simulations in the literature are mainly from two sources: Pearce et al. (1999) and Chadwick et al. (2004). Results from these two independent studies are similar (**Table 2**). We used the compositions based on Chadwick et al. (2004), with minor modifications. Sandstone mineralogy from Chadwick et al. (2004) was also adopted by the “Best Practice Manual, Saline Aquifer CO_2 Storage Project (SACS)” (Holloway et al., 2004). The sandstone is composed mainly of quartz (73.67% of all minerals by volume), feldspar (13% K-feldspar and 3% of albite), calcite (6%), and small amounts of muscovite, and chlorite.

No data on the formation water composition were available at the Sleipner site. Previous studies used the Oseberg formation water as a representative for the Sleipner site (e.g., Gaus et al., 2005; Audigane et al., 2007). Johnson et al. (2004a) slightly modified the chemical composition of the Oseberg formation water to be in better accordance with the mineralogy of the Utsira Formation. In this study, we adopted the formation water composition from Johnson et al. (2004a) (**Table 3**).

The thermodynamic dataset was adopted from Xu et al. (2006). The primary source for the equilibrium constants for the aqueous species and minerals used in this study originated from the EQ3/6 V7.2b database (Wolery, 1992). However, many substitutions and changes have been incorporated in response to more recent publications on the thermodynamic properties of several rock forming minerals and aqueous species. Among these are revisions to the feldspars by Arnorsson and Stefansson (1999) and Stefansson and Arnórsson (2000), several clay minerals by Aja (1997), chlorite (Xu et al., 2005), dawsonite (Ferrante et al., 1976), magnesite and dolomite (Rock et al., 2001), siderite (Preis and Gamsjager, 2002), ankerite (Xu et al., 2004), and SiO_2(aq) (Rimstidt, 1997).

3. Results and Discussion

The pH of the brine shows a stepwise distribution, reflecting the control of two different buffer reactions **(Fig. 1)**. Such a pattern is common for acidic water intrusion into a sandy aquifer with carbonate minerals (Zhu et al., 2001). In the "prograde" period (the first 100 years of injection), near the injection well where all calcite in the Utsira Sand is exhuasted, the pH of the brine is buffered by the CO_2 solubility reaction at ~3.5. This value is similar to the pH value of 3.4 found by Johnson et al. (2004b). Further away from the injection well, where calcite is still present, brine pH is buffered to ~5 by the calcite-brine reaction. This is similar to the value of 5.13 found by Audigane et al. (2007). Further downstream, the pH was maintained at the original value of ~7.4 before disturbance.

During the "retrograde" period, upstream regional groundwater with a pH of ~7.4 dissolves CO_2 at the upstream (left) edges of the CO_2 plume. The solubility reaction generated a steep slope for the pH wave on the left hand side. On the downstream side (right side), the slope of the pH wave is more gentle, as mixing is the dominant process. Over time, the low pH plume migrates downstream. **Figure 1** shows the movement of the low pH plume in color and with a three-dimensional view. At the bottom projection, the slopes of the plume indicate the velocity of the low pH plume migration. Gradually, the pH plume enlarges as it moves downstream. Note that the reaction rates for the silicate mineral dissolution are higher in acidic brine. Therefore, the low pH plume is where the most intensive reactions of dissolution and precipitation occur.

Feldspar dissolution is one of the major reactions in the aquifer, partly because of the high abundances (8.45% K-feldspar and 1.9% albite volume fraction VF. VF is defined as the volume of the mineral divided by the volume of the media, e.g., cubic meters of quartz in one cubic meter of media including framework and pores) and partly because these reactions are the slowest. Hence their reactions control other reactions. Different rate laws for feldspars result in drastically different amounts of feldspar dissolved in the Utsira (**Fig 2 and 3**). This leads to different amounts of precipitated dawsonite (**Fig 4**) through the coupled reactions:

$$CO_2(aq) + H_2O + NaAlSi_3O_8 = 3SiO_2 + NaAlCO_3(OH)_2 \qquad (1)$$

Albite Chalcedony Dawsonite

$$Na^+ + CO_2(aq) + H_2O + KAlSi_3O_8 = K^+ + 3SiO_2 + NaAlCO_3(OH)_2 \qquad (2)$$

K-feldspar Chalcedony Dawsonite

The Alex law reduced the albite dissolution rate, and hence reduced the Na^+ supply.

Different rate laws for feldspars and secondary minerals have little effect on the amount of ankerite precipitated (**Fig 5**). Ankerite precipitation can be described by the reaction:

$$1.4Na^+ + 0.6H^+ + 3.9CO_2(aq) + 0.7Mg_{2.5}Fe_{2.5}Al_2Si_3O_{10}(OH)_8 + 2.5CaCO_3 = Mg^{2+} + \qquad (3)$$

Chlorite Calcite

$$1.7H_2O + 2.1SiO_2 + 1.4NaAlCO_3(OH)_2 + 2.5CaFe_{0.7}Mg_{0.3}(CO_3)_2$$

Chalcedony Dawsonite Ankerite

Originally, the Utsira Sand contains 0.039 volume fraction or 3.9% calcite by volume. When in contact with acidic water induced by CO_2 injection, calcite is dissolved (**Fig 6)**. However, counter intuitively, only a small amount of calcite was dissolved in the aquifer. Near the injection well (0-50), all 0.039 VF calcite is dissolved. The pH was lowered to ~3.5 and is buffered by the CO_2 gas solubility reaction. However, further downstream, only a small amount of calcite was dissolved because the brine was soon enriched with HCO_3^- and Ca^{2+}, and therefore is saturated with calcite. Calcite VF decreases only from 0.039 to 0.036. At year 10,000, between 2500 and 8000m, calcite VF gradually decreases due to the dissolution induced by the lower pH of the brine。

Finally, different rate laws for mineral dissolution resulted in different predicted fates of CO_2 in the Utsira Sand **(Fig 7)**. Figure 7 shows the CO_2 partitioning into four trapping mechanisms (hydrodynamic/structural, solubility, residual/capillary, and mineral) and its temporal and spatial evolution as a result of the multi-phase flow and CO_2-brine-rock reactions. In the base case (**Fig 7a**), mineral trapping consitutute 21% of all injected CO_2. In contrast, in the Alex case (**Fig 7b**), only ~11% of total injected CO_2 s trapped in minerals. The differences increase with time, as silicate mineral reactions are slow. Therefore, whether the Utsira Sand is "reactive" or not depends on the referred time period.

4. Conclusions

In order to evaluate the uncertainties of the predicted long-term CO_2 fate in saline aquifers, due to uncertain reaction kinetics, we conducted reactive transport modeling (RTM) for the Utsira Sand, Sleipner project, Norwegian North Sea. The temporal and spatial evolution of the CO_2's fate at Sleipner, in terms of CO_2 partitioning into the four trapping mechanisms (hydrodynamic/structural, solubility, residual/capillary, and mineral), was simulated for four reaction kinetics scenarios. The four reaction kinetics scenarios feature a Burch-type empirical rate law (Burch et al., 1993) for feldspar dissolution and a BCF formulation for secondary mineral precipitation, in addition to the commonly used transition state rate law for both dissolution and precipitation.

We found that the predicted long-term fate of CO_2 is closely linked to the geochemical reactions conceptualized in the models. Predicted CO_2 mineral trapping when using the linear rate law for all dissolution and precipitation is twice as much as when using the Burch type rate law for feldspar dissolution. Therefore, the ad hoc use of the TST rate laws result in the upper bound of predicted mineral trapping mechanisms in sandy aquifers.

Part III Tables

Table 1. Hydrogeologic parameters for the Utsira sandstone formation

Parameters	Adopted values	Range	References
Permeability (m^2)	2×10^{-12}		Singh et al. (2010)
Porosity	0.35	0.34 – 0.36	Singh et al. (2010)
Thickness (m)	10		Singh et al. (2010)
Temperature (°C)	33.5	29-37	Boait et al. (2011); Cavanagh and Haszeldine (2014)
Pressure (bar)	83	80-86	CHADWICK et al. (2005); Boait et al. (2011)
CO$_2$ injection rate (kg/s)	3.5 (0-100 years)		
Co-injected brine rate (kg/s)	1.0		
Relative permeability			
Liquid (Van Genuchten, 1980):			
$k_{rl} = \sqrt{S^*\{1-(1-[S^*]^{1/m})^m\}^2}$	$S^*=(S_l-S_{lr})/(1-S_{lr})$		
S_{lr}: irreducible water saturation	0.11	0.11	Singh et al. (2010)
m: exponent	0.8		
Gas (Corey, 1954):			
$k_{rg} = \left(1-\hat{S}\right)^2\left(1-\hat{S}^2\right)$	$\hat{S} = \dfrac{(S_l - S_{lr})}{(1 - S_{lr} - S_{gr})}$		
S_{gr}: irreducible gas saturation	0.21	0.21	Singh et al. (2010)
Capillary pressure (Van Genuchten, 1980):			
$P_{cap} = -P_o\left([S^*]^{-1/m}-1\right)^{1-m}$	$S^*=(S_l-S_{lr})/(1-S_{lr})$		
S_{lr}: irreducible water saturation	0.11	0.11	
m: exponent	0.68		
P_o: strength coefficient (kPa)	2.5	2.5	Cavanagh (2013)

Table2. Initial mineral abundances and mineral phases used in the simulations

Minerals	Pearce et al. (1999)	Chadwick et al. (2004)	Minerals introduced in the model	Mineral by volume
Quartz	76.33	75	Quartz	73.67
K-feldspar	6.93	13	K-feldspar	13
Plagioclase	3.01	3 (Albite)	Albite~low, Anorthite	3
Mica/Illite	5.22	3	Muscovite	3
Calcite	6.74	3	Calcite	6
Chlorite	1.33		Chlorite	1.33
Aragonite		3	Not used	/
Pyrite	0.05		Not used	/
Ilmenite	0.12		Not used	/
Apatite	0.02		Not used	/
Zeolite	0.22		Not used	/
Ti Oxides	0.03		Not used	/
Chalcedony			Chalcedony	0.0
Magnesite			Magnesite	0.0
Dawsonite			Dawsonite	0.0
Kaolinite			Kaolinite	0.0
Siderite			Siderite	0.0
Dolomite-dis			Dolomite-dis	0.0
Ankerite			Ankerite	0.0

Table 3. Brine composition in the Utsira sandstone formation

Component	Concentration[a]
	(mol/kg H_2O)
Na	0.4520
K	0.0053
Ca	0.00742
Mg	0.0181
Al	1.3×10^{-8}
Si	1.66×10^{-4}
Fe (total)	1.0×10^{-8}, [b]
Cl	0.5213
C	0.00232
pH	7.2

[a] Johnson et al. (2004a). [b] Assumed value

Table 4. Adopted kinetic data for minerals

Mineral	[a]Log k_H (E_a)	[b]Log k_{H2O} (E_a)	[c]n	[d]Reactive surface area	Rate Law (Base Case)	Rate Law (Alxe Case)	Rate Law (BCF Case)	Rate Law (Alex+BCF Case)
Calcite	Equilibrium	Equilibrium			Equilibrium	Equilibrium	Equilibrium	Equilibrium
Quartz		-13.99 (87.6)		9.8	TST	TST	Dissolution: TST; Precipitation BCF	Dissolution: TST; Precipitation BCF
K-feldspar	-10.06 (51.7)	-12.41 (38.0)	0.5	9.8	TST	Dissolution: Alex; Precipitation: TST	Dissolution: TST; Precipitation BCF	Dissolution: Alex; Precipitation BCF
Oligoclase	-9.67 (65.0)	-11.84 (69.8)	0.457	9.8	TST	Dissolution: Alex; Precipitation: TST	Dissolution: TST; Precipitation BCF	Dissolution: Alex; Precipitation BCF
Muscovite	-11.85 (22.0)	-13.55 (22.0)	0.37	151.6	TST	TST	Dissolution: TST; Precipitation BCF	Dissolution: TST; Precipitation BCF
Chlorite	-11.11 (88.0)	-12.52 (88.0)	0.5	9.8	TST	TST	Dissolution: TST; Precipitation BCF	Dissolution: TST; Precipitation BCF
Chalcedony		-9.42 (49.8)[f]			TST	TST	Dissolution: TST; Precipitation BCF	Dissolution: TST; Precipitation BCF
Kaolinite	-11.31 (65.9)	-13.18 (22.2)	0.777	151.6	TST	TST	Dissolution: TST; Precipitation BCF	Dissolution: TST; Precipitation BCF
Magnesite	-6.38 (14.4)	-9.34 (23.5)	1.0	9.8	TST	TST	Dissolution: TST; Precipitation BCF	Dissolution: TST; Precipitation BCF
Siderite	Set to dolomite	-8.9 (62.76)[e]	Set to dolomite	9.8	TST	TST	Dissolution: TST; Precipitation BCF	Dissolution: TST; Precipitation BCF
Dawsonite	Set to dolomite	Set to siderite	Set to dolomite	9.8	TST	TST	Dissolution: TST; Precipitation BCF	Dissolution: TST; Precipitation BCF
Ankerite	Set to dolomite	Set to siderite	Set to dolomite	9.8	TST	TST	Dissolution: TST; Precipitation BCF	Dissolution: TST; Precipitation BCF
Dolomite-dis	-3.19 (36.1)	-7.53 (52.2)	0.5	9.8	TST	TST	Dissolution: TST; Precipitation BCF	Dissolution: TST; Precipitation BCF

[a] Log kinetic rate constant k_H (mol/m^2/s) at 25 ^{o}C and activation energy E_a (kJ/mol) for acid mechanism from Palandri and Kharaka (2004).

[b] Log kinetic rate constant k_{H2O} (mol/m^2/s) at 25 ^{o}C and activation energy E_a (kJ/mol) for neutral mechanism from Palandri and Kharaka (2004).

[c] Power term n with respect to $H+$ from Palandri and Kharaka (2004).

[d] Reactive surface area (cm^2/g) based on Sonnenthal and Spycher (2001), which was reduced by one order of magnitude.

[e] From Steefel (2001).

[f] Data for chalcedony precipitation while the dissolution kinetics data were assumed to be the same as those for quartz

Part III. Figures

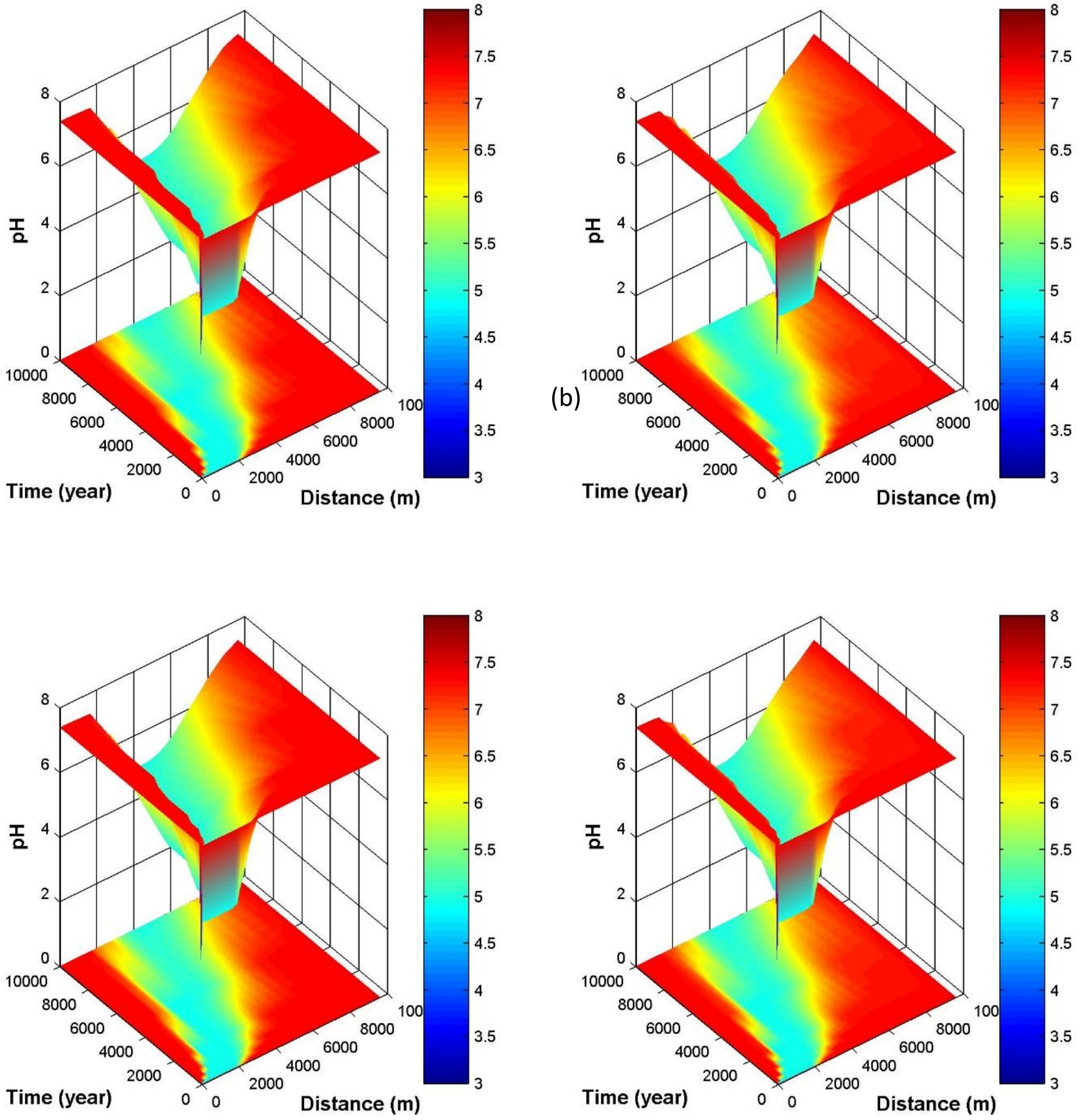

Figure 1. Temporal and spatial evolution of the brine pH in the simulated Utsira Sand. In our model, we assumed CO_2 injection/spill into Layer 9 for 100 years. Regional groundwater was allowed to flow back to the domain after the spill/injection and the simulation was continued until year 10,000. From top left clockwise: (a) Base Case; (b) Alex Case; (c) BCF Case; (d) Alex+BCF Case.

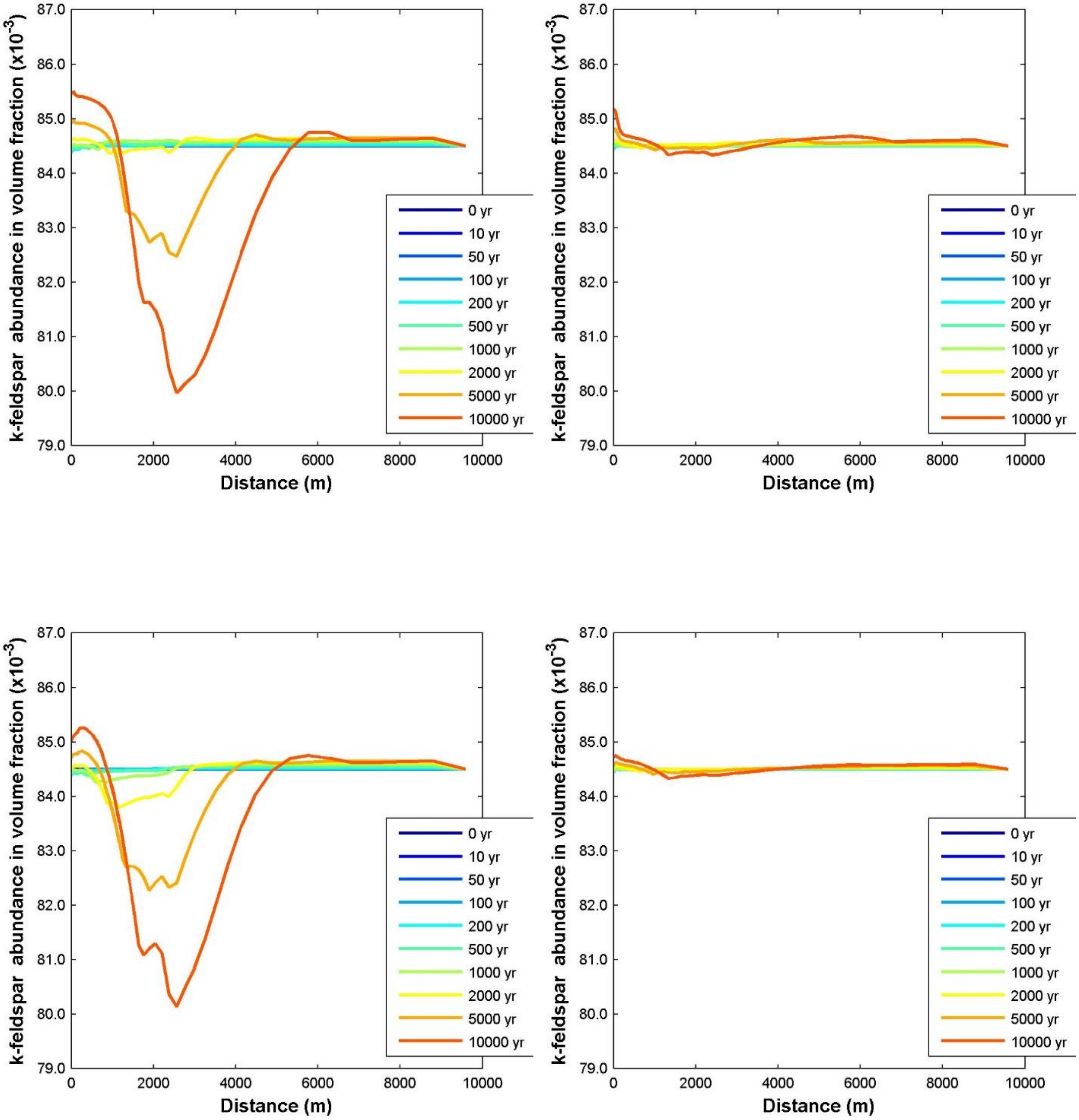

Figure 2. Volume fraction (VF) of K-feldspar and its evolution with time and space. From top left clockwise: (a) Base Case; (b) Alex Case; (c) BCF Case; (d) Alex+BCF Case.

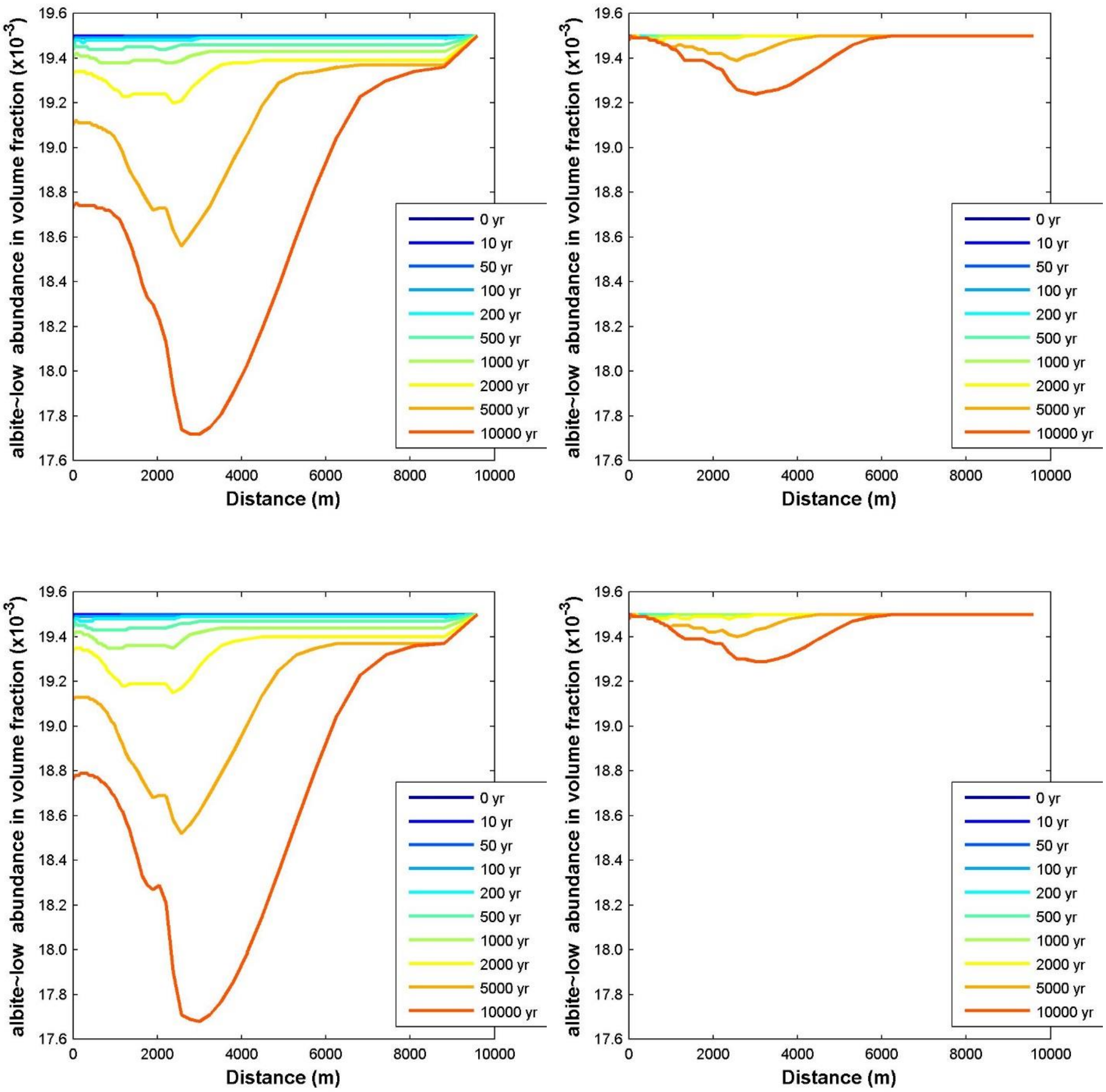

Figure 3. Volume fraction (VF) of low-albite and its evolution with time and space. From top left clockwise: (a) Base Case; (b) Alex Case; (c) BCF Case; (d) Alex+BCF Case.

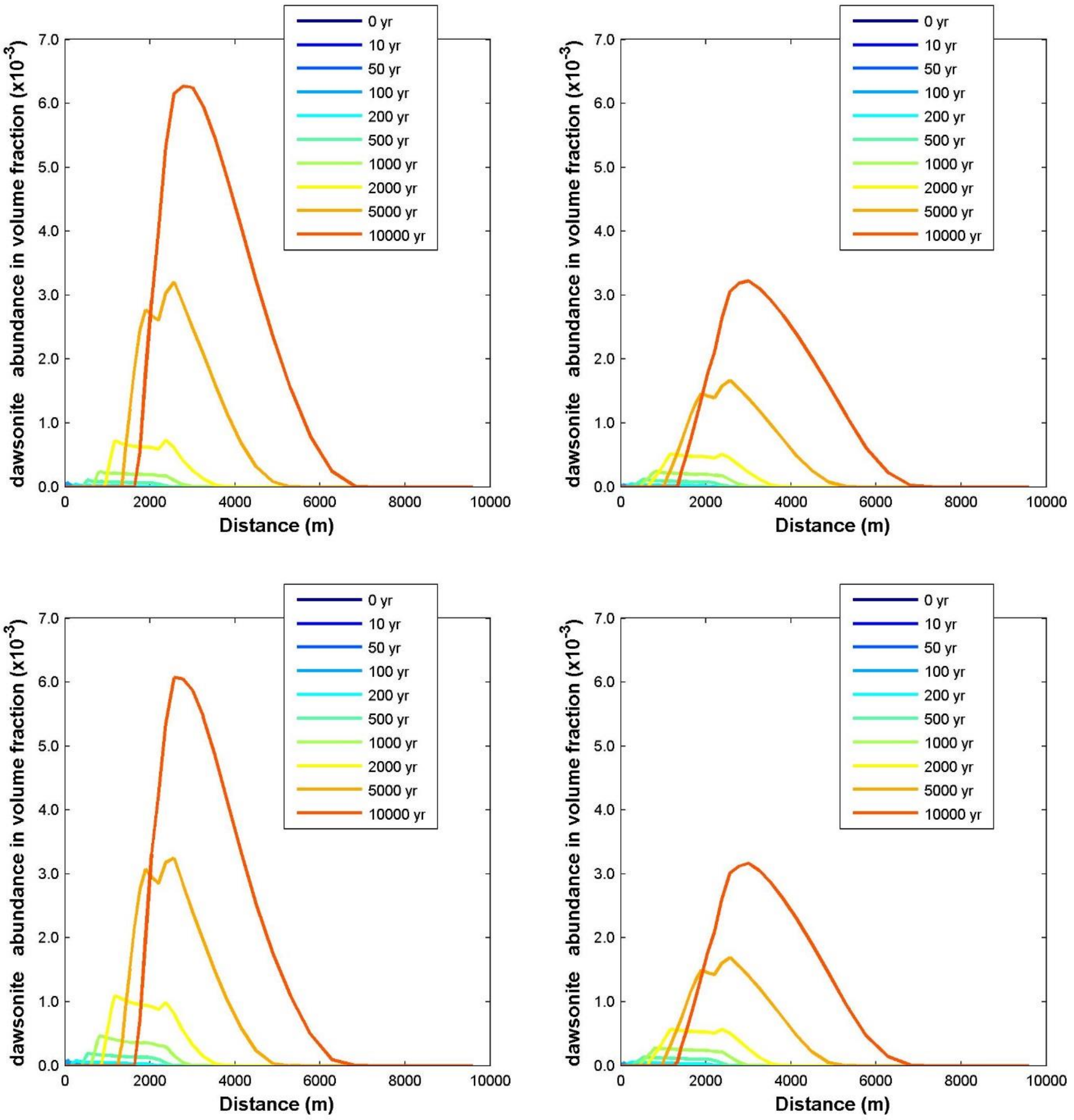

Figure 4. Volume fraction (VF) of dawsonite and its evolution with time and space. From top left clockwise: (a) Base Case; (b) Alex Case; (c) BCF Case; (d) Alex+BCF.

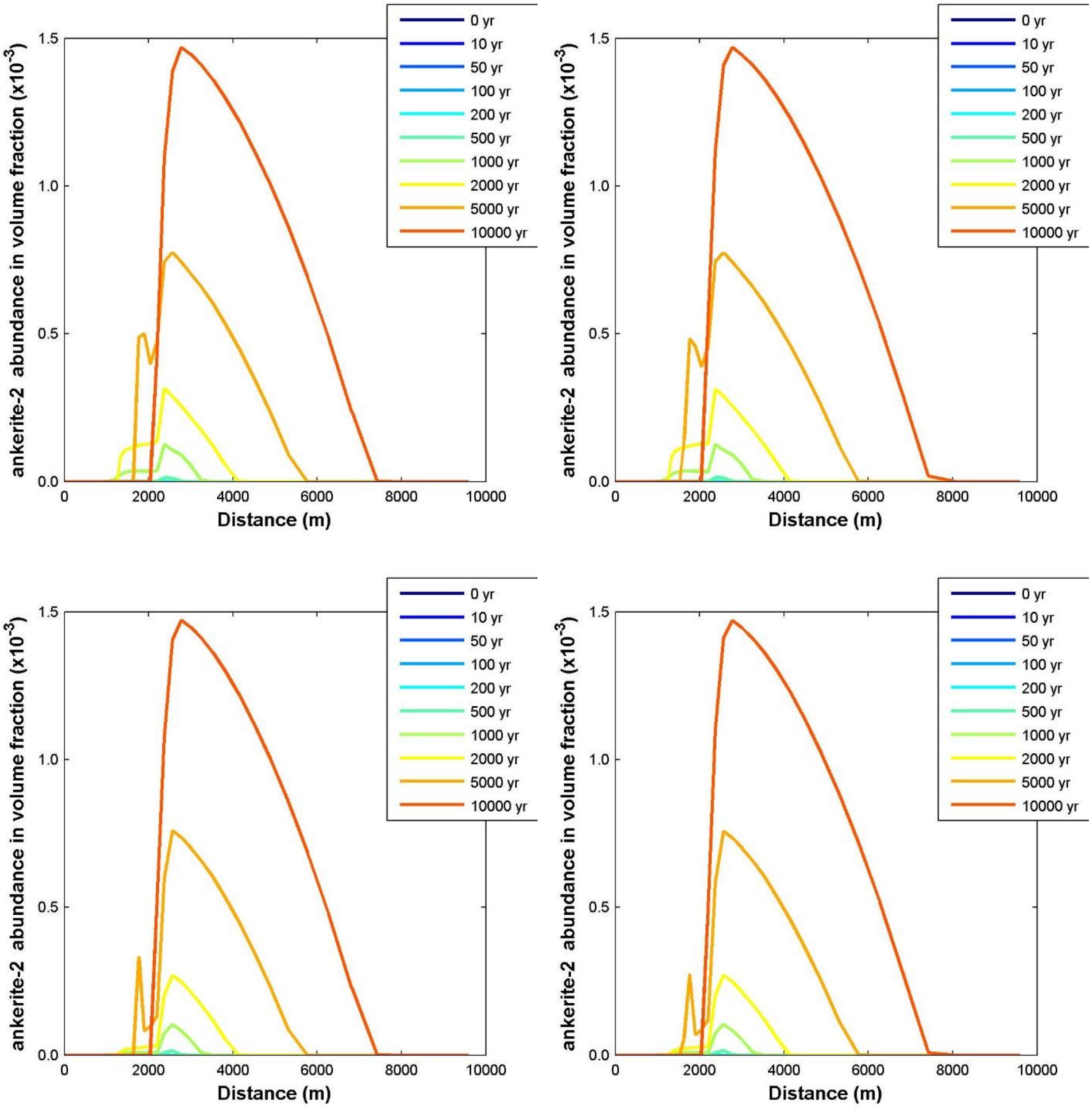

Figure 5. Volume fraction (VF) of ankerite and its evolution with time and space. From top left clockwise: (a) Base Case; (b) Alex Case; (c) BCF Case; (d) Alex+BCF. Different rate laws for feldspars do not result in different ankerite precipitation because ankerite precipitation is more related to chlorite.

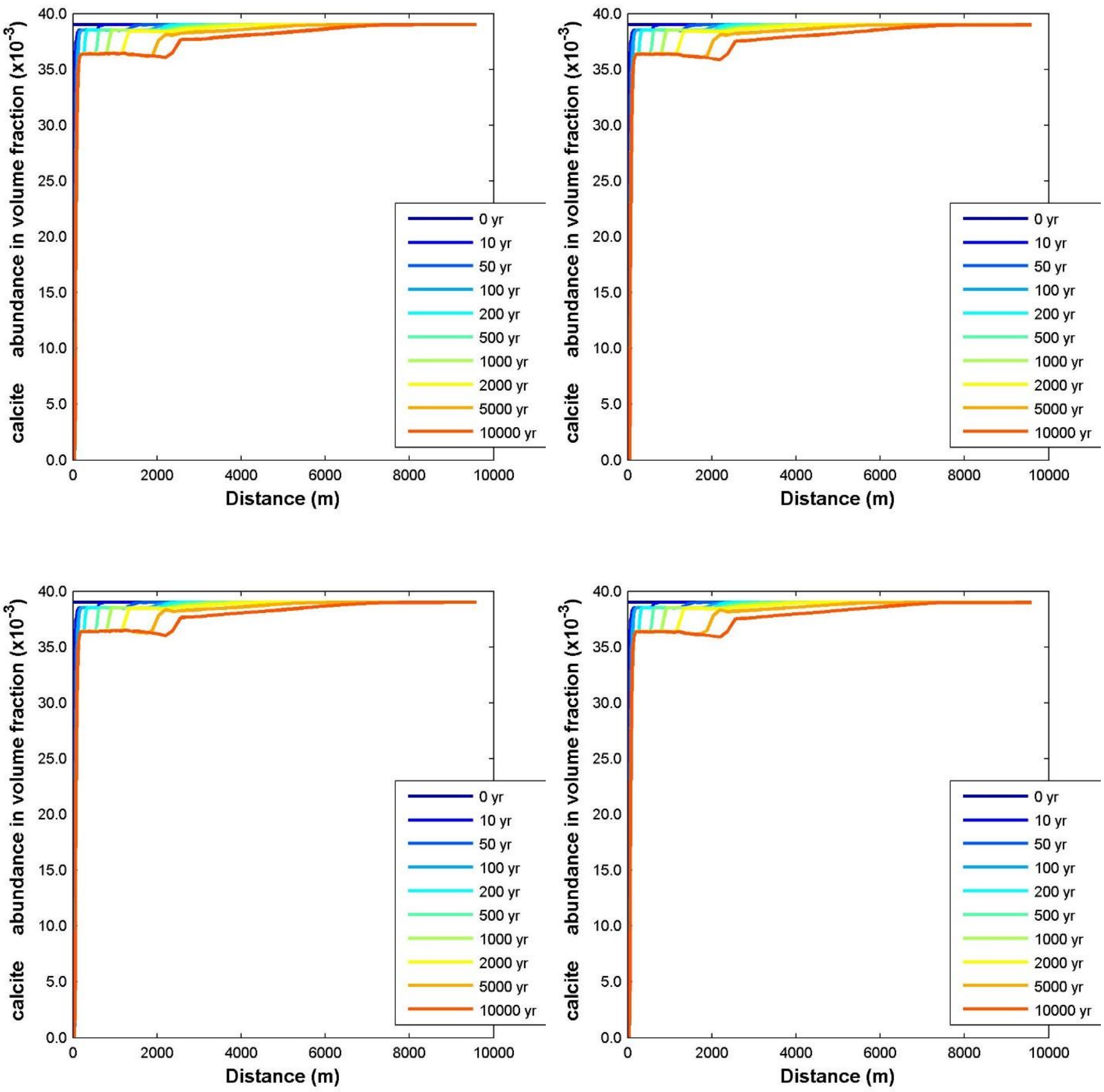

Fig. 6. Volume fraction (VF) of calcite and its evolution with time and space. From top left clockwise: (a) Base Case; (b) Alex Case; (c) BCF Case; (d) Alex+BCF Case

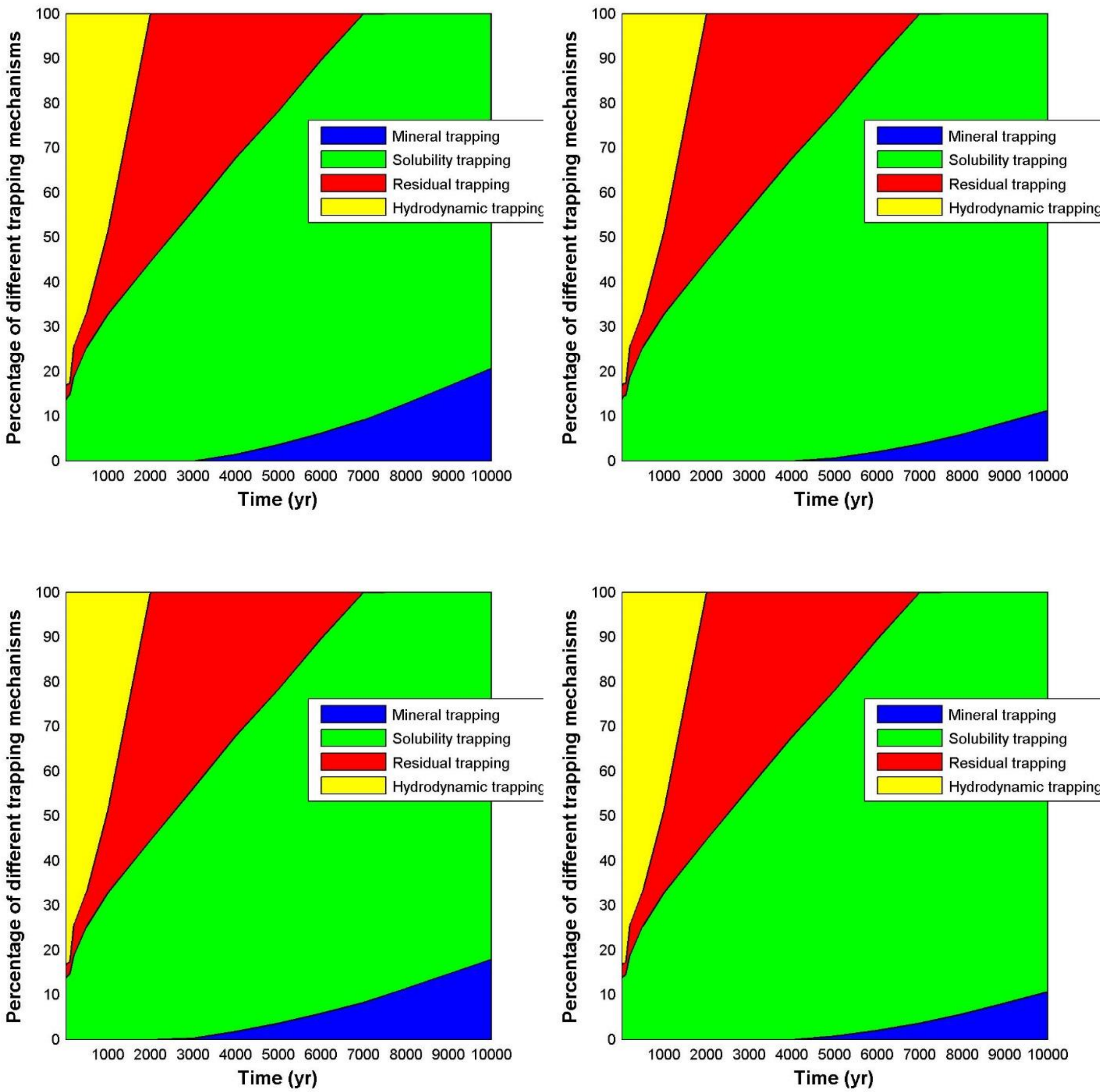

Figure 7. CO$_2$ partitioning into four trapping mechanisms (hydrodynamic/structural, solubility, residual/capillary, and mineral) and its temporal and spatial evolution as a result of multi-phase flow and CO$_2$-brine-rock reactions. From top left clockwise: (a) Base Case; (b) Alex Case; (c) BCF Case; (d) Alex+BCF Case.

References Cite

Aja, S.U., 1997. Formation and stability of endmember illite .1. Solution equilibration experiments at 100 to 250 degrees C and P-v,P-soln - Comment. Geochimica Et Cosmochimica Acta 61, 4455-4460.

Arnorsson, S., Stefansson, A., 1999. Assessment of feldspar solubility constants in water in the range of 0 degrees to 350 degrees C at vapor saturation pressures. Am J Sci 299, 173-209.

Audigane, P., Gaus, I., Czernichowski-Lauriol, I., Pruess, K., Xu, T.F., 2007. Two-dimensional reactive transport modeling of CO_2 injection in a saline Aquifer at the Sleipner site, North Sea. American Journal of Science 307, 974-1008.

Boait, F., White, N., Chadwick, A., Noy, D., Bickle, M., 2011. Layer spreading and dimming within the CO_2 plume at the sleipner field in the north sea. Energy Procedia 4, 3254-3261.

Burch, T.E., Nagy, K.L., Lasaga, A.C., 1993. Free energy dependence of albite dissolution kinetics at 80° C and pH 8.8. Chemical Geology 105, 137-162.

Cavanagh, A., 2013. Benchmark calibration and prediction of the Sleipner CO_2 plume from 2006 to 2012. Energy Procedia 37, 3529-3545.

Cavanagh, A.J., Haszeldine, R.S., 2014. The Sleipner storage site: Capillary flow modeling of a layered CO_2 plume requires fractured shale barriers within the Utsira Formation. International Journal of Greenhouse Gas Control 21, 101-112.

CHADWICK, R.A., ARTS, R., EIKEN, O., 2005. 4D seismic quantification of a growing CO2 plume at Sleipner, North Sea. Geological Society, London, Petroleum Geology Conference series 6, 1385-1399.

Chadwick, R.A., Zweigel, P., Gregersen, U., Kirby, G.A., Holloway, S., Johannessen, P.N., 2004. Geological reservoir characterization of a CO2 storage site: The Utsira Sand, Sleipner, northern North Sea. Energy 29, 1371-1381.

Corey, A.T., 1954. The interrelation between gas and oil relative permeabilities. Prod. Mon., 38-41.

Ferrante, M.J., Stuve, J.M., Richardson, D.W., 1976. Thermodynamic data for synthetic dawsonite. U.S. Bureau of Mines Report Investigation, 8129, Washington, D.C., 13p.

Gaus, I., Azaroual, M., Czernichowski-Lauriol, I., 2005. Reactive transport modelling of the impact of CO_2 injection on the clayey cap rock at Sleipner (North Sea). Chemical Geology 217, 319-337.

Holloway, S., Chadwick, A., Lindeberg, E., Czernichowski-Lauriol, I., Arts, R., 2004. Best Practice Manual, Saline Aquifer CO_2 Storage Project (SACS), 53 pp.

Johnson, J.W., Nitao, J.J., Knauss, K.G., 2004a. Reactive transport modeling of CO_2 storage in saline aquifers to elucidate fundamental processes, trapping mechanisms, and sequestration partitioning: in Geol. Soc. London Spec. Pub. 233 Geologic Storage of Carbon Dioxide, Baines, S.J., and Worden, R.H., eds., p. 107-128.

Johnson, J.W., Nitao, J.J., Knauss, K.G., 2004b. Reactive transport modelling of CO_2 storage in saline aquifers to elucidate fundamental processes, trapping mechanisms and sequestration partitioning. Geological Society, London, Special Publications 233, 107-128.

Palandri, J.L., Kharaka, Y.K., 2004. A compilation of rate parameters of water-mineral interaction kinetics for application to geochemical modeling. U.S.Geol. Surv., p. 66.

Pearce, J.M., Kemp, S.J., Wetton, P.D., 1999. Mineralogical and petrographical characterization of 1m core from the Utsira formation, Central North Sea: British Geological Survey, Report WG/99/24C.

Preis, W., Gamsjager, H., 2002. Critical evaluation of solubility data: enthalpy of formation of siderite. Phys. Chem. Chem. Phys. 4, 4014-4019.

Rimstidt, J.D., 1997. Quartz solubility at low temperatures. Geochimica et Cosmochimica Acta 61, 2553-2558.

Rock, P.A., Mandell, G.K., Casey, W.H., Walling, E.M., 2001. Gibbs Energy of Formation of Dolomite from Electrochemical Cell Measurements and Theoretical Calculations. Am J Sci 301, 103-111.

Singh, V., Cavanagh, A., Hansen, H., Nazarian, B., Iding, M., Ringrose, P., 2010. Reservoir modeling of CO_2 plume behavior calibrated against monitoring data from Sleipner, Norway, SPE Annual Technical Conference and Exhibition, Florence, Italy.

Sonnenthal, E.L., Spycher, N., 2001. Drift-scale coupled processes (DST and THC seepage) models, Yucca Mountain Project, Lawrence Berkeley National Laboratory, Berkeley, California.

Steefel, C.I., 2001. CRUNCH. Lawrence Livermore National Laboratory, p. 76.

Stefansson, A., Arnórsson, S., 2000. Feldspar saturation state in natural water. Geochimica et Cosmochimica Acta 64, 2567-2584.

Van Genuchten, M.T., 1980. A Closed-form Equation for Predicting the Hydraulic Conductivity of Unsaturated Soils. Soil Sci Soc Am J 44, 892-898.

Wolery, T.J., 1992. EQ3/6, A software package for geochemical modeling of aqueous systems: Package overview and installation guide (version 7.0):. URCL-MA-110662-PT-I, Livermore, Calif., Univ. California, Lawrence Livermore Laboratory.

Xu, T., Apps, J.A., Pruess, K., 2004. Numerical simulation of CO_2 disposal by mineral trapping in deep aquifers. Applied Geochemistry 19, 917-936.

Xu, T., Apps, J.A., Pruess, K., 2005. Mineral sequestration of carbon dioxide in a sandstone-shale system. Chemical Geology 217, 295-318.

Xu, T., Sonnenthal, E., Spycher, N., Pruess, K., 2006. TOUGHREACT--A simulation program for non-isothermal multiphase reactive geochemical transport in variably saturated geologic media: Applications to geothermal injectivity and CO_2 geological sequestration. Computers & Geosciences 32, 145-165.

Zhu, C., Hu, F.Q., Burden, D.S., 2001. Multi-component reactive transport modeling of natural attenuation of an acid ground water plume at a uranium mill tailings site. Journal of Contaminant Hydrology 52, 85-108.

Grand Summary of Findings and Conclusions

In order to assess modeling uncertainties for CCUS, we simulated CO_2 plume migration in the uppermost layer (Layer 9) of the Utsira Sand in the Norwegian North Sea and long-term fate of CO_2 up to 10,000 years. In Part I, we applied two multi-phase compositional simulators to the Sleipner Benchmark model and calibrated the model against the time-lapsed seismic monitoring data from 1999, 2001, 2002, 2004, 2006, 2008, and 2010. Calibration against plume outlines, specifically the CO_2-water contacts, which are based on the geophysical monitoring data, was accomplished by introducing permeability anisotropy, adjusting reservoir temperature, and taking into account the CH_4 impurity in the CO_2 stream at Sleipner.

In Part II & III, we assessed uncertainties of the predicted long-term CO_2 fate in saline aquifers due to uncertain reaction kinetics. Reactive transport models (RTM) were used for simulating multi-phase flow, transport, and CO_2-water-rock reactions using the software ToughReact. Under four scenarios of rate laws, the temporal and spatial evolution of CO_2 fate was simulated in terms of CO_2 partitioning into the four trapping mechanisms (hydrodynamic/structural, solubility, residual/capillary, and mineral). The four scenarios of reaction kinetics feature a Burch-type empirical rate law for feldspar dissolution and BCF formulation for secondary mineral precipitation, in addition to the commonly used linear rate law for both dissolution and precipitation reactions. A domain with a distance of 10,000 m from the injection well, a scenario of 100 years of CO_2 injection, and subsequent CO_2-water-rock reactions up to 10,000 years with a regional flow of ~1 m/yr was constructed for simulations. In Part II, we used a generic sandy aquifer. In Part III, we simulated CO_2 fate in the topmost layer or Layer 9 in the Utsira Sand.

Our modeling results show:

(1) The simulated CO_2-water contacts approximately matched with the observed areal extent of the CO_2 plume in 1999, 2001, 2002, 2004, 2006, and 2008 and showed improvements over previous models. To quote Cavanagh (2013): “These (previous) models have failed to quantitatively or qualitatively reproduce the plume morphology to date.” Here, our model was generally able to match the elongated, northward extension of the observed plume.

(2) The approximate history match at Sleipner was achieved by calibrating the model against CO_2-water contacts delineated by seismic data with adjustments of permeability (k), reservoir temperature (T), and CH_4 composition in the CO_2 streams. An increase of N-S permeability is justified by the sedimentary geology of the site and the presence of an N-S trending CO_2 plume. Reservoir temperature and CH_4% used in the model are within the ranges of reported values in the literature. However, the model is not unique. Many combinations of k, T, and CH_4 would produce similar matches, and other possibilities that would have improved the development of an N-S elongated CO_2 plume, such as a slight tilting of the surface of Utsira top to the south, were not considered.

(3) Although many parameters are uncertain, which leads to uncertainness of the simulated plume extent, the predicted short-term fate of CO_2 at Sleipner nevertheless fell within a narrow band, ~93±2% structural/hydrodynamic trapping and ~7±2% solubility trapping. For time periods of decades, mineral trapping is negligible because of the low temperature at Sleipner.

(4) For long-term, e.g., 10,000 years, the Utsira aquifer is reactive and mineral trapping is significant. However, the predicted CO_2 fate is subject to uncertainties of reaction kinetics. Modeling results show that different rate laws for mineral dissolution and precipitation

reactions resulted in different predicted amounts of trapped CO_2 by carbonate minerals, with scenarios of the conventional linear rate law for feldspar dissolution having twice as much mineral trapping (21% of injected CO_2) as scenarios with a Burch-type or Alekseyev et al.–type rate law for feldspar dissolution (11%). So far, most RTM studies for CCUS have used the conventional linear rate law and therefore simulated the upper bound of mineral trapping. The negligence of the regional flow after injection, however, as in most previous studies, artificially limited the extent of geochemical reactions as if in a batch system. With replenishing undersaturated groundwater from upstream, the Utsira Sand is reactive over a time scale of 10,000 years.

In conclusion, it appears that we were able to use widely available reservoir simulation tools to simulate multiphase flow at Sleipner and reproduce an N-S elongated CO_2 plume. Our reactive transport modeling of long-term CO_2 fate underscore prediction uncertainties resulting from uncertain reaction kinetics and the significance of replenishing regional flow after CO_2 injection in evaluation of mineral trapping.